

Study of Structural, Transport and Magnetic Properties of Some Perovskite Based Oxides

THESIS SUBMITTED FOR THE DEGREE OF

DOCTOR OF PHILOSOPHY

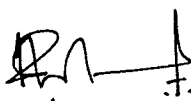
IN THE FACULTY OF NATURAL SCIENCE
GOA UNIVERSITY
GOA

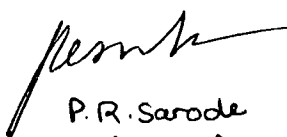
By

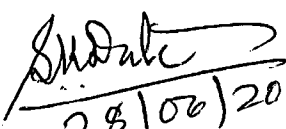
530.41
MUR/STU

P. S. RAMU MURTHY
DEPARTMENT OF PHYSICS
GOA UNIVERSITY
GOA 403 206

The corrections recommended by the referees have been
duly carried out in the thesis.


T. K.R. Pholkan
28/6/2011 (Co-guide)


P. R. Sarode
(Guide)
OCTOBER 2010

Examined

28/06/2011
(Examiner)

T-532

DECLARATION

The author hereby declares that this thesis represents work which has been carried out by him and that it has not been submitted to any other University or Institution for the award of any Degree, Diploma, Associateship, Fellowship or any other such title.

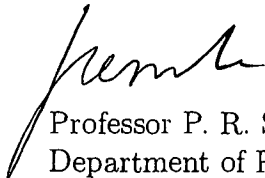
Place: Taleigao Plateau.

Date : October, 2010


18/10/2010.
P. S. Ramu Murthy

CERTIFICATE

We hereby certify that the above Declaration of the candidate Mr. P. S. Ramu Murthy is true and that this thesis represents his independent work.


Professor P. R. Sarode
Department of Physics
Goa University, Goa

18/10/2010


18/10/2010
Dr. K. R. Priolkar
Department of Physics
Goa University, Goa

Acknowledgement

It is indeed my privilege to thank all those involved directly or indirectly and contributed to the success of this work. I wish to express my sincere thanks to my supervisors: Prof. P. R. Sarode and Dr. K. R. Priolkar, Department of Physics, Goa University, for the guidance and the freedom to work in my own way.

I am very indebted to Dr. Kaustubh R. S. Priolkar for bringing the best in me and giving me all the encouragement, vision and teaching me the finer aspects of research. A great friend of mine, is indeed rare to find.

Financial assistance from UGC-DAE Consortium for Scientific Research, Mumbai under Project number CRS-M-126 is gratefully acknowledged.

I am thankful to Dr. Amitabh Das, Solid State Physics Division, BARC, Mumbai for all the help extended to me in performing Neutron Diffraction measurements at BARC through the collaborative research scheme, Prof. M. S. Hegde, Solid State and Structural Chemistry Unit, Indian Institute of Science, (SSCU-IISc) Bangalore for extending the facility to carry out XPS measurements, Prof. A. K. Nigam and Dr. Preeti Bhoje, Tata Institute of Fundamental Research, Mumbai for all the help in carrying out magnetization experiments.

Profuse thanks to Prof. J. A. E. Desa, Dr. Ramesh Pai and the other members of the teaching faculty at the Department of Physics, Goa University for their valuable help and feedback through out my research work.

I am also thankful to my colleagues, late Mr. Orlando Fernandes, Dr. A. F. Barbosa and Dr. J. B. C. Efrem D'Sa for their continuous encouragement and support.

Special thanks to my colleagues, Mrs. Suchana Amonkar, Dr. Swati Pawar at Dhempe College of Arts and Science, and Research students, Mr. Nelson Lobo, Miss. Shraddha Ganorkar, Mr. Kapil Ingle for their company and support.

A note of thanks to the technical and administrative staff of Physics Department, Goa University for their cooperation during the tenure of my research.

Special thanks to my family, especially my wife Jyoti who has gone above and beyond what women expect of their spouses in support of me. During my years of research at the University, she has taken over almost all aspects of maintaining our home, has been a stellar parent at all times, and has managed on her own on numerous occasions that I have travelled to perform experiments and attend conferences and symposia. Without her love and support, I would not have considered returning to University, let alone had the confidence to complete my degree.

I also owe a debt of gratitude to my parents and my in-laws for their motivation and support that has helped me thrive in thought and action and to my brothers and sisters who have always been there for me.

Contents

1	Introduction	1
1.1	Historical Background	1
1.2	Structure of ABX_3 Perovskite	4
1.2.1	Cation Ordering	10
1.3	Double Perovskites: Structural and Magnetic Properties	10
1.4	Electronic Interactions of Perovskites	14
1.4.1	Direct Exchange	15
1.4.2	Indirect Exchange	19
1.5	Scope of the Present Study	23
1.5.1	Ruthenium Double Perovskites	23
	References	30
2	Experimental Techniques	36
2.1	Introduction	36
2.2	Sample Preparation Technique	36
2.2.1	Solid State Synthesis of Ceramic Samples	37
2.3	Diffraction Methods	37
2.3.1	X-ray Diffraction	37

2.3.2	Neutron Powder Diffraction	40
2.4	Bulk Characterization Methods	42
2.4.1	Magnetometry	42
2.4.2	Four Probe Resistivity	49
2.5	X-ray Photoelectron Spectroscopy	50
2.6	X-ray Absorption Fine Structure Spectroscopy	52
2.6.1	Experimental Setup	53
2.6.2	Sample Preparation	55
	References	57
3	Disorder Induced Negative Magnetization in LaSrCoRuO₆	59
3.1	Introduction	59
3.2	Structural Studies(X-ray and Neutron Powder Diffraction)	61
3.3	Magnetization Measurements	64
3.4	X-ray Absorption Fine Structure	71
3.5	Discussion	72
3.6	Conclusions	73
	References	74
4	Structure, Transport and Magnetic Properties in	
	La_{2x}Sr_{2-2x}Co_{2x}Ru_{2-2x}O₆	76
4.1	Introduction	76
4.2	Results	78
4.2.1	X-ray Diffraction Studies	78

4.2.2	Magnetization Studies	80
4.2.3	Neutron Diffraction	86
4.2.4	Resistivity Measurements	86
4.2.5	X-ray Photoelectron Spectroscopic Studies	89
4.3	Discussion	90
4.4	Conclusion	92
	References	93
5	Effect of B-site Dopants on Magnetic and Transport Properties of	
	LaSrCoRuO₆	95
5.1	Introduction	95
5.2	Results	97
5.2.1	LaSrCo _{1-x} Ru _{1+x} O ₆	97
5.2.2	LaSrCo _{1-y} Cu _y RuO ₆	108
5.3	Discussion	111
5.4	Conclusion	114
	References	115
6	Role of A-site Cations in Magnetic and Transport Properties of	
	LaSrCoRuO₆	117
6.1	Introduction	117
6.2	Structural Studies	119
6.3	Transport Measurements	120
6.4	Magnetization Measurements	122

6.5 Discussion	127
6.6 Conclusion	128
References	129
7 Summary and Conclusions	131
7.1 Implications of this work	132
7.2 Future Work	137

List of Tables

3.1	Unit cell parameters, Co and Ru site occupancies obtained from Rietveld refinement and Curie-Weiss parameters calculated from magnetization measurements at 1000 Oe for the two samples of $\text{LaSrCo}_{1-x}\text{Ru}_{1+x}\text{O}_6$. Numbers in parentheses are uncertainty in the last digit.	62
3.2	Structural parameters like bond length ($\text{R}\text{\AA}$), bond angle and mean square radial displacement ($\sigma^2\text{\AA}^2$) obtained from Co and Ru K edge EXAFS analysis. Numbers in parentheses are uncertainty in the last digit.	72
4.1	Expected (E) and refined (R) occupancies of Co and Ru for different values of $\text{La}_{2x}\text{Sr}_{2-2x}\text{Co}_{2x}\text{Ru}_{2-2x}\text{O}_6$	80
4.2	Unit cell parameters obtained from Rietveld refinement and Curie-Weiss parameters calculated from magnetization measurements at 1000 Oe for $\text{La}_{2x}\text{Sr}_{2-2x}\text{Co}_{2x}\text{Ru}_{2-2x}\text{O}_6$. Numbers in parentheses are uncertainty in the last digit.	80

5.1	Room temperature structural parameters obtained from Le Bail fitting and high temperature magnetic and transport properties for $\text{LaSrCo}_{1-x}\text{Ru}_{1+x}\text{O}_6$. Here a , b , c and β denote unit cell parameters, V is the unit cell volume, μ_{eff} (μ_B/fu) and Θ_{CW} represent effective magnetic moment and Curie Weiss temperature respectively and T_p is temperature of peak magnetization seen in ZFC curve. Numbers in parentheses are uncertainty in the last digit.	101
5.2	Room temperature structural parameters obtained from Le Bail fitting and high temperature magnetic and transport properties for $\text{LaSrCo}_{1-x}\text{Ru}_{1+x}\text{O}_6$. Here a , b , c and β denote unit cell parameters, μ_{eff} and Θ_{CW} represent effective magnetic moment and Curie Weiss temperature respectively and T_p is temperature of peak magnetization seen in ZFC curve. Numbers in parentheses are uncertainty in the last digit.	110
6.1	Unit cell parameters, Co and Ru site occupancies obtained from Rietveld refinement, Bond Valence Sums, Bond angles between Co and Ru octahedra and Curie-Weiss parameters calculated from magnetization measurements at 1000 Oe for the two samples of LaSrCoRuO_6 and LaCaCoRuO_6 . Numbers in parentheses are uncertainty in the last digit.	122

List of Figures

1.1	The ideal cubic ABX_3 perovskite structure (two views)	6
1.2	Cooperative $BX_{6/2}$ rotations giving (a) tetragonal (projection on (001) of $BX_{6/2}$ array) (b) rhombohedral and (c) orthorhombic (Pbnm) symmetry	8
1.3	Network of $BX_{6/2}$ octahedra in the ABX_3 perovskite polytypes: (a) cubic 3C, (b) hexagonal 2H, (c) hexagonal 6H, (d) hexagonal 4H and (e) rhombohedral 9R	9
1.4	Ideal cubic double perovskite having a chemical formula $A_2BB'O_6$. Oxygen atoms form octahedra around alternating B and B' ions	12
1.5	The mechanism of Super exchange.	21
1.6	The mechanism of Double exchange.	22
2.1	The Bragg condition, $2d\sin\theta = n\lambda$, where n is an integer, the extra distance traveled by the x-rays to the farther plane of atoms is equal to the multiple of the X-ray wavelength.	38
2.2	The Neutron Powder Diffractometer at BARC used for neutron diffraction measurements. The description of the instrument parameters can be seen on the right.	41
2.3	General wiring diagram of the SQUID Magnetometer from Quantum Inc.	45
2.4	Diagram of the second order Gradiometer coils	46

2.5	A typical 'scan' of the SQUID Magnetometer	46
2.6	Schematic of the XAFS experiment. The setup for both the transmission and fluorescence geometries is depicted	54
3.1	Rietveld refined XRD patterns for LSCR13 and LSCR12. The open circles show the observed counts and the continuous line passing through these counts is the calculated profile. The difference between the observed and calculated patterns is shown as a continuous line at the bottom of the two profiles. The calculated positions of the reflections are shown as vertical bars.	61
3.2	Observed (circles), calculated (line) and difference ND patterns recorded at 300K (upper panel) for LSCR13 and LSCR12. The inset presents data in limited range with the superlattice reflections seen clearly in LSCR13 indicating higher degree of order. The lower panel shows neutron data taken at 20K for the same samples. The inset presents data in limited range with the arrows indicating magnetic reflections present in LSCR13.	63
3.3	Magnetization as a function of temperature at applied fields of 1000 Oe in LSCR13 (a) and LSCR12 (b).	64
3.4	Inverse Magnetic susceptibility function of temperature calculated as $\chi = M/H$ at applied fields of 1000 Oe in LSCR13 and LSCR12.	66
3.5	ZFC and FC magnetization curves at applied field of 50 Oe recorded for LSCR13 (a) and LSCR12 (b).	67

3.6	Isothermal magnetization curves for LSCR13 recorded in the field interval of $\pm 5T$ at 5K (a); its magnified view (± 10 KOe) (b); virgin magnetization curves at few representative temperatures (c) and variation of magnetization values extracted from virgin curves at a field value of ~ 50 Oe. . . .	68
3.7	Isothermal magnetization curves for LSCR12 recorded in the field interval of $\pm 5T$ at 5K (a); its magnified view (± 10 KOe) (b); virgin magnetization curves at few representative temperatures (c) and variation of magnetization values extracted from virgin curves at a field value of ~ 50 Oe. . . .	70
3.8	k^3 weighted magnitude of Fourier transform of EXAFS data recorded at Co and Ru K-edge in LSCR13 and LSCR12.	71
4.1	Rietveld refined XRD patterns of $\text{La}_{2x}\text{Sr}_{2-2x}\text{Co}_{2x}\text{Ru}_{2-2x}\text{O}_6$. The open circles show the observed counts and the continuous line passing through these counts is the calculated profile. The difference between the observed and calculated patterns is shown as a continuous line at the bottom of the two profiles. The calculated positions of the reflections are shown as vertical bars.	79
4.2	Magnetization as a function of temperature recorded in applied fields of 1000 Oe (upper panel) and 50 Oe (lower panel) in $\text{La}_{2x}\text{Sr}_{2-2x}\text{Co}_{2x}\text{Ru}_{2-2x}\text{O}_6$. 81	81
4.3	Plot of inverse magnetic susceptibility (H/M) as a function of temperature calculated using magnetization data recorded in applied field of 1000 Oe in $\text{La}_{2x}\text{Sr}_{2-2x}\text{Co}_{2x}\text{Ru}_{2-2x}\text{O}_6$	83
4.4	Isothermal magnetization curves recorded in the field interval of $\pm 5T$ at 5K for $\text{La}_{2x}\text{Sr}_{2-2x}\text{Co}_{2x}\text{Ru}_{2-2x}\text{O}_6$	85

4.5	Observed (circles), calculated (line) ND patterns recorded at 300K and 20K in case of $\text{La}_{2x}\text{Sr}_{2-2x}\text{Co}_{2x}\text{Ru}_{2-2x}\text{O}_6$ for $x = 0.25$ and $x = 0.75$. The data at 20K is shown in limited range for clarity. The continuous line at the bottom is the difference line between observed and calculated data.	87
4.6	Resistivity of $\text{La}_{2x}\text{Sr}_{2-2x}\text{Co}_{2x}\text{Ru}_{2-2x}\text{O}_6$ as a function of temperature (upper panel). The lower panel shows a plot of $\log \rho$ versus $T^{-1/4}$ for all compositions.	88
4.7	Co(2p) and Ru(3p) core level spectra along with fitted curves for $\text{La}_{2x}\text{Sr}_{2-2x}\text{Co}_{2x}\text{Ru}_{2-2x}\text{O}_6$ compounds.	90
5.1	Le bail fitted XRD patterns for $\text{LaSrCo}_{1-x}\text{Ru}_{1+x}\text{O}_6$. The data points are indicated as circles and the solid line through them is the fit to the data. The difference pattern is shown at the bottom along with tick marks indicating Bragg reflections.	98
5.2	Variation of intensity of superlattice $(\frac{1}{2}, \frac{1}{2}, \frac{1}{2})$ reflection with increasing Ru ($x > 0$) and Co ($x < 0$) doping.	99
5.3	(a) Composition dependance of the unit cell volume in $\text{LaSrCo}_{1-x}\text{Ru}_{1+x}\text{O}_6$. (b) Variation of tolerance factor t with x in $\text{LaSrCo}_{1-x}\text{Ru}_{1+x}\text{O}_6$	100
5.4	Magnetization curves for $\text{LaSrCo}_{1-x}\text{Ru}_{1+x}\text{O}_6$ during the ZFC and FC cycle recorded at 1000 Oe.	103
5.5	Isothermal magnetization recorded at 5K in the field range of $\pm 5\text{T}$ for two different values of x belonging to $\text{LaSrCo}_{1-x}\text{Ru}_{1+x}\text{O}_6$. Insets show the expanded ($\pm 4500\text{Oe}$) loops.	104

5.6	Low field (50 Oe) magnetization data as a function of temperature for $\text{LaSrCo}_{1-x}\text{Ru}_{1+x}\text{O}_6$. The inset in plot of $x = 0.2$ shows the initial magnetization curve as a function of applied field for the same sample.	105
5.7	Neutron diffraction patterns recorded at 300K and 20K for $x = 0.2$ and -0.2 of the series $\text{LaSrCo}_{1-x}\text{Ru}_{1+x}\text{O}_6$. The 300K data is presented in the 2θ range of 5° to 100° as circles along with Rietveld refined curve (solid line through the data) and the difference curve at the bottom. The 20K data is shown in limited range to highlight the weak magnetic reflections (marked with corresponding (h,k,l) values).	107
5.8	Resistivity as a function of temperature for $\text{LaSrCo}_{1-x}\text{Ru}_{1+x}\text{O}_6$ compounds where $x = -0.2, 0$ and 0.2	108
5.9	XRD patterns of $\text{LaSrCo}_{1-y}\text{Cu}_y\text{RuO}_6$ for $y = 0.1$ and 0.2 along with best fitted line and difference line shown at the bottom. The ticks indicate the positions of allowed Bragg reflections.	109
5.10	ZFC and FC magnetization curves for $\text{LaSrCo}_{1-y}\text{Cu}_y\text{RuO}_6$ recorded at $H = 1000\text{Oe}$	110
5.11	Temperature variation of electrical resistivity for $\text{LaSrCo}_{1-y}\text{Cu}_y\text{RuO}_6$ where $y = 0.1$ and 0.2	112
6.1	Isothermal Magnetization recorded at 5K in applied fields of $\pm 5\text{T}$ for LaSrCoRuO_6	119

6.2	Rietveld refined XRD patterns for LaSrCoRuO_6 (upper panel) and LaCaCoRuO_6 (lower panel). The open circles show the observed counts and the continuous line passing through these counts is the calculated profile. The difference between the observed and calculated patterns is shown as a continuous line at the bottom of the two profiles. The calculated positions of the reflections are shown as vertical bars.	121
6.3	Temperature dependance of resistivity of LaSrCoRuO_6 and LaCaCoRuO_6	123
6.4	Magnetization as a function of temperature at applied fields of 1000 Oe for LaSrCoRuO_6 and LaCaCoRuO_6	124
6.5	Plot of Inverse Magnetic susceptibility ($1/\chi = H/M$) as a function temperature for LaSrCoRuO_6 and LaCaCoRuO_6 . The solid line is a fit to Curie-Weiss equation.	125
6.6	Magnetization as a function of temperature at applied fields of 50 Oe in LaSrCoRuO_6	126

Chapter 1

Introduction

The perovskite structure has shown great flexibility of composition, incorporating nearly every member of the periodic table. The basic perovskite framework, a 3-dimensional array of corner sharing octahedra, is also the basis for related structures, known collectively as layered perovskites, which include two dimensional layers of corner sharing octahedra separated by layers of cations. The perovskite and layered perovskite structures can incorporate ions of a variety of sizes and charges, as this framework is flexible, allowing for subtle distortions that ease the bond strains created by size mismatch. However, the perovskite structure does compete with other structures of similar stoichiometry. Perovskites and layered perovskites are of great interest for the wide variety of useful properties that they exhibit. Each of these properties is influenced by the structure, as subtle changes alter symmetry considerations, bond overlap, and band energy levels. Understanding and predicting the structure of these compounds is essential for the intelligent design of new and useful materials.

1.1 Historical Background

The mineral perovskite, CaTiO_3 , was discovered by German chemist and mineralogist Gustav Rose in 1839, who named it for the Russian dignitary Lev Alexeievich Perovsky

[1]. Since then, the name "perovskite" has been applied to the many compounds, synthetic and natural, that have similar structure and stoichiometry. Much of the early work on synthetic perovskites was done by V.M. Goldschmidt,[2, 3] who developed the principal of the tolerance factor as well as other principals in use today. They are ceramics (solid materials combining metallic elements with nonmetals, usually oxygen) that have a particular atomic arrangement. They are the earth's most abundant minerals and have long been of interest to geologists for the clues they hold to the planet's history. They fascinate from a technological point of view as well because, as a group, natural and synthetic perovskites exhibit an array of electrical properties. Whereas a given crystal structure is usually associated with a specific electrical property, perovskites run the gamut from insulators to semiconductors (in which whole ions rather than just electrons, flow through the crystal), metal-like conductors and now high-temperature semiconductors. What accounts for this remarkable range of properties arises from the flaws in the superconductors wherein a slight modification of the ideal perovskite architecture often results in new features. There is no one-to-one correlation; a given modification does not automatically produce a particular degree of electrical conductivity, yet any time the ideal structure is altered, the possibility of new electrical or other properties arises.

In their ideal form, perovskites which are described by the generalized formula ABX_3 , consist of cubes made up of three distinct chemical elements (A, B and X) that are present in a ratio of 1:1:3. The A and B atoms are metallic cations (ions with a positive charge) and the X atoms are non-metallic anions (ions with a negative charge). An A cation - the larger of the two kinds of metals - lies at the center of each cube, the B cations occupy all eight corners and the X anions lie at the midpoints of the cube's 12 edges. The mineral

perovskite, CaTiO_3 , that forms at high temperatures embodies the ideal structure. Its unit cell, or basic building block, consists of a single cube. The calcium in the A position is larger than the titanium in the B positions and oxygen fills all 12 of the X sites. The crystal often grows into the shape of a cube or an octahedron, reflecting the symmetry of the atomic structure.

Many perovskites are somewhat distorted because the central A cation is too small in relation to the B cations at the corners of the cube. The disparity causes the X atoms, and sometimes the B's to move out of position. Crystallographers often visualize such movements by thinking of the ideal unit cell not as a simple cube but as a cluster of polyhedrons. Each B cation, which defines the corner of adjoining cubes, is surrounded by and closely bonded to six anions, one from each of the six cube edges that converge at the corner. The anions define the points of an octahedron. The A cation formerly viewed as being at the center of a cube, is now considered to be surrounded by eight corner-sharing octahedrons, each of which contains a B cation in the center. When A cations are too small in relation to the B cations, the octahedrons, whose axes are aligned in an ideal perovskite, tilt and twist, the framework collapses around the A cations, lowering the symmetry and potentially altering the perovskite's optical, elastic, electrical and other physical properties. Dozens of different perovskite tilt patterns have been identified. In tilted perovskites, as in the ideal forms, the B cations may remain at the center of their octahedrons. In some perovskites, however, the B cations are slightly shifted. Such "off-centering" of positively charged cations can give perovskite crystals electrical polarity: one end is positively charged and the other end is negatively charged. More-over, the direction of the off-centering can often be changed simply by subjecting the sample to an electric

field. Materials that are both polarized and able to reverse polarity under the influence of an electric field are known as ferroelectrics and have many applications in electronic devices. The suitability of a particular combination of cations for the perovskite structure can be estimated by the use of the tolerance factor t as seen in the equation below where r_A is the radius of the A-site cation, r_B is the radius of the B-site cation and r_O is the radius of the O^{2-} ;

$$t = \frac{(r_A + r_O)}{\sqrt{2}(r_B + r_O)} \quad (1.1)$$

1.2 Structure of ABX_3 Perovskite

The structural family of perovskites is a large family of compounds having crystal structures related to the mineral perovskite $CaTiO_3$. In the ideal form, the crystal structure of cubic ABX_3 perovskite can be described as consisting of corner sharing $[BX_6]$ octahedra with the A cation occupying the 12-fold coordination site formed in the middle of the cube of eight such octahedra. The ideal cubic perovskite structure is not very common and also the mineral perovskite itself is slightly distorted. The perovskite family of oxides is probably the best studied family of oxides. The interest in compounds belonging to this family of crystal structure arises in the large and ever uprising variety of properties exhibited and the flexibility to accommodate almost all of the elements in the periodic system. Pioneering structural work on perovskites were conducted by Goldschmidt et al in the 1920's that formed the basis for further exploration of the perovskite family of compounds [3]. Distorted perovskite have reduced symmetry, which is important for their magnetic and electric properties. Due to these properties, perovskites have great industrial importance, especially the ferroelectric tetragonal form of $BaTiO_3$. If a large

oxide ion is combined with a metal ion having a small radius, the resulting crystal structure can be looked upon as close packed oxygen ions with metal ions in the interstitials. This is observed in many compounds with oxygen ions and transition metals of valence +2, e.g. NiO, CoO, and MnO. In these crystal structures, the oxygen ions form a cubic close packed lattice (ccp) with the metal ion in octahedral interstitials (i.e. the rock salt structure). Replacing one fourth of the oxygen with a cation of approximately the same radius as oxygen (e.g. alkali, alkali earth or rare earth element) reduces the number of octahedral voids, occupied by a small cation, to one fourth. The chemical formula can then be written as ABX_3 , and the crystal structure is called a perovskite. X is often oxygen but also other large ions such as F^- and Cl^- are possible. The idealized cubic structure is realized e.g. in $CaRbF_3$ and $SrTiO_3$. The latter can be described as Sr^{2+} and O^{2-} ions forming a cubic close packed lattice with the Ti^{4+} ions occupying the octahedral holes created by the oxygens. The perovskite structure has a three dimensional net of corner sharing $[TiO_6]$ octahedra with the Sr^{2+} ions in the twelve fold cavities in between the polyhedra. The perovskite structure is known to be very flexible and the A and B ions can be varied leading to the large number of known compounds with perovskite or related structures. Most perovskites are distorted and do not have the ideal cubic structure.

This structure has the ability to adapt to a mismatch between the equilibrium (A-X) and (B-X) bond lengths and to different average (A-X) and (B-X) equilibrium bond lengths where more than one A-site cation and /or B-site cation species is present allows for realization of a large number and variety of stoichiometric perovskites. Moreover, the ability of the structure to tolerate atomic vacancies and to form inter-growth structures extends this family even further. The substitution of an aliovalent A-site cation allows

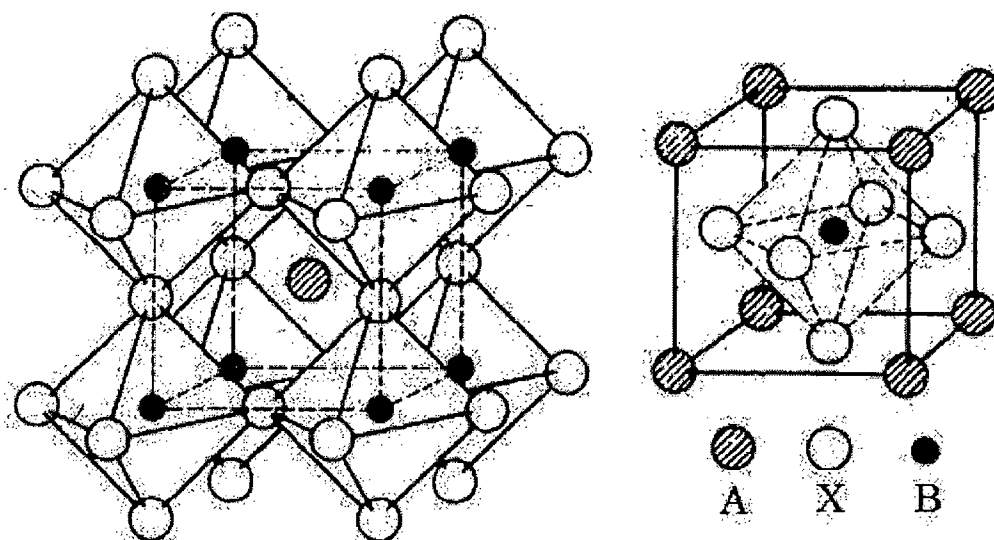


Figure 1.1: The ideal cubic ABX_3 perovskite structure (two views).

realization of a mixed valence on an BX_3 array with minimal perturbation of its periodic potential. A measure of this perturbation is the variance,

$$\sigma^2(r_A) \equiv \langle (r_A)^2 \rangle - \langle r_A \rangle^2 \quad (1.2)$$

where r_A is the A-cation ionic radius.

The ideal perovskite structure is built up of a cubic ABCABC stacking of close-packed ABX_3 planes with B cations occupying the octahedral interstices coordinated by six X anions. A measure of the mismatch of the average (A-X) and (B-X) equilibrium bond lengths in the cubic phase is given by the deviation from unity of the geometric tolerance factor,

$$t = \frac{(A - X)}{\sqrt{2}(B - X)} \quad (1.3)$$

The equilibrium (A-X) and (B-X) bond lengths are calculated for ambient conditions from the sums of the ionic radii available in the tables [4], obtained from X-ray data

taken at room temperature and ambient pressure. Since the (A-X) and (B-X) bonds have different thermal expansion and compressibility, $t = t(T, P)$ is unity at a single temperature for a given pressure. A larger thermal expansion of the (A-X) bonds makes $dt/dT > 0$ except where a spin-state transition occurs on the B cation. Normally the (A-X) bond is found to be more compressible than the (B-X) bond [5, 6, 7], which makes $dt/dP < 0$; but where transition-metal B atoms have 3d electrons that approach or enter the crossover from localized to itinerant electronic behavior, the (B-X) bond appears to be more compressible and give a $dt/dP > 0$ [8].

A $t < 1$ is found to place the (B-X) bonds under compression and the (A-X) bonds under tension. The structure alleviates these stresses by a cooperative rotation of the $BX_{6/2}$ octahedra that lowers the space group symmetry from cubic ($Pm\bar{3}m$). 15 tilt systems and their space groups that are possible were identified by Glazer also providing a notation for their description. The common rotations are about a cubic [001] axis to give the tetragonal ($I4/mcm$ if rotations of successive (001) planes are out of phase and $P4/mbm$ if these rotations are in-phase) symmetry of Fig.1.2(a) about a cubic [111] axis to give the rhombohedral ($R\bar{3}c$ if the rotation in successive (111) planes are out of phase and $Im\bar{3}$ if these rotations are in phase) symmetry of Fig.1.2(b) or about a cubic [110] axis to give the orthorhombic ($Pbnm$ or $Pnma$) symmetry of Fig.1.2(c). At highest temperatures, the perovskites are normally cubic; transformation to a lower symmetry on cooling introduces twins, which makes the determination of the local structure with single-crystal diffraction difficult. The Cooperative rotations are found to bend the B-X-B bond angles from 180° to $(180^\circ - \phi)$ and the average angle θ_{av} decreases on going from tetragonal to rhombohedral to orthorhombic symmetry. In the orthorhombic structure, the

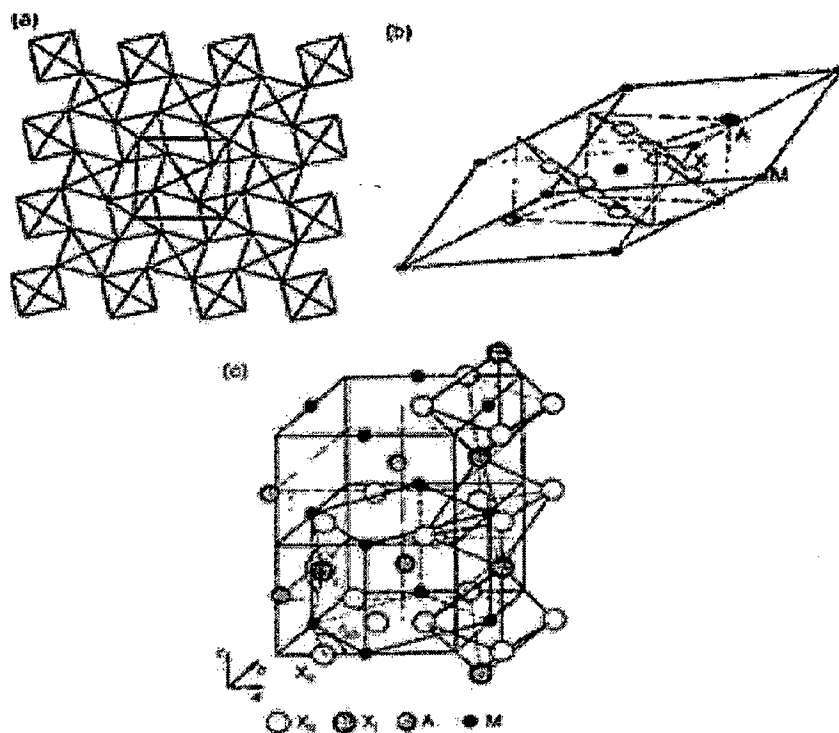


Figure 1.2: Cooperative $BX_{6/2}$ rotations giving (a) tetragonal (projection on (001) of $BX_{6/2}$ array) (b) rhombohedral and (c) orthorhombic (Pbnm) symmetry

cubic [110] axis about which the $BX_{6/2}$ octahedra rotate is the b-axis, which normally makes $b > c/\sqrt{2} > a$, where c is parallel to the cubic [001] axis. The rotations however, introduce a shortest A-X bond along the a-axis that is subjected to a compressive stress that is relieved by a bending from 90° of an X-B-X bond angle of the $BX_{6/2}$ octahedra, this bending would then increase a. At the larger tolerance factors t of the range in which the orthorhombic phase is stabilized, a small bending from 90° of the octahedral-site bond angle is sufficient to make $a > c/\sqrt{2} > b$.

A $t > 1$ places the (B-X) bonds under tension and the (A-X) bonds under compression. Under tension, the B-X-B bond angle remains 180° , but the B-X bond may develop a

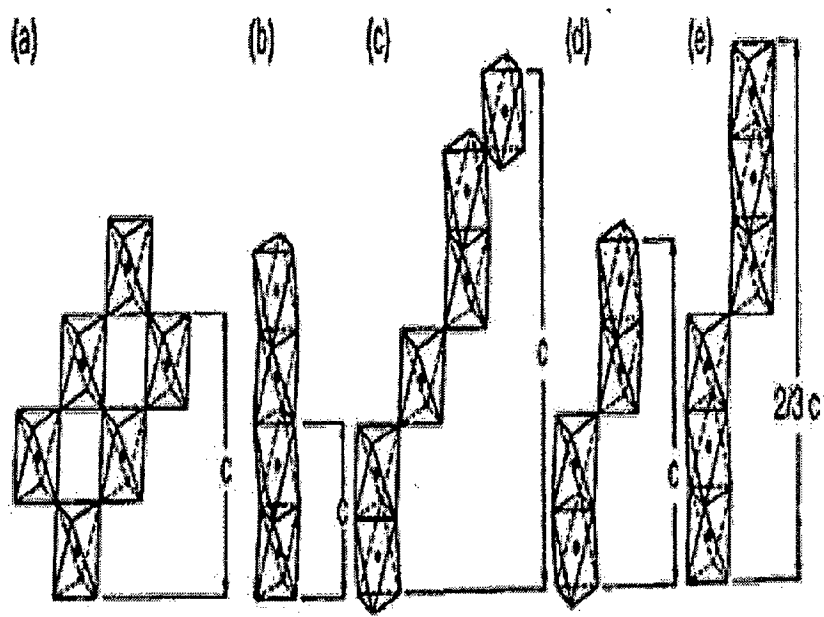


Figure 1.3: Network of $BX_{6/2}$ octahedra in the ABX_3 perovskite polytypes: (a) cubic 3C, (b) hexagonal 2H, (c) hexagonal 6H, (d) hexagonal 4H and (e) rhombohedral 9R

double-well potential energy that results in ferroic properties. Alternatively, the structure may alleviate the tensile stresses by introducing hexagonal ABAB stacking, the octahedral sites coordinated by six anions sharing common octahedral-site faces in isolated columns accommodated between columns rather than common octahedral-site corners as in cubic stacking. A shared octahedral-site face however increases the $M^{m+}-M^{m+}$ electrostatic repulsive energy and therefore lowers the Madelung energy of an ionic perovskite. As a compromise between the loss in elastic-stress energy and the loss in Madelung energy, the hexagonal stackings are introduced in stages with increasing $(t-1)$ to give a series of polytypes as shown in the Fig.1.3.

1.2.1 Cation Ordering

Cation ordering can occur on both the A and B sites. There are many examples of double perovskites $A_2BB'X_6$ in which the B and B' atoms are ordered because of a charge difference $\Delta q \leq 2e$ and or a large size and electronegativity difference. Cation ordering may allow stabilization in an octahedral site of a cation that is too large to be normally found in such a site. Similarly ordering of A-site cations in $AA'B_2O_6$ perovskites are known. Of particular interest is where smaller ions such as Cu^{2+} or Mn^{3+} that are stable in square coplanar coordination induce a cooperative rotation of the $BO_{6/2}$ octahedra that provides four coplanar nearest neighbors from the twelve-fold oxygen coordination of an A-site. Some examples include $(CaCu_3)B_4O_{12}$ where $B = Ge, Mn, Ti, Ru$ and $(NaMn_3)Mn_4O_{12}$. With a $\Delta q = 3e$, ordered $A_3BB'_2O_9$ perovskites have been found as in $Sr_3MgSb_2O_9$ and $Ba_3BaTa_2O_9$. Similarly, ordering of A-site cations in $AA'B_2O_6$ perovskites are known.

1.3 Double Perovskites: Structural and Magnetic Properties

The investigation of double perovskite oxides dates back to 1961 when a ferromagnetic behavior of Re-based double perovskites was reported by Longo and Ward [9]. Afterwards, a slow progress was made until 1998 when the publication of Kobayashi et al [10] on half-metallic properties of Sr_2FeMoO_6 renewed the interest in this class of compounds. Later, the half-metallicity was also demonstrated by first principles calculations of the density of states in Sr_2FeReO_6 [11]. Possible spin-electronics applications arising from the electronic structure caused a rapid advancement in the study of double perovskites.

Physics of the system involves a wide range of effects making them a challenging subject of investigation. This involves the interplay of the crystallographic structure and both electronic and magnetic properties. The double perovskites belong to a large family of oxides with general formula $A_2BB'O_6$ (A being a large divalent or trivalent alkaline earth ion, B and B' transition metal ions) as seen in Fig. 1.4. The A ions are 12-fold coordinated to oxygen, B and B' are located in the centre of the oxygen octahedra. In case of a significant size or valence difference between B and B' ions, they occupy an alternating crystallographic sites i.e. B type atom has only B' neighbors and vice versa so BO_6 and $B'O_6$ octahedra are arranged in two interleaving fcc sublattices. Such a configuration is known under the name of an **ordered double perovskite**. If the size or valence difference is diminished, the ordering becomes more difficult to obtain and the amount of structural defects increases. The basic crystallographic structure being a cubic one, can be described in terms of the $Fm\bar{3}m$ space group. Due to the mismatch of the A ions and B(B') ions sizes, the octahedra can undergo cooperative tilting in order to obtain a configuration that is more favorable from the energetic point of view.

While the A cation size gets smaller, an empty space arises around it and needs to be filled up. Space groups exhibiting lower symmetry replace then the cubic structure. Using Glazer's terminology [12], the $a^0a^0c^-$ octahedral tilt is responsible for the occurrence of the tetragonal structure ($I4/m$ space group), while the monoclinic structure ($P2_{1/n}$ space group) arises from the $a^+b^-b^-$ tilt. Such tilts shift the oxygen atoms from their ideal positions giving rise to additional diffraction peaks. For small distortions, a unit cell with cubic symmetry is allowed for the structural refinements of the diffraction data. The tetragonal distortion requires a new unit cell to be defined, with its main axes

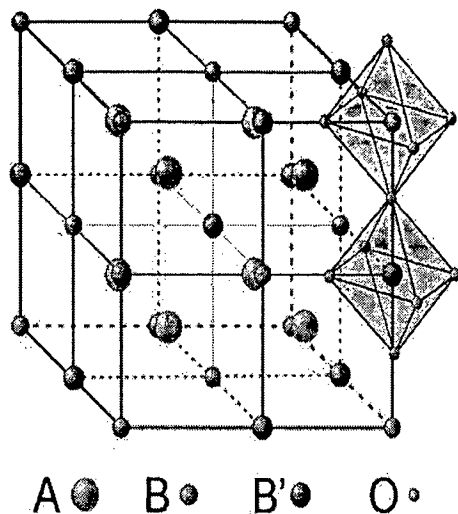


Figure 1.4: Ideal cubic double perovskite having a chemical formula $A_2BB'O_6$. Oxygen atoms form octahedra around alternating B and B' ions

being defined along the cubic $[110]$ and $[-110]$ directions. The lattice parameters of the tetragonal cell are defined as: $c = c_{cubic} = c_{tetra}$ and $a_{tetra} = a_{cubic}/\sqrt{2}$.

As in the case of simple perovskites, the tolerance factor can be defined that allows the anticipation of the crystallographic structure on the basis of the tabulated ionic radii due to the mismatch between the A site cation and the space available inside the oxygen octahedra. The main difference with respect to the perovskites is that the double perovskite structure requires two distances (B - O and B' - O) to be taken into account. Consequently the double perovskite tolerance factor t can be defined as:

$$t = \frac{r_A + r_O}{\sqrt{2}[(r_b + r_O)]} \quad (1.4)$$

where r_i is an effective ionic radius of the i^{th} atom ($i = A, B \text{ or } B'$) whose values are tabulated by Shannon [13] and r_b arises from the average of the ionic radii of B and B'

ions.

The accuracy of the estimation of the oxygen atom positions is of primary importance while calculating the experimental value of the tolerance factor. Apparently, it can be said as a general rule valid for all members of the double perovskite family that $t > 1.05$ requires a hexagonal structure, for $1.05 > t > 1.00$, the cubic structure with Fm3m space group is the most likely one, for $1.00 > t > 0.97$, the compound has a tetragonal structure with I4/m space group, and finally for $0.97 > t$, the compound becomes monoclinic having P2₁/n space group or orthorhombic.

In the ideal double perovskite, the oxygen atoms are located between the B and B' ions on a straight line. However, this is valid only for highly symmetric systems (and for small tetragonal distortions). Further, lowering of the symmetry causes the deviation of the B - O - B' angle from 180° due to tilting of the BO₆ and B'O₆ octahedra. This consequently affects the electronic interactions along B - O - B' - O - B paths.

Double perovskites contain equal concentrations of two different B-site cations that are ordered. Although the R_{0.5}A_{0.5}MnO₃ perovskites with $t \leq t_c$ that have an ordering of Mn⁴⁺ and Mn³⁺ ions might be considered double perovskites, the term is generally reserved for perovskites with two B-site cations of different atoms that are ordered. Ordering of B-site cations into alternate BO_{6/2} sites normally requires a charge difference of at least 2e between the two B-cation species or a large size and electronegativity difference of the B-site cation. A smaller A-site cation stable in eight-fold oxygen coordination and a large electropositive A-site cation like Ba²⁺ that is most stable in twelve-fold oxygen coordination may order into alternate (001) planes in an oxygen-deficient perovskite provided the B-site cations are stable in square-pyramidal coordination. Although these

oxygen-deficient perovskites are not classified as double perovskites, they do represent an important ordering of two different A-site cations present in 50-50 concentrations. Two examples of A-site ordering are $\text{TbBaCo}_2\text{O}_{5.5}$ [14] and RBaFeO_5 .

Trunkanov et al [15] have shown that RBaMn_2O_6 perovskites prepared in air at high temperature are cubic with disordered R^{3+} and Ba^{2+} ions on the A sites, however annealing in a reducing atmosphere is found to yield tetragonal RBaMn_2O_5 with R^{3+} and Ba^{2+} ordered on alternate (001) planes. The ordering of the A sites is retained on re-oxidation to RBaMn_2O_6 at lower temperatures. The magnetic and electrical properties depend sensitively not only on the A-site cation ordering, but also as in other manganese-oxide perovskites on the geometric tolerance factor.

1.4 Electronic Interactions of Perovskites

Perovskites with transition metal ions on the B site show an enormous variety of intriguing electronic or magnetic properties. This variety is not only related to their chemical flexibility, but also to a larger extent related to the complex character that transition metal ions play in certain coordinates with oxygen or halides [17]. While magnetism and electronic correlations are usually related to unfilled 3d electron shells, multiferrocity, a coexistence of spontaneous ferroelectric and ferromagnetic moments, is a rare phenomenon due to the small number of low-symmetry magnetic point groups that allow a spontaneous polarization [18]. Nevertheless, in the presence of competing interactions [19], canted moments [20, 21] or in composites [22], large magneto-capacitive couplings have been reported. A few examples of material properties are listed in which transition metal perovskites and related structures prove to be outstanding. The magnetism or

orbital ordering phenomenon of various kinds are observed in perovskites with transition metal ions that have unfilled 3d electron shells. The electronic correlations of such 3d states are generally strong, as the ratio U_d/W of the Coulomb repulsion energy U_d v/s the bandwidth W is larger compared to other electronic states, i.e., they have a more local character and a tendency for insulating states or metal-insulator transitions [23]. Hopping and superexchange of these electrons takes place via oxygen sites due to the overlap of the respective wave function. Thereby, the properties and phase diagrams of a perovskite strongly depend on nonstoichiometries and even more on tilting or distortions of the $[\text{BO}_6]$ octahedra. The further aspects rely on the order/disorder processes of the orbital part of the 3d wave function, charge doping and charge/orbital inhomogeneous states that lead to a colossal response, e.g. to external magnetic fields [24].

Electronic interactions in perovskites are of the **Direct Exchange** and **Indirect Exchange** type:

1.4.1 Direct Exchange

Five d orbitals of a transition-metal atom B are degenerate, however with more than one electron in the d manifold, the spin degeneracy is removed by the ferromagnetic direct exchange interaction between electron spins in atomic orthogonal orbitals. These exchange interactions together with minimization of the electron-electron coulomb energies produce the Hund intra-atomic exchange field H_{ex} . The exchange splitting between spin states is designated by Δ_{ex} .

The atomic orbitals $f_m = R_{nl}(r)P_l^m(\cos\theta)\exp(\pm im\phi)$ with azimuthal angular dependencies for $l = 2$ (d orbitals)

$$f_0 \sim \frac{(\cos^2\theta - 1) \sim [(z^2 - x^2) + (z^2 - y^2)]}{r^2},$$

$$f_{\pm} \sim \sin 2\theta \exp(\pm i\phi) \sim (yz \pm izx)r^2, \quad (1.5)$$

$$f_{\pm} \sim \sin^2 \theta \exp(\pm 2i\phi) \sim [(x^2 - y^2) \pm ixy]r^2$$

In an ideal cubic perovskite with the B-O-B bond angle $\theta = 180^\circ$, the xy and $(yz \pm izx)$ orbitals of a transition metal atom B only overlap the ligand O-2p $_{\pi}$ orbitals while the $[(z^2 - x^2) + (z^2 - y^2)]$ and $(x^2 - y^2)$ orbitals only overlap the O-2s, 2p $_{\sigma}$ orbitals. The expectation values $b^{ca} \equiv (f_{ca}, H' \phi_o) \approx \epsilon_{mo}(f_m, \phi_o)$ for a virtual charge transfer from an O $^{2-}$ ion back to an empty B-d orbital f_m is proportional to the overlap integral (f_m, ϕ_o) between f_m and the same-symmetry sum of nearest neighbour oxygen orbitals ϕ_o ; ϵ_{mo} is a one-electron energy that increases with the perturbation energy H' of the oxygen-orbital potential energies by the B atom. The b_{σ}^{ca} for σ -bonding are larger than the b_{π}^{ca} for π -bonding. Therefore, the antibonding states of a σ -bond are raised higher than those of a π -bond and, as a consequence, the cubic symmetry of the octahedral site raises the two-fold-degenerate pair of σ -bonding orbitals, the $[(z^2 - x^2) + (z^2 - y^2)]$ and $(x^2 - y^2)$ orbitals, above the three-fold-degenerate set of π -bonding orbitals xy , $(yz \pm izx)$ by an energy Δ_{ex} , which quenches the orbital angular momentum associated with $m = \pm 2$.

If a point-charge ionic model places the empty d orbitals of a degenerate manifold, an energy ΔE_p above the anion-p orbitals, the antibonding d-like states can be described by a second-order perturbation theory to give the ligand-field wavefunctions:

$$\begin{aligned} \psi_t &= N_{\pi}(f_t - \lambda_{\pi}\phi_{\pi}), \\ \psi_e &= N_{\sigma}(f_e - \lambda_{\sigma}\phi_{\sigma} - \lambda_s\phi_s), \end{aligned} \quad (1.6)$$

provided the covalent-mixing parameters are $\lambda_{\pi} \equiv b_{\pi}^{ca}/\Delta E_p \ll 1$ and $\lambda_{\sigma} \equiv b_{\sigma}^{ca}/\Delta E_p \ll$

1. A larger ΔE_s makes $\lambda_s < \lambda_\sigma \ll 1$, where the above equation is applicable. According to the second-order perturbation theory, the antibonding states are raised by an energy $\Delta\epsilon = |b^{ca}|^2/\Delta E_p$ by the B-X covalent bonding, and the cubic-field splitting of the e and t orbital energies is:

$$\Delta_c = \Delta\epsilon_\sigma - \Delta\epsilon_\pi = \Delta_B + (\lambda_\sigma^2 - \lambda_\pi^2)\Delta E_p + \lambda_s^2\Delta E_s, \quad (1.7)$$

where Δ_B is a small, purely electrostatic energy that is reduced to uncertain sign as a result of penetration of the O^{2-} -ion electron cloud by the cation wavefunctions. In the perovskite structure, such an interaction between the ψ_t orbitals and the A-site cation orbitals is found to lower ϵ_π and increase Δ_c .

In oxides, the cubic-field splitting Δ_c and the intra-atomic exchange splitting Δ_{ex} are of comparable magnitude, and the d^4 to d^7 configurations may be either HS t^3e^1 , t^3e^2 , t^4e^2 , t^5e^2 , where $\Delta_{ex} > \Delta_c$; or LS t^4e^0 , t^5e^0 , t^6e^0 , t^6e^1 , where $\Delta_c > \Delta_{ex}$. The covalent mixing of the O-2p wavefunctions into ψ_t and ψ_e lowers Δ_{ex} and increases Δ_c , which indicates that a smaller ΔE_p and a larger radial extension of the d wavefunctions favours the LS over the HS state. Consequently, the 4d-block and 5d-block B atoms have LS configurations.

The cubic-field splitting is also found to influence the placement of the redox energies of the transition-metal B cations. On going to heavier atoms of a given d-block, the larger nuclear charge stabilizes the d-electron manifold for a given valence state. Where the cubic-field splitting leaves an orbital degeneracy, a JT local site distortion removes this degeneracy so as to stabilize the electronic configuration. Therefore, ions that have an orbital degeneracy in cubic symmetry are called JT ions. However, a local site distortion is

opposed in a crystal by elastic forces that favour higher symmetry, so the distortion only occurs at lowest temperatures unless there is large enough concentration of the JT ions to allow cooperative JT distortions to reduce the opposing elastic forces. Where the orbital angular momentum is not quenched, a long-range magnetic order can give a cooperative JT distortion through the spin-orbit coupling $\lambda L.S$ even where the concentration of JT ions is small. This distortion is known as magnetostriction. Cooperative JT distortions induce a crystallographic distortion that is superimposed on any distortion introduced by cooperative rotations of the $BO_{6/2}$ octahedra.

Itinerant Electron Ferromagnetism

A simple Heisenberg model has several shortcomings such as: (1) The sign of the exchange integral can be evaluated only in the limits of very high or very low temperatures. It is extremely difficult to evaluate this integral near a phase transition where it is of greatest interest and (2) It fails to explain the non integral value of the Bohr magneton number per atom observed in Fe, Co, and Ni. The band theory of ferromagnetism first proposed by Stoner [25] and independently by Slater [26], gave satisfactory explanation for the non integral value of magnetic moment per atom, particularly for case Co and Ni. In this case, 3-d electrons are considered to form a band, just as the 4s electrons form the conduction band. The 3d electrons are thus itinerant and free to move in the entire lattice. Due to exchange energy, the 3d band is split into two halves with opposite spins. The larger the exchange energy, the greater the difference between the two bands. Along with the non integral values of atomic magnetic moments, the band theory explained successfully many features of magnetic order in the 3-d elements and alloys.

1.4.2 Indirect Exchange

Interactions between the localized $4f^n$ configurations on neighbouring A-site cations is weak as also are those between an A-site $4f^n$ and B-site d^n configuration except for the special case where the energy of a $4f^n$ configuration overlaps a partially filled d band. In the absence of heavy B-Group metals, the inter-atomic interactions of particular interest are those between d electrons on the neighbouring transition-metal ions B. On the other hand, interactions between 5s or 6s orbitals on neighbouring group-B metals on the B-sites give rise to a narrow conduction band accessible to reduction; however the electrons in these bands usually segregate into localized s^2 cores since the on-site electron-electron coulomb energies U_s between spin-paired s^2 electrons is relatively small.

In the perovskite structure, the dominant interactions between B-cation 3d electrons are normally the $(180^\circ-\phi)$ B-X-B interactions. These interactions are between the non-orthogonal orbitals and therefore involve virtual or real electron transfers. The spin-independent resonance integrals that describe an electron transfer between B atoms at R_i and R_j are:

$$b_\pi^{cac} \equiv (\psi_{ti}, H' \psi_{rj}) \approx \epsilon_\pi \lambda_\pi^2, \quad (1.8)$$

$$b_\sigma^{cac} \equiv (\psi_{ei}, H' \psi_{ej}) \approx \epsilon_\sigma \lambda_\sigma^2$$

where, in the absence of a heavy group-B metal on the A-site, ψ_t and ψ_e are given by equation (5), H' is the perturbation of the potential at R_j caused by the presence of an atom at R_i .

The interactions between localized spins on neighbouring atoms are treated by a perturbation theory in which the spin dependent resonance integrals for parallel and

antiparallel coupling of spins are [27, 28]

$$\begin{aligned} t_{ij}^{\uparrow\uparrow} &= b^{cac} \cos\left(\frac{\theta_{ij}}{2}\right), \\ t_{ij}^{\uparrow\downarrow} &= b^{cac} \sin\left(\frac{\theta_{ij}}{2}\right) \end{aligned} \quad (1.9)$$

for electron transfer between atoms whose spins are rotated by an angle θ_{ij} with respect to one another. The spin angular momentum is conserved in an electron transfer.

Interactions between localized spins on neighbouring like atoms involve virtual charge transfers of two types: a transfer between configurations d^n at the cost of an energy U_{eff} to create a polar state d^{n+1} called the **superexchange**, while the transfer of two electrons from an O^{2-} ion, one to each of the two B atoms on opposite sides and each at the cost of the charge-transfer energy $\Delta = \Delta E_p$, is called **semicovalent** exchange. Here, two cases can be distinguished: antiferromagnetic interactions between half-filled orbitals and the ferromagnetic interactions between half-filled and empty or full orbitals. Both, the **superexchange** and **semicovalent** exchange give the same rules for the sign of these spin-spin interactions.

The electron transfers to half-filled orbitals on the B atoms, be it from a neighbouring B atom or from an O^{2-} ion, are constrained by the Pauli exclusion principle to be antiferromagnetic to the spin on the receptor cations and the two electrons of a common p_π or p_σ orbital are spin-paired. Therefore, in the second-order perturbation theory, the interaction between the two half-filled orbitals is antiferromagnetic.

On the other hand, the electron transfer to an empty orbital is not constrained by the Pauli exclusion principle, but the Hund intra-atomic exchange field H_{ex} stabilizes the transfer of a spin parallel to that on the receptor ion over that of an antiparallel spin by an energy Δ_{ex} . Hence, the interaction between a half-filled and an empty orbital is

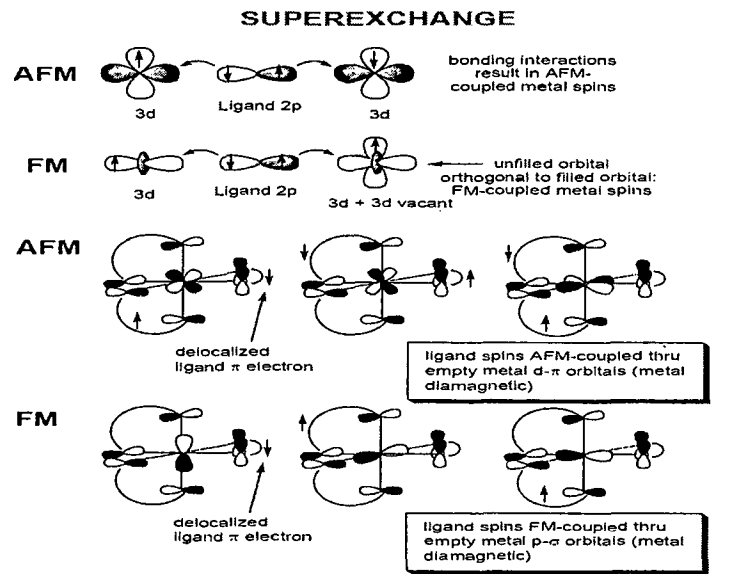


Figure 1.5: The mechanism of Super exchange.

ferromagnetic and is given by the third-order perturbation theory.

Double Exchange

Interactions involving a real charge transfer are called double exchange; the charge transfer is between two different valence states of the same B atom. The real charge transfer is described by first-order perturbation theory with Δ_{ex} stabilizing a spin transfer between localized spins with ferromagnetic alignment:

$$\Delta_{ex}^D \approx -z(1-c)ct_{ij} \uparrow\uparrow = -z(1-c)cb_{ij}^{cac} \cos(\theta_{ij}/2), \quad (1.10)$$

where c is the fraction of reduced B atoms with d^{n+1} and $z(1-c)$ is the fraction of B-like nearest neighbours with configuration d^n .

The indirect exchange is a coupling of the localized spins at B atoms by a partially occupied broad band where Δ_{ex} is not large enough to remove totally the spin degeneracy of the broad band at the B atom. This interaction is ferromagnetic at small $k_F R$, where

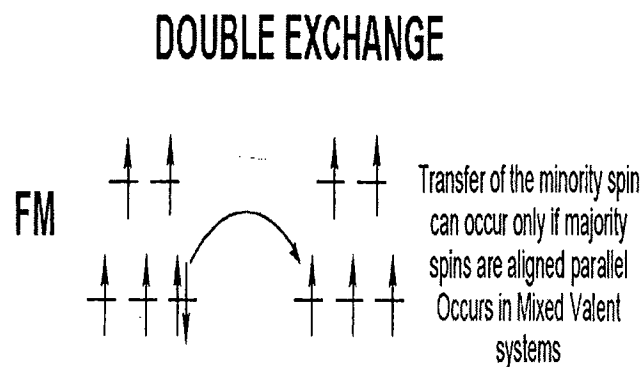


Figure 1.6: The mechanism of Double exchange.

R is the separation between B atoms and $\hbar k_F$ is the charge carrier momentum at the Fermi energy; it becomes antiferromagnetic at larger $k_F R$.

The most general form of the bilinear spin-spin coupling between two localized spins S_i and S_j on neighbouring atoms is $V_{ij} = S_i \cdot K_S \cdot S_j + S_i \cdot K_A \cdot S_j$, where K_S and K_A represent symmetric and antisymmetric tensors. The first term remains invariant under the interchange of two spins whereas the second term changes sign. Dzialoshinskii [31] was the first to point out that the antisymmetric term, which may be written as:

$$\Delta_{ex}^A = -2D_{ij} \cdot S_i \times S_j \quad (1.11)$$

is allowed under the symmetry constraint that the magnetic energy be invariant under all symmetry operations of the magnetic point group. The applications of this symmetry requirement determines the allowed direction of the vector D_{ij} with respect to the crystal axes. The antisymmetric exchange term cants the antiferromagnetically coupled spins to give a net ferromagnetic component in a direction perpendicular to D_{ij} . The magnitude of the cant depends on the relative magnitudes of the antisymmetric and symmetric exchange

terms. Where the spin-orbit coupling is a second order effect (orbital angular momentum quenched in the ground state), Moriya [32] has calculated a $D_{ij} \approx (\Delta g/g)J_{ij}$, where g is the spectroscopic splitting factor and $\Delta g = (g-2)$. The spin canting of a few degrees in this case gives a weak intrinsic ferromagnetic component below an antiferromagnetic Neel temperature T_N . On the other hand, if the spin-orbit coupling enters in first-order theory, then it is possible to have $D_{ij} \approx J_{ij}$ and the right-angle nearest-neighbour coupling usually found between rare earth spins in perovskites. A large ferromagnetic component due to spin canting of an antiferromagnetic array can, in principle, occur if an antiferromagnetic superexchange interaction varying as $\cos \theta_{ij}$ competes with a double-exchange interaction varying as $\cos(\theta_{ij})/2$.

1.5 Scope of the Present Study

1.5.1 Ruthenium Double Perovskites

Mixed ruthenates with perovskite-based crystal structures have been receiving considerable attention of late [33, 34, 35, 36, 37, 38, 39, 40, 41, 42, 43, 44, 45, 46, 47, 48, 49, 50, 51, 52, 53, 54, 55, 56, 57, 58, 59, 60], both because of their interesting magnetic properties and because of the recent discovery of superconductivity in the layered ruthenate Sr_2RuO_6 [48]. Despite the rarity of 4d-based magnetic materials, SrRuO_3 is a robustly (Curie temperature $T_C \approx 165\text{K}$, magnetization $M \approx 1.6\mu_B/\text{Ru}$) ferromagnetic metal occurring in a distorted cubic perovskite structure. Further, Sr_2YRuO_6 , which has essentially the same crystal structure as SrRuO_3 , but with every second Ru substituted by Y, is antiferromagnetic. The variety of electronic and magnetic properties observed in these superficially similar compounds already possess an interesting theoretical challenge like for instance, nonsuperconducting cuprates, which despite their large variety, always show

strong antiferromagnetism. Besides, there exist a number of interesting observations that require attention, these include the fact that SrRuO_3 is the only known ferromagnetic material among the $4d$ oxides. As such interesting differences are expected from the much more abundant $3d$ oxide magnets. For example, much stronger spin-orbit effects compared to the $3d$ systems may be anticipated, and these may manifest themselves in the magnetocrystalline and magneto-optical properties. Additional interest in these ruthenates comes from their apparent proximity to superconductivity, and possible new insights into the problem of high-temperature superconductivity that may emerge from their study.

$\text{La}_2\text{CoRuO}_6$ is a double perovskite that crystallizes in the $P2_1/n$ superstructure commonly found in double perovskites wherein the $P2_1/n$ space group accommodates a rock-salt form of arrangement of Co and Ru and describes the $a^+b^-b_-$ system of three octahedral tilts in the Glazier notation. Antiparallel collinear magnetic structures with perpendicular Co and Ru sublattices have been suggested for systems such as LaMCoRuO_6 , ($M = \text{Ca}$ and Sr) the models being consistent with the presence of dominant linear σ Co-O-Ru-O-Co superexchange via the vacant e_g orbitals on Ru. Symmetric exchange coupling between the Co and Ru sublattices is frustrated, leaving weaker antisymmetric interactions to determine the perpendicular arrangement of Co and Ru sublattice moments. The $\text{La}_2\text{CoRuO}_6$ system is found to follow two collinear and two non-collinear models, the magnitudes of the Co and Ru moments are not uniquely determined, however are found to vary from the Co only to the Ru only solutions. Both the solutions are found to be plausible with a reduction in magnetic moments being attributed to be entirely due to magnetic frustrations. The magnetic frustrations are found to arise due to increasing A-cation size

that leads to a strong reduction in T_N and a saturated Co moment, the frustration arising from competing 90°C exchange interactions between the Co sublattices in which the stronger 180°C interactions are satisfied. As compared to LaSrCoRuO_6 ($T_N=85\text{K}$) and LaCaCoRuO_6 ($T_N=96\text{K}$), a lower $T_N=25\text{K}$ for $\text{La}_2\text{CoRuO}_6$ is **attributed to be due to decreasing covalency from Ru^{5+} to Ru^{4+} which weakens the superexchange interactions.**

On the other hand, Sr_2YRuO_6 belongs to the family of double perovskite insulators, $\text{Sr}_2\text{LnRuO}_6$ ($\text{Ln} = \text{rare earth or Y}$)[61], **where the Ru ions exist in the pentavalent state (Ru^{5+})** with a high-spin state and $4d^3$ configuration ($J = 3/2$). Though the structure of these compounds can be derived from the well known perovskite structure SrRuO_3 by replacing alternate Ru ions with Ln ions [62], these compounds do not show any similarity to their parent compound SrRuO_3 which is a ferromagnetic metal. The layered structure, essentially consists of alternating LnRuO_4 and SrO planes, accommodating both the Ru and rare earth atoms in the same LnRuO_4 plane and hence both the atoms share the same site symmetry (B-site of the perovskite structure ABX_3). The alternating positions of the Ru and Ln atoms in the unit cell result in two types of interactions between the Ru atoms; namely: (i) direct interaction of the Ru-O-O-Ru and (ii) indirect interaction through the rare earth atoms, Ru-O-Ln-O-Ru. Since the compounds having nonmagnetic Ln ions (Y and Lu) are also found to order magnetically [62, 63], the direct interaction is assumed to be stronger than the indirect interaction through the rare earth atoms. In the ordered double perovskite $\text{Sr}_2\text{LnRuO}_6$ compounds, the B-site of the perovskite structure ABX_3 is uniquely occupied either by Ru or the rare earth metal ions due to the lower coordination number compared to Sr. With ruthenium being consid-

ered to be in the oxidation state of 5+ in these compounds, the chances of ferrimagnetic ordering of $\text{Ru}^{5+}/\text{Ru}^{4+}$ moments are found to be very rare. The magnetic interactions among the ordered Ru moments can take place in two ways; (i) the σ -super exchange interaction between nearest neighbour (nn) Ru^{5+} via Ru-O-O-Ru pathway and (ii) the Π -super exchange between the next nearest neighbour (nnn) Ru^{5+} ions via Ru-O-Y-O-Ru pathway. With Y being nonmagnetic ion it is not expected to take part in the exchange interaction and hence the second interaction between nnn is assumed to be negligible.

The layered compounds, often characterized by strong competition between antiferromagnetic and ferromagnetic coupling and a complex interplay of spin, charge and orbital degrees of freedom, are extremely sensitive to small perturbations such as slight structural alterations. Sr_2YRuO_6 is a typical example, where negative magnetization is observed in low fields has been ascribed to two oppositely ordered ferromagnetic superexchange interactions, Ru-O-O-Ru and Ru-O-Y-O-Ru [64]. The perovskite LaSrCoRuO_6 attracts attention because of the interplay of the cationic order, charge balance and complex magnetic interactions between transition metal ions. The crystal structure consists of a pseudocubic array of corner-shared CoO_6 and RuO_6 octahedra, which are in an ideal case ordered in a rocksalt arrangement forming, thus the so-called double perovskite. It is a type of layered compound wherein degree of B-site (Co and Ru) order can lead to intriguing magnetic and transport properties [6, 8]. However, unlike the Y, Co is a magnetic ion and that has led to different interpretations of the nature of magnetic order in this compound. Presence of two magnetic cations introduces additional magnetic exchange paths, the linear Co-O-Ru-O-Co and the perpendicular Ru-O-O-Ru and Co-O-O-Co [6]. It was first reported to be a 3D variable range hopping semiconductor with magnetic

ordering temperature of 157K [67]. However, recent studies have suggested that the compound is an antiferromagnet with a $T_N = 87\text{K}$ [6] or a spin glass [8] and the transition at 157K could be due to SrRuO_3 impurity. Both these studies highlight the importance of the degree of B-site order in governing the magnetic ground state. Although ferromagnetism should dominate with increasing disorder, studies by Mamchik et al report to the contrary and therefore the necessity to understand such behavior.

Alterations of A and B-site compositions can lead to a change in valence states of Co and Ru and that plays an important role in the magnetic properties of these compounds. Apart from SrRuO_3 impurity phase, the sharp rise in magnetization can also be due to ferromagnetic Ru-O-Ru interactions arising from anti-phase grain boundaries [68]. The studies conducted so far on LaSrCoRuO_6 by varying the composition ratio of A site ions (La and Sr) highlight the importance of different magnetic interactions between $\text{Co}^{2+/3+}$ and $\text{Ru}^{4+/5+}$ in governing the magnetic ground state [8, 69]. The charge transfer between Ru and Co in LaSrCoRuO_6 is very sensitive to local atomic structure such as cation order [6, 69]. Any disturbance in this cation order leads to compensation of antiferromagnetic interactions by the ferromagnetic interactions most likely associated with Ru-O-Ru interactions. Hence the main aim of this thesis is to study the effect of thermal and substitutional disorder on the structural, magnetic and transport properties of archetype double perovskite LaSrCoRuO_6 .

Disorder in LaSrCoRuO_6 can be introduced either by changing the composition ratios of A-site or B-site cations or a thermal disorder. Thermal disorder is expected to have least complications as the compound essentially remains compositionally identical. It is therefore interesting to see the effect of such a disorder on the magnetic and

transport properties of LaSrCoRuO_6 . Chapter 3 reports the effect of thermally induced site-occupancy disorder in LaSrCoRuO_6 on its magnetic properties. The most notable feature that we see here is the observation of negative magnetization at low applied fields in the more disordered sample. The results have been explained on the basis of EXAFS data recorded at Co and Ru K-edge to be due to presence of additional ferromagnetic interactions resulting from B-site disorder in an otherwise antiferromagnetic lattice.

In Chapter 4 detailed investigations carried out on the structural, magnetic and transport properties of solid solutions of SrRuO_3 and LaCoO_3 which form double perovskite compounds of the type $\text{La}_{2x}\text{Sr}_{2-2x}\text{Co}_{2x}\text{Ru}_{2-2x}\text{O}_6$, where $0.25 \leq x \leq 0.75$ are described. This study elucidates the effect of delicate charge balance achieved in solid solutions of LaCoO_3 and SrRuO_3 by conversion of Co^{3+} to Co^{2+} and oxidation Ru^{4+} to Ru^{5+} due to formation of double perovskite structure.

Effect of substitutions at the B or B' sites in LaSrCoRuO_6 have not been studied so far. In particular, the effect of antisite disorder will be very important as it will alter the magnetic interactions present in LaSrCoRuO_6 and perhaps result in more complex magnetic ground state. Antisite disorder in ferromagnetic double perovskites like $\text{Sr}_2\text{FeMoO}_6$ is known to affect magnetic and transport properties of these compounds. Chapter 5 reports structural, transport and magnetic properties of $\text{LaSrCo}_{1-x}\text{Ru}_{1+x}$ for $-0.3 \leq x \leq 0.4$ and $\text{LaSrCo}_{1-y}\text{Cu}_y\text{RuO}_6$ $y \leq 0.2$ studied using X-ray diffraction (XRD), Neutron diffraction (ND), resistivity and magnetization as a function of temperature and magnetic field. The compounds studied herein have a fixed A-site variance though varying tolerance factor t and redox active $\text{Co}^{2+/3+}$ and $\text{Ru}^{4+/5+}$ couples resulting essentially due to antisite disorder. This study elucidates the complex role of coexisting localized

electrons belonging to both Co and Ru *d* orbitals as well as some itinerant π^* electrons of Ru: t_{2g} parentage that arise due to presence of Ru^{4+/5+} and Co^{2+/3+} redox couples on the structural, magnetic and transport properties of substituted LaSrCoRuO₆.

Finally in chapter 6 a comparison between the properties of LaSrCoRuO₆ and LaCaCoRuO₆ has been made to understand the role of Sr in modifying electronic band structure of Ru and its effect on magnetic and transport properties of these double perovskites.

References

- [1] A. Navrotsky, D. J. Weidner, Preface. In *Perovskite: A Structure of Great Interest to Geophysics and Material Science*, Eds. American Geophysical Union: Washington D.C., Vol. 45, 1989, p xi.
- [2] V.M. Goldschmidt, *Naturwissenschaften* **14**, 477-485 (1926).
- [3] A.S. Bhalla, R. Guo and R. Roy, The perovskite structure- a review of its role in ceramic science and technology, *Mat. Res. Innovat.* **4**, 3-26 (2000) and references therein.
- [4] R. D. Shannon and C. T. Prewitt, *Acta Crystallogr B*, **25**, 725 (1969); Shannon R D and Prewitt C T, *Acta Crystallogr, B* **26**, 1046 (1970).
- [5] J. B. Goodenough, J. A. Kafalas and J. M. Longo, *Preparative Methods in Solid State Chemistry* ed P Hagenmuller, (New York: Academic) chapter 1 1972.
- [6] H.K. Mao, R.J. Hemley, Y. Fei, J.F. Shu, L.C. Chen, A.P. Jephcoat and Y. Wu, *J. Geophys. Res.*, **96**, 8069 (1991)
- [7] A. Katrusiak and A. Ratuszna, *Solid State Commun.*, **84**, 435 (1992)
- [8] J.B. Goodenough, *Structure Bonding*, **98**, 1 (2001); J.B. Goodenough and J-S Zhou, *Structure Bonding*, **98**, 17 (2001)

- [9] J. Longo and R. Ward ,J. Am. Chem. Soc., **83**, 2816-2818 (1961)
- [10] K. I. Kobayashi ,T. Kimura , Y. Tomioka ,H. Sawada , K. Terakura and Y. Tokura,
Nature, **395**, 677-680 (1998)
- [11] K. I. Kobayashi , T. Kimura , Y. Tomioka , H. Sawada ,K. Terakura and Y. Tokura
,Phys. Rev.B, **59**, 11159-62 (1999)
- [12] A. M. Glazer , Acta Crystallogr, **28**, 3384-96 (1972)
- [13] R. D. Shannon ,Acta Crystallogr. A, **32**, 751-67 (1976)
- [14] M. Soda , Y. Yasui , T. Fujita , T. Miyashita , M. Sato and K. Kakurai, J. Phys.
Soc. Japan, **72**, 1729 (2003)
- [15] S. V. Trukanov , I. O. Troyanchuk , M. Hervieu, H. Szymezak and K. Barner ,Phys.
Rev. B ,**66**, 184424 (2002)
- [16] P.W.Anderson, Phys.Rev, **2**, 115 (1959)
- [17] P. Lemmens and P. Millet ,Spin-Orbit-Topology,a triptych, in "Quantum Mag-
netism", Springer, Heidelberg, (2004).
- [18] H.Schmid ,Ferroelectrics, **162**,317 (1994).
- [19] J. Hemberger , P. Lunkenheimer , R. Fichtl , H.A.K. von Nidda , V.Tsurkan and
A. Loidl , Nature, **434**, 364 (2005)
- [20] T. Kimura , T. Goto , H. Shintani , K. Ishizaka ,T. Arima and Y. Tokura ,Nature,
426, 55 (2003)

- [21] D. Higashiyama ,N. Kida ,T. Miyasaka ,T. Arima , and Y. Tokura ,Phys.Rev.B, **70**,174405 (2004)
- [22] H. Zheng ,J. Wang ,S.E. Lofland ,Z. Ma ,Mohaddes-Ardabili, T. Zhao ,L. Salamanca-Riba , S.R. Shinde , S.B. Ogale ,F. Bai , D. Viehland , Y. Jia , D.G. Schlom ,M. Wuttig , A. Roytburd , and R. Ramesh , Sciences, **303**, 661 (2004).
- [23] M.Imada , A. Fujimori ,A. Tokura ,Rev.Mod.Phys., **70**, 1039 (1998)
- [24] Y.Tokura ,Physics Today, **56**, 50 July (2003)
- [25] E.C. Stoner , Phil.Mag., **15**, 1080 (1933)
- [26] J.C. Slater ,Phys.Rev.,**49**, 537 (1936)
- [27] P.W.Anderson,Phys.Rev, **79**, 350 (1950)
- [28] P.W.Anderson and H. Hasegawa, Phys.Rev, **100**, 675 (1955)
- [29] H. Kramers ,Physica, **1**, 182 (1934)
- [30] P.W. Anderson ,Solid State Physics, **14**, 99 (1963)
- [31] I.E. Dzialoshinskii, J.Phys.Chem.Solids, **4**, 241 (1958)
- [32] T.Moriya, Phys.Rev, **120**, 91 (1960)
- [33] C.B. Eorn ,R.J. Cava ,J.M. Fleming ,R.B. van Dover ,J.H. MarChem.Solidsshall , J.W.P. Hsu , J.J. Krajewski , and W.F. Peck ,Sciences, **258**, 1766 (1992)
- [34] D. Kirillov , Y. Suzuki, K. Antognazza ,K. Char ,I. Bozovic , and T.H. Geballe , Phys.Rev.B, **51**, 12 825 (1995)

- [35] M. Shikano ,T.K. Huang ,Y.Inaguma , M. Itoh , and T. Nakamura ,Solid State Commum., **90**, 115 (1994)
- [36] M. Itoh , M. Shikano,and T. Shimura ,Phys.Rev.B., **51**, 16 432 (1995)
- [37] L. Klein ,J.S. Dodge , T.H. Geballe , A. Kapitulnik, A.F.Marshall ,Antognazza, and K. Char ,Appl.Phys.Lett, **66**, 2427 (1995)
- [38] D.J. Singh ,J.Appl.Phys **79**, 4818 (1996)
- [39] J.J. Neumeier ,A.L. Cornelius , and J.S. Schilling ,Physica B, **198**, 324 (1994)
- [40] S.A. Carter ,B. Batlogg ,R.J. Cava ,J.J. Krajewski ,W.F. Peck ,Jr.,and L.W. Rupp ,Jr.,Phys.Rev.B, **51**,17 184 (1995)
- [41] J.S. Gardner ,G. Balakrsihnan , and D.M.K. Paul ,Physica C, **252**, 303 (1995)
- [42] A. Gulino ,R.G. Egdell , P.D. Battle , and S.H. Kim ,Phys.Rev.B, **51**, 6827 (1995)
- [43] S.C. Gausepohl , M. Lee ,K. Char ,R.A. Rao , and C.B. Eorn ,Phys.Rev.B, **52**, 3459 (1995)
- [44] S.C. Gausepohl ,M. Lee ,R.A Rao , and C.B. Eorn , Phys.Rev.B, **54**, 8996 (1996)
- [45] G. Cao,S.McCall,J.Bolivar,M.Shepard,F.Freibert,P.Henning,J.E.Crow and T.Yuen,Phys.Rev.B **54**,15 144 (1996).
- [46] J.H. Cho , Q.X. Jia ,X.D. Wu ,S.R. Foltyn , and M.P. Maley, Phys.Rev.B, **54**, 37 (1996)
- [47] L. Klein ,J.S. Dodge ,C.H. Ahn , G.J. Snyder , T.H. Geballe ,M.R. Beasley ,and A. Kapitulnik , Phys.Rev.Lett, **77**, 2774 (1996)

- [48] Y. Maeno , H. Hashimoto , K. Yoshida ,S. Nishizaki ,T. Fujita , J. G. Bednorz and F. Lichtenberg, *Nature (London)*, **372**, 532 (1994)
- [49] T. Oguchi ,*Phys.Rev.B*, **51**, 1385 (1995)
- [50] D.J. Singh ,*Phys.Rev.B*, **52**, 1358 (1995)
- [51] T. Vogt , and D.J. Buttrey , *Phys.Rev.B*, **52** ,R9843 (1995)
- [52] N. Shirakawa , K. Murata ,Y. Nishihara , S. Nishizaki ,Y. Maeno ,T. Fujita ,J.G. Bednorz ,F. Lichtenberg , and N. Hamada , *J.Neurphysiol*, **64**, 1072 (1995)
- [53] M. Schmidt ,T.R. Cummins ,M. Burk , D.H. Lu ,N. Nucker ,S. Schuppler , and F. Lichtenberg ,*Phys.Rev.B*, **53**, R14 761 (1996)
- [54] A.P. Mackenzie , A.J. Julian ,G.J. McMullan ,M.P. Ray , G.G. Lonzarich ,Y. Maeno , S. Nishizaki , and T. Fujita ,*Phys.Rev.Lett*, **76**, 3786 (1996)
- [55] T. Yokoya , A. Chainami ,T. Takahashi ,H. Katayama-Yoshida ,M. Kasai , Y. Tokura , N. Shanthi , and D.D. Sarma ,*Phys.Rev.B*, **53**, 8151 (1996)
- [56] T. Yokoya ,A. Chainami ,T. Takahashi , H. Katayama-Yoshida ,Kasai M., and Tokura Y.,*Phys.Rev.Lett*, **26**, 3009 (1996)
- [57] Lu D.H.,Schmidt M., Cummins T.R., Schuppler S., Lichtenberg F., and Bednorz J.G.,*Phys.Rev.Lett*, **76**, 4845 (1996)
- [58] T.M Rice , and M. Sigrist,*J.Phys. Condens.Matter*, **7**, L643 (1995)
- [59] P.B. Allen, H. Berger,O. Chauvet,L. Forro,T. Jarlborg,A. Junod,B. Revaz, and G. Santi, *Phys.Rev.B*, **5**, 4393 (1996)

- [60] T. Kiyama, K. Yoshimura, K. Kosuge, Y. Ikeda, and Y. Bando, *Phys.Rev.B*, **54**, R756 (1996)
- [61] P.C.Donohue and E.L.McCann, *Mat. Res. Bull.*, **12**, 519 (1977).
- [62] P.D.Battle and W.J.Macklin, *J. Solid State Chem.*, **52**, 138 (1984)
- [63] P.D.Battle and C.W.Jones, *J.Solid State Chem*, **78**, 108 (1989)
- [64] R. P. Singh and C. V. Tomy , *Phys. Rev. B*, **78**, 024432 (2008)
- [65] J-W. G Bos .,J. P. Attfield, *Chem. Matter.*, **16**, 1822 (2004)
- [66] A. Mamchik , W. Dmowski , T. Egami , I-W. Chen , *Phys. Rev. B*, **70**, 104410 (2004)
- [67] S. H. Kim , P. D. Battle , *J. Sol. State Chem.*, **114**, 174 (1995)
- [68] S. Kim , R. I. Dass and J. B. Goodenough , *J. Sol. State Chem.* **181**, 2989 (2008)
- [69] P. Tomes , Hejtmanek and K. Knizek, *Sol. State Sci.*, **10**, 486 (2008)

Chapter 2

Experimental Techniques

2.1 Introduction

The aim of this chapter is to introduce the reader to all the experimental work carried out in this thesis with regard to the study of some of the double perovskites that are mentioned in the latter chapters. Along with the sample preparation technique, the method adopted for measurements, basic principle involved and the instruments used for all the experiments, are discussed below. In particular, to study the crystal structure and magnetic structure, techniques like X-ray diffraction and Neutron Powder Diffraction were employed. The transport and magnetic properties were investigated using four-probe resistivity and magnetization as a function of temperature and magnetic field. In order to gain an insight into changes occurring in the local structure of constituent atoms, X-ray absorption fine structure (XAFS) study has been undertaken.

2.2 Sample Preparation Technique

There are several techniques available that allow obtaining single-phase double perovskite samples. One can mention the wet chemistry methods (sol-gel) or solid-state reaction method. The Physical properties of the samples synthesized with different methods

can differ. However, this applies mostly to the microstructure and electrical transport properties.

2.2.1 Solid State Synthesis of Ceramic Samples

All the polycrystalline samples were synthesized by the standard solid state reaction method by taking stoichiometric amounts of La_2O_3 , SrCO_3 , $\text{Co}(\text{NO}_3)_2 \cdot 6\text{H}_2\text{O}$, CuO and RuO_2 . These starting powders were ground thoroughly, pressed into pellets and heated for a total of 48 hours at 1200°C and 1300°C with three intermediate regrinding steps. Prior to firing, the powders of La_2O_3 , RuO_2 and SrCO_3 were pre-heated at 900°C and 700°C respectively to get rid of any adsorbed water.

2.3 Diffraction Methods

Diffraction methods have become a fundamental tool for the structural characterization and they have also been applied to the samples studied in this thesis. The X-ray diffraction (XRD) and Neutron Powder Diffraction (NPD) allow studying the long range ordering and thus a determination of the crystallographic structure on the one hand, and the deviations from a perfect ordering on the other hand. The usefulness of both the short x-rays and neutrons arises from the possibility to tune their wavelength so that it closely matches the interatomic distances in the solid (i.e. becomes of the order of ($\sim 1\text{\AA}$)).

2.3.1 X-ray Diffraction

X-ray diffraction is a widely used technique to determine the crystalline phase in the bulk materials. The wavelength of X-ray is comparable to the separation (d) between the crystal planes. Diffraction occurs when the Bragg condition which states that, the X-rays

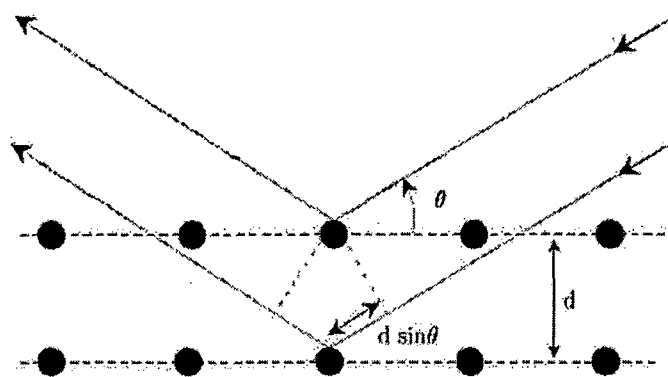


Figure 2.1: The Bragg condition, $2d\sin\theta = n\lambda$, where n is an integer, the extra distance traveled by the x-rays to the farther plane of atoms is equal to the multiple of the X-ray wavelength.

reflected from two neighboring planes of atoms must coherently interfere, is satisfied. This condition is fulfilled when the extra distance traveled by the x-rays to the farther planes of atoms is equal to the multiple of the X-ray wavelength, i.e. $2d\sin\theta = n\lambda$, where n is an integer (as illustrated in the Fig 2.1) giving rise to diffraction in solids [1, 2]. An x-ray diffraction can be carried out on the polycrystalline (powder) samples or single crystals. The XRD pattern is a plot of the intensity of diffracted rays versus Bragg angle and contains information about the structure and composition of the basis. This information needs to be extracted from the pattern by employing a proper analysis procedure.

In the present study, the powder method is made use off wherein the samples were crushed into fine powder in an agate pestle and mortar and placed in a beam of monochromatic X-rays. The powder X-ray diffraction measurements are performed on powder samples using Rigaku X-ray diffractometer system in the department. The intensity of the Copper K_{α} ($\lambda = 1.5418\text{\AA}$) radiation diffracted from the powdered specimen was detected

by a scintillation counter and recorded as a function of 2θ , where θ is the angle of incidence. The patterns were recorded in continuous mode in the 2θ range of $18^\circ \leq 2\theta \leq 80^\circ$ with a step size of 0.02 at a speed of $2^\circ/\text{min}$. The diffraction peaks were indexed using a commercially available Powder Diffraction Package.

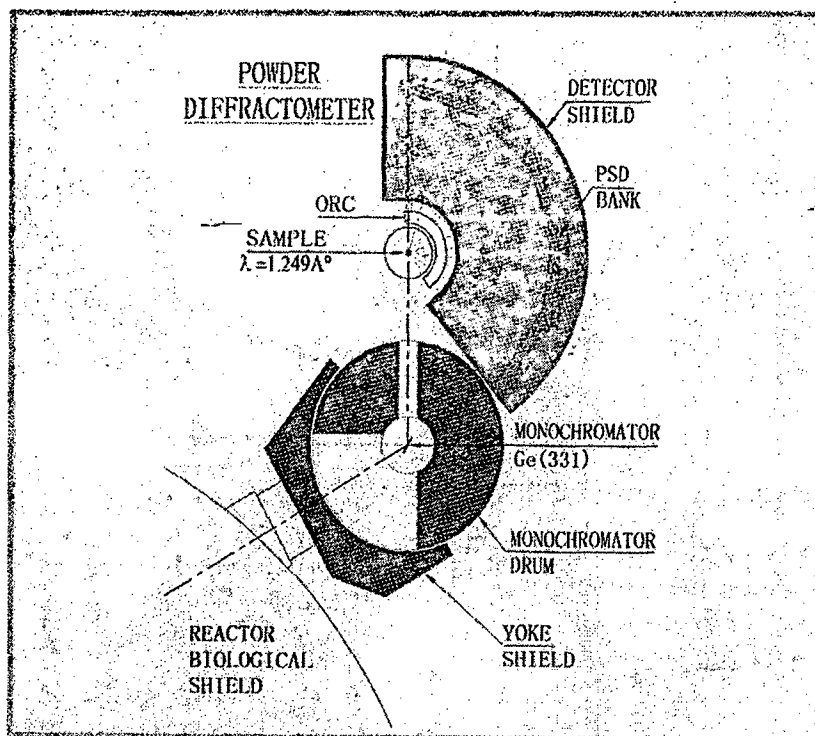
Experimental Set-up for X-ray Diffraction

The diffractometer consists of a x-ray source, a goniometer and a counter. Copper anode was used as the target in the X-ray source. The goniometer is designed to satisfy the focusing conditions geometrically. The sample lies at the center of the focussing circle and the plane of the circle at right angles with the axis of rotation of the goniometer. The plane of focussing circle involves the axis-I of focus of the target, the axis-II of the goniometer and the axis-III of the receiving slit. The radius of the focussing circle is a function of the angle θ formed by the surface of the sample with the extension line of the direct X-ray beam and the angle formed by the straight line connecting the axes II and III in 2θ . This angle is always accurately twice the angle θ formed by the surface of the sample with the extension line of the direct X-ray beam. Since in this goniometer, the X-ray beam from the line focus will irradiate the sample, the greater part of the X-ray beam is irradiated on the sample inclined against the focusing circle plane. When this angle of inclination is large, resolution of the diffracted X-ray beams and accuracy of the measured diffracted angle decreases. To minimize the angle of inclination, the soller slit is used. The soller slit boxes have three slit holders for insertion of the diversion slit, the receiving slit and the scatter slit. The divergence slit determines the horizontal divergence angle of the x-ray beam irradiating the sample. The receiving slit is for limiting the width of diffracted beams entering the counter. It forms a pair with the divergence slit. The x-ray

diffraction measurements were performed on powder samples using diffractometer system. The intensity of the K_{α} radiation diffracted from the powder specimen was detected by a scintillation counter and recorded as a function of the angle 2θ . The diffraction peaks were indexed to determine the crystallographic structures, space groups and lattice parameters of the samples.

2.3.2 Neutron Powder Diffraction

Neutron diffraction is a complementary technique to x-ray diffraction in structural studies. Neutrons interact with the atom nucleus and with the electron spin. Thus, magnetic ions give substantial scattering due to the interaction of the magnetic moment of the neutron with the unbalanced electron spin. The form factor f used in XRD is replaced with the scattering length b having units of length. The factor b is dependent on the nuclear properties of the atom and has no simple correlation with the atomic number. It becomes negative for hydrogen, giving a large contrast when compared to other atoms. Moreover, due to the small size of the nucleus with respect to the thermal neutron wavelength (point-like scattering), there will be no dependence of b with the scattering angle θ . In the case of ferromagnetic and antiferromagnetic materials, below certain ordering temperature, all the magnetic moments will become oriented with respect to some axis, within a magnetic domain. To each magnetic atom, magnetic scattering amplitude D may be ascribed. Consequently apart from the Bragg diffraction peaks, arising from the three-dimensional ordering in crystal structure and nuclear scattering, additional peaks will appear being dependant on the ordering in the magnetic unit cell. If the magnetic unit cell is equivalent to the chemical unit cell, the magnetic and the nuclear Bragg peaks will be located at the same position in 2θ units. On the other hand, if the magnetic cell



Instrument parameters

Beam hole no.	T1013
Monochromator	Ge (331)
Wavelength	1.249 Å
Beam size	4.0 cm x 1.5 cm
Flux at sample	8.5×10^5 n/cm ² /sec
Scattering angle	$4^\circ < 2\theta < 140^\circ$
Q range	$0.4 - 9.4 \text{ \AA}^{-1}$
$\Delta d/d$	$\sim 0.8\%$
Detector	5 PSDs (to be upgraded to 15 PSDs)
Sample environment	10 - 300 K

Figure 2.2: The Neutron Powder Diffractometer at BARC used for neutron diffraction measurements. The description of the instrument parameters can be seen on the right.

does not coincide with the chemical cell, magnetic Bragg peaks will occur in new positions corresponding to a super-structure long-range order. Above the ordering temperature, no magnetic order is present, and thus no long-range magnetic scattering contribution to the diffraction pattern will be present.

The NPD measurements presented in this thesis have been performed using the Powder diffractometer-2 which is a multi-PSD based instrument at the Dhruva reactor of BARC, Mumbai, covering a Q range upto 9.4 \AA^{-1} as seen in the Fig.2.2. This part of the work has been done in close collaboration with Dr. Amitabh Das, SSPD, BARC.

2.4 Bulk Characterization Methods

A large number of macroscopic properties of the material can be investigated easily by means of experimental methods that can be generally called as bulk methods. In the case of materials being investigated in this thesis, these are the magnetometry and the four probe resistivity measurements.

2.4.1 Magnetometry

A large part of the work during the examination of the properties of the double perovskites investigated was dedicated to the magnetic properties of the material. The experiments have been performed both in high and low fields as a function of temperature and temperature ranges but not only under magnetic fields that can be easily obtained with the commercial use devices in the laboratories. Some large experimental facilities allowing the user to achieve very large fields have also been used.

SQUID Magnetometry

Superconducting Quantum Interference Devices (SQUID) are the most sensitive detectors of magnetic flux available. A SQUID is in essence, a flux to voltage transducer, providing an output voltage that is periodic in applied flux with a period of one flux quantum, $\Phi_0 = h/2e \approx 2.07 \times 10^{-15} \text{Wb}$. One is generally able to detect an output signal corresponding to a flux change much less than Φ_0 .

SQUIDs combine two physical phenomena, flux quantization - the fact that the flux Φ in a closed superconducting loop is quantized [3] in units of Φ_0 and second the Josephson tunneling [4]. There are two kinds of SQUIDs. The first [5], the dc SQUID, consists of two Josephson junctions connected in parallel on a superconducting loop and is so

* Fe_2MnGa

~~✗~~ check Ni substitution

✓ (a) Ni - Mn - In

✓ (b) Ni - Mn - Ga

✓ (c) Ni - Fe - Ga

⇒ (d) ~~✗~~ Fe - Mn - Ga

Gemez

The corrections ~~say~~ ^{recommended} by the referees have been
duly carried out

Examined

External Examiner

Guides

named because it operates with a steady state current bias. The second is the rf SQUID [6, 7] which involves a single Josephson junction interrupting the current flow around a superconducting loop and is operated with a radio frequency flux bias.

One of the simplest SQUID based instrument is the magnetometer. A pick-up loop is connected across a input coil to make a superconducting flux transform. The SQUID and the input coil are generally enclosed in a superconducting shield. If one applies magnetic flux $\delta\Phi^p$ to the pick-up loop, flux quantization requires

$$\delta\Phi^p + (L_i + L_p)J_s = 0 \quad (2.1)$$

Here L_i is the inductance of the input coil, L_p is the inductance of the pick-up loop and J_s is the supercurrent induced in the transformer. We have neglected the effects of the SQUID on the input circuit. The flux coupled into the SQUID, which we assume to be in flux locked loop is

$$\delta\Phi = M_i |J_s| = \frac{M_i \delta\Phi^p}{L_i + L_p} \quad (2.2)$$

where M_i is the mutual inductance. We find the minimum detectable value of $\delta\Phi^p$ by equating $\delta\Phi$ with the equivalent flux noise of the SQUID. Defining S_{Φ}^p as the spectral density of the equivalent flux noise referred to the pick-up loop, we find

$$S_{\Phi}^p = \frac{(L_p + L_i)^2}{M_i^2} S_{\Phi} \quad (2.3)$$

Introducing the equivalent noise energy referred to the pick-up loop we obtain

$$\frac{S_{\Phi}^p}{2L_p} = \frac{(L_p + L_i)^2}{L_i L_p} \frac{S_{\Phi}}{2\alpha^2 L} \quad (2.4)$$

We observe that eqn 2.4 has the minimum value

$$\frac{S_{\Phi}^p}{2L_p} = \frac{4\epsilon(f)}{\alpha^2} \quad (2.5)$$

when $L_i = L_p$. Thus a fraction $\alpha^2/4$ of the energy in the pick-up loop is transferred to the SQUID. It must be mentioned here that we have neglected the possible effects arising from noise in the SQUID, the fact that input circuit reduces the SQUID inductance and any possible coupling between the feedback coil and the input circuit.

The magnetic field resolution for $L_i = L_p$ can then be written as

$$B_N^{(p)} = \frac{(S_\Phi^p)^{1/2}}{\pi r_p^2} = \frac{2\sqrt{2}L_p^{1/2}\epsilon^{1/2}}{\pi r_p^2\alpha} \quad (2.6)$$

where r_p is the radius of the pick-up loop. Now [8], $L_p = \mu_0 r_p [\ln(8r_p/r_0) - 2]$, where $\mu_0 = 4\pi \times 10^{-7}$ henries/meter and r_0 is the radius of the wire. For a reasonable range of values of r_p/r_0 we can obtain $B_N^{(p)} = 2(\mu_0\epsilon)^{1/2}/\alpha r_p^{3/2}$. Thus one can improve the resolution indefinitely by increasing r_p , keeping $L_i = L_p$. However, in practice, the size of the cryostat sets the upper limit for r_p . For a conservative values of ϵ , α and r_p one gets $B_N^{(p)} = 5 \times 10^{-15} \text{ Tesla Hz}^{-1/2}$ which is much higher than any non superconducting magnetometer.

SQUID magnetometers usually employ flux transformers made of Nb wire. An important variation of the flux transformer is a gradiometer which can either be of first order measuring $\delta B_z/\delta z$ or a second order measuring $\delta^2 B_z/\delta z^2$. The gradiometer discriminates strongly against distant noise sources which have a small gradient, in favour of locally generated signals. One can thus use a second order gradiometer in an unshielded environment. Our magnetization measurements were recorded on the SQUID magnetometer : the Magnetic Properties Measurements System (MPMS) from Quantum Design Inc. at Tata Institute of Fundamental Research, Mumbai. Figure 2.3 shows a general wiring diagram of this SQUID magnetometer. This uses a second order gradiometer.

The coils are wound in a second-derivative configuration in which the upper and lower

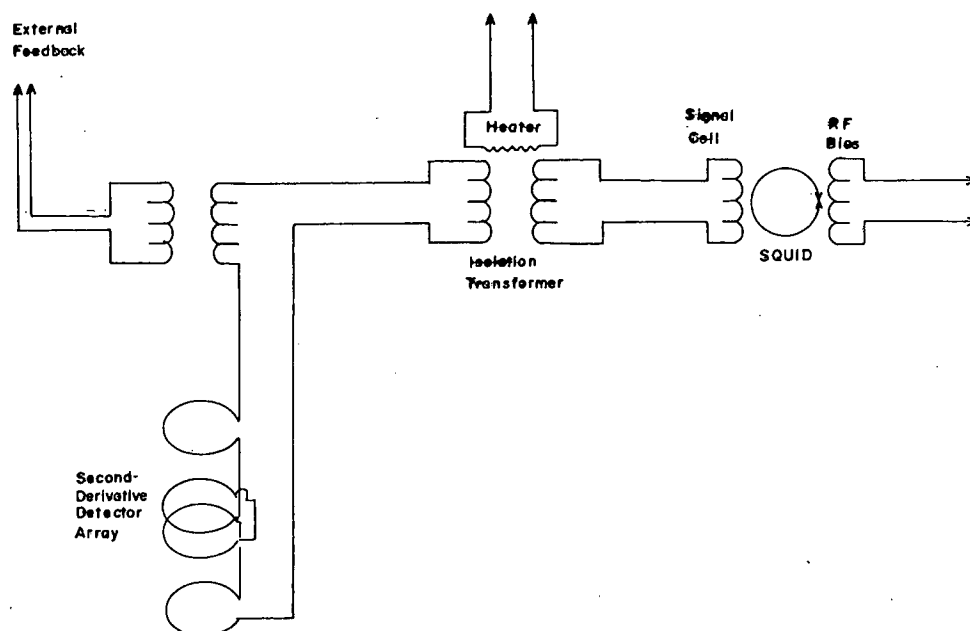


Figure 2.3: General wiring diagram of the SQUID Magnetometer from Quantum Inc.

single turns are counterwound with respect to the two-turn center coil. As mentioned above, this configuration strongly rejects interference from nearby magnetic sources and lets the system function without the need for a superconducting shield around the SQUID sensing loop. The general diagram of the coils is shown in Figure.2.4

The normal measurement process used in the MPMS is to position the sample below the detection coils with the sample transport set at its lower limit of travel, and then raise the sample through the coils while measuring the output of the SQUID detector.

In its initial position, the sample should be well below the detection coils so that the SQUID does not detect the sample moment. The sample is then typically measured by repeatedly moving the sample upward some distance and reading the voltage from the SQUID detector. If the SQUID voltage is read at large number of points, the voltage can be plotted as a function of sample position, as shown in Figure.2.5. A set of such data is known as scan.

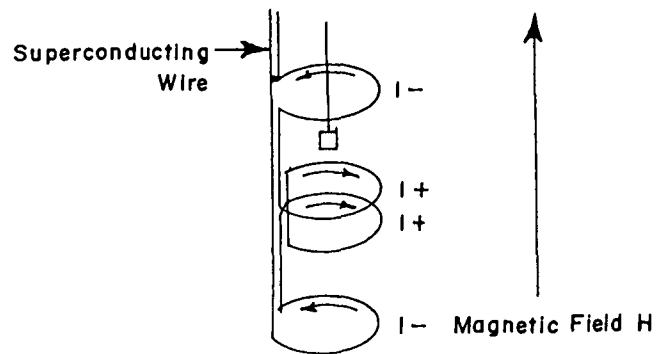


Figure 2.4: Diagram of the second order Gradiometer coils

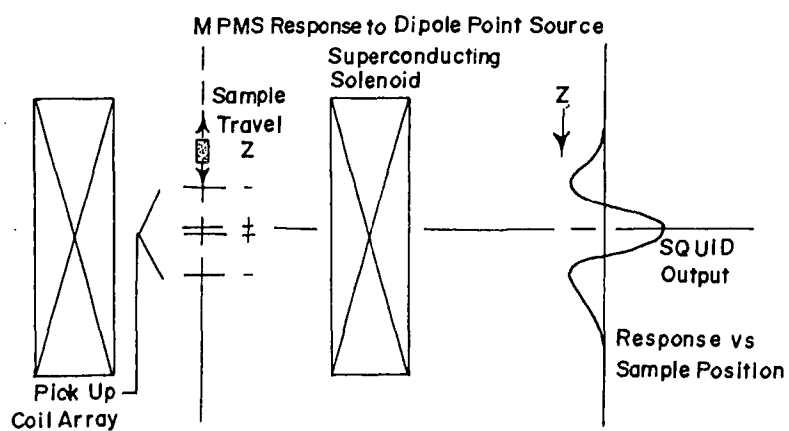


Figure 2.5: A typical 'scan' of the SQUID Magnetometer

Data Measurement and Analysis

The raw data from a measurement are a set of voltage readings taken as a function of position as the sample is moved upward through the sensing loops. At each position, the SQUID output voltage is typically read several times, and many vertical scans can be averaged together to improve the measurement resolution. The magnetic moment calibration for the system is determined by measuring palladium standard over a range of magnetic fields, and adjusting the system calibration factors to obtain the correct moment of the standard. The standard is a right circular cylinder approximately 3mm diameter \times 3mm high. With pickup coil geometry used in MPMS, samples of this size or smaller are effectively point sources to an accuracy of about 0.1%.

After the raw data have been collected, one of the three methods is used to compute the magnetic moment of the sample. Using the full scan method the moment is calculated as the square root of the sum of the squares, normalized for the number of data points and the system calibration factors. This process minimizes errors due to volume variations of the sample. This analysis works well when the signal is large compared to the noise of the system. However, when the sample response becomes comparable to the system noise, this technique effectively sums the noise signal as well as the signal, rather than trying to average the noise to zero.

The other two methods available for moment calculation are Linear Regression and Iterative Regression. These methods calculate the EMU value by fitting a theoretical signal to the measured data and using the best fit to calculate the EMU. The regression calculations eliminate noise more effectively, and the iterative calculation corrects the sample position by adjusting for vertical displacement before calculating the EMU.

Sample Mounting Considerations

The sample holder can be a major contributor to the background signal, but this contribution can be minimized by choosing materials with low magnetic susceptibility and by keeping the mass of these materials to a minimum. The materials used in the sample holder must also perform well over the temperature range to be used. In a gradiometer-type magnetometer, like the one used here, the geometrical arrangement of the background and the sample is critical when their magnetic susceptibilities will be of similar magnitude, and thus the sample holder should optimize the positioning of the sample in the magnetometer. The sample should also be rigidly mounted to avoid extraneous motion of the sample during measurements.

In case of a second order gradiometer, moving a long homogeneous sample (which extends well beyond the ends of the coil during measurement) through the pickup coil will not produce any signal. For this reason the drinking straw, which is light weight, homogeneous plastic tube, is often used as an important part of the sample holder. Since a homogeneous sample that extends well beyond the pickup coils does not produce a signal, yet a small sample does produce a signal, there must be a cross over between the two limits. The sample length should not exceed 10mm along the field direction to obtain most accurate measurement. It is important to keep the sample susceptibility constant over its length as well the sample should be kept close to the centerline of the magnetometer to get the most accurate measurements.

When the background contribution of the sample holder will be similar in magnitude to the sample signal, the relative position of the sample and the materials producing the background is important. If there is a spatial offset between the sample and the

background along the axis of the magnet, the signal produced by both of them will be highly distorted and will not be characteristic of the dipole moment that is being measured.

In our measurements, samples in the form of rectangular pieces, typically of 5mm height by 3mm breadth were used. Magnetization (M) was measured as a function of temperature and as a function of field. $M(T)$ was measured in an applied field of 50 Oe and 1000 Oe in the temperature range of 5 to 300 K. The sample was initially cooled from 300K to 5 K in zero applied field and the data was recorded while warming up to 300 K in the applied magnetic field (referred to as ZFC curve) and subsequent cooling (referred to as FC curve) back to 5 K. It may be emphasized here that care has been taken to make sure that the remanent field of SQUID magnetometer was less than ± 13 Oe during the low field measurements. Magnetization as a function of field was measured under sweep magnetic fields up to $\pm 5T$ at various temperatures. Before each $M(H)$ was recorded, the sample was cooled in zero field from 300 K to the desired temperature of measurement. Magnetization was measured while increasing H to 50 kOe (virgin curve). Measurement of M was then continued with the cycling of H between 50 and -50 kOe.

2.4.2 Four Probe Resistivity

In the investigation of the electrical properties, a method for measuring the resistivity of the material is of great importance. The simplest way to measure the resistance of the material is to make two contacts and measure the drop of voltage while letting the current pass through the contacts. Temperature dependant electrical resistivity measurements on all the samples were made using the in-house conventional d.c four probe setup. This resistivity inset has a sample holder with four equidistant copper contacts. The sample

is mounted onto this holder using G-varnish that electrically isolates the sample from the rest of the insert while maintaining a good thermal contact. A manganin heater radially wound just above the sample holder serves to control the temperature of the sample. Here the desired current through the sample is passed through the outer two contacts using a Keithley 224 programmable constant current source and the potential developed across the inner two contacts made on the sample is measured using a Keithley 2182A nanovoltmeter. The entire system is evacuated and cooled in a liquid Nitrogen dewar and the temperature is measured with a calibrated Platinum resistor (Pt-100) having an accuracy of 0.1K using Keithley 2010 multimeter. Using this set-up measurements in the temperature range of 77K to 350K can be made.

Rectangular bars with dimensions $\approx (2\text{mm} \times 5\text{mm} \times 1\text{mm})$ were cut from the sample and used for the measurements. The data acquisition was carried in the cooling and warming cycles in the temperature range: 77K to 300K.

2.5 X-ray Photoelectron Spectroscopy

Electrons in condensed matter are classified into core electrons and outer electrons (or valence electrons). The core electrons are well localized inside the atom, and so they keep their properties in the free atom state, irrespective of the chemical surroundings. On the other hand, the outer electrons are more extended and contribute to the inter-atomic bond, so that their properties are different for different materials even with the same atomic origin. In the core level spectroscopy, a core electron is excited by an incident photon or by an incident electron, and the spectra associated with the core level excitation, provide us with important information on the properties of outer electrons, as

well as atomic arrangements. One of the most important aspects of core level spectroscopy is that many body effects of outer electrons are often reflected sensitively in the spectral features. In magnetic materials which contain incompletely filled f or d electrons, the core holes couple strongly with f or d electrons resulting in splitting of core level spectra. One of the origins of the splitting is known as the exchange splitting, where the core hole spin s is coupled with the local spin S of f or d electrons on the core hole site through the exchange interaction given by $U = -J.S.s$. When the core hole has a finite value of orbital angular momentum, the exchange splitting is generalized to the multiplet splitting. The exchange or multiplet splitting is essentially of atomic origin [9]. When monochromatic source of x-rays are used to remove core electrons, the photoelectron spectroscopy is referred to as X-ray Photoelectron Spectroscopy (XPS). If an electron is ionized from a core level with non zero orbital angular momentum, the spin of the whole state can couple to its orbital angular momentum leading to two different J values, ($J = 1 \pm 1/2$) i.e. $J_1 = 3/2$ and $J_2 = 1/2$ for the final state. As the energy of these two final states are different, the spectrum of any such core level shows a doublet structure corresponding to the different J values in absence of any other interaction. The 2p levels of the first row transition metal oxides, the 3p and 3d levels of second row transition metal oxides are known to show such spin-orbit coupled doublet structure in XPS spectra. The energy difference ΔE_{nl} , between the two peaks corresponding to the two different J values is known as the spin orbit splitting. Besides the doublet structure corresponding to different J values, XPS spectra of transition metal compounds (3d, 4d), rare earths (4f,5f) where electron correlation are strong, show evidence of satellites next to the core level peaks [10, 11, 12] due to multielectronic excitations. These satellites can appear on the higher

(shake up) or on the lower energy side (shake down) of the main core level peaks. When a core-hole is created in one of the levels, the nuclear charge felt by the other electrons increases nearly by +1 and the outer electrons relax in this new attractive potential. The relaxation energy thus produced can cause an outer electron to make a transition to an unoccupied state. If such a transition takes place, the energy of the photoejected electron decreases or increases by an amount equal to the energy of the transition and an extra peak appears in the photoelectron spectrum. Energy separation and intensity of the satellite with reference to the main peak for a given metal ion depend on the nature of the ligand, and gives the energy difference between bonding and antibonding levels.

X-ray photoelectron spectra at Co (2p) and Ru (3d) levels were recorded using Thermo Fisher Scientific Multilab 2000 (England) instrument with Al K_{α} radiation (1486.6 eV). The binding energies reported here is with reference to graphite at 284.5 eV having an accuracy of ± 0.1 eV.

2.6 X-ray Absorption Fine Structure Spectroscopy

X-ray Absorption Fine Structure commonly known as XAFS is a technique employed to study the chemical environment of the atoms in a crystal. When a high energy X-ray photon is absorbed, a core level electron is emitted if the incident energy of the photons exceeds its binding energy. This causes a sharp dip in the transmitted intensity which is called as "absorption edge". The outgoing photo-electron can be thought of as a spherical wave expanding in all directions. When such a wave reaches the neighboring atoms, it will be partially back-scattered. The back-scattered wave interferes with the outgoing electron wave causing a constructive or destructive interference. The net effect is the

modulation of the transmitted X-rays through the absorber upto about 1000 eV from the absorption edge. The interference pattern depends mainly on the number, nature and distance of the surrounding atoms. Thus XAFS proves to be a useful tool for the study of the atoms in a solid. The XAFS experiment can be divided into three parts, the experimental set-up, the sample preparation and the data analysis procedure. The first two parts will be discussed below while the actual procedure for data analysis is discussed with LaSrCoRuO₆ XAFS as an example and presented in the next Chapter.

2.6.1 Experimental Setup

The X-ray absorption experiment can be carried out in the transmission as well as fluorescence mode. All the experiments presented in this thesis were carried out using the Co and Ru edge in transmission mode at room temperature using the beamline 12C at the Photon factory, Tsukuba, Japan. The X-ray source here is the bending magnet type with 1.2 T field and the energy ranges from 2 - 2.4 GeV with injection current of 300 mA (@ 2 GeV) and 130 mA (@2.4 GeV). The Fig.2.6 shows the schematic of a typical XAFS experiment for both, transmission and fluorescence geometries. The main components are: the monochromator used to select the X-ray energy, the slits and the ion chambers used to sample the incident and transmitted X-ray intensities. Polychromatic X-rays are produced by the synchrotron radiation source or by bremsstrahlung from a conventional laboratory source and a desired energy band of approximately 1 eV bandwidth is then selected by diffraction from monochromator. The monochromator consists of two channel-cut silicon crystals held parallel to each other. Only those X-ray photons that are of correct wavelength λ ($\lambda = hc/E$, where h is the Planck's constant and c is the speed of light) to satisfy the Bragg condition $n\lambda = 2d\sin\theta$ at the selected angle θ will be

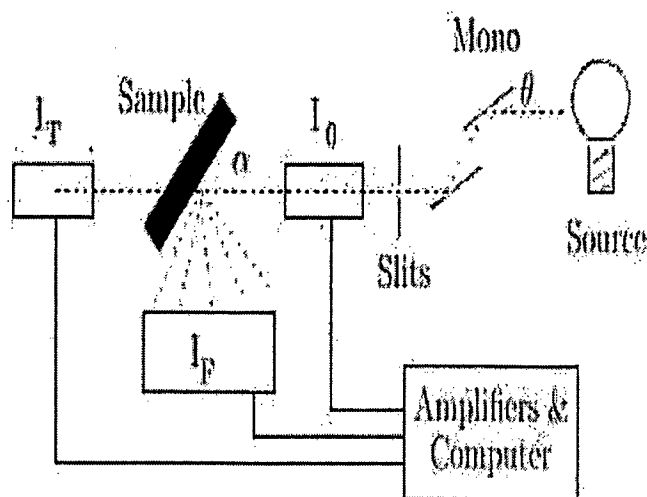


Figure 2.6: Schematic of the XAFS experiment. The setup for both the transmission and fluorescence geometries is depicted

reflected from the first crystal. The parallel second crystal is used as a mirror to restore the beam to its original direction. However, along with the fundamental edge energy E , the monochromator crystals can pass higher order harmonics (like $2E$, $3E$, etc) into the experimental beam. Making the two crystals slightly non-parallel by detuning the second crystal eliminates the higher order harmonics that would interfere with the fundamental reflections. The harmonics rejection is further achieved by using X-ray mirrors made of metals with high atomic number viz. Rh or Pt.

The slits placed after the monochromator define the size of the beam that strikes the sample. The dimensions of the slits are so chosen as to strike a balance between two contrasting aspects: maximizing the throughput and maximizing the energy resolu-

tion. The throughput is increased by opening the slits as more photons pass through. However, due to the angular divergence of the X-ray source and the geometry of the monochromator, there is a spread of energies compromising the energy resolution. The slit window at EXAFS beamline at Photon factory, Tsukuba, Japan has a rectangular geometry and all four sides can be adjusted to attain a critical size of the beam incident on the sample. The incident and transmitted X-ray fluxes are monitored usually with gas ionization chambers. The ion chambers are basically, parallel plate capacitors with high voltage maintained across the plates. The region in between the plates is filled with gas that gets ionized when x-rays travel through it. The associated electronics measures the current produced and hence determines the proportional x-ray intensity. The choice of a particular gas or mixture of gases that fills the ion chambers is made on the basis of the x-ray edge to be measured. Finally, the sample is affixed onto a motorized sample stage with monochromatic movement to facilitate the movement of the sample into the beam. For the XAFS measurement at ambient conditions, sample is in direct contact with the surroundings. XAFS can also be carried out in wide range of sample environment conditions with suitable modifications at the sample holder stage.

2.6.2 Sample Preparation

The form of the sample for XAFS experiment is just as important as the technique of measurement and needs to be prepared in much the same way with due consideration to absorption of X-ray photons. The most important characteristics of an XAFS sample are its thickness, homogeneity and purity. The sample thickness is determined by optimizing the signal to noise ratio. This corresponds to an edge step absorption coefficient of about 1.0 while total absorption coefficient does not exceed 2.5. The homogeneity of the sample

is important because the XAFS signal gets attenuated if part of the x-rays do not pass through the sample. The particle size of the powder sample should be fairly uniform.

Taking into consideration all these factors, absorbers for the XAFS experiments were made by spreading very fine powder of the sample on a scotch tape avoiding any sort of sample inhomogeneity and pin holes. Small strips of the sample coated tape were cut and were held one on top of the other. This assembly of the sample coated tape was sandwiched in between the scotch tape and held onto the sample holder plate. Enough number of such strips were adjusted to give absorption edge jump, $\Delta\mu x \leq 1$. XAFS at Ru and Co K-edges were recorded in the transmission mode using Si(111) as monochromator. The K-edge energies of Ru and Co are given in the table.

The measurements were carried out at room temperature and liquid Nitrogen temperature. The incident and transmitted photon intensities were simultaneously recorded using gas-ionization chambers filled with mixtures of He-N₂ for Ru edge and Ar-N₂ for Co edge. Measurements were carried out from 300 eV below the edge energy to 1000 eV above it with a 5 eV step in the pre-edge region and 2.5 eV step in the EXAFS region. At each edge, three scans were collected for each sample.

Data analysis was carried out using IFEFFIT [13] in ATHENA and ARTEMIS programs [14]. Here theoretical fitting standards were computed with ATOMS and FEFF6 programs [15, 16].

References

- [1] B.D. Cullity, Elements of X-ray Diffraction, Addison Wesley Publishing Co. USA (1956)
- [2] A.J. Dekker, Solid State Physics, Prentice Hall Edition (1957)
- [3] F. London "Superfluids" Wiley, New York, 1950
- [4] B.D. Josephson, Phys. Lett. **1**, 251 (1962); Adv. Phys., **14**, 419 (1965)
- [5] R.C. Jaklevic, J. Lambe, A.H. Silver and J.E. Marcereau, Phys. Rev. Lett., **12**, 159 (1964)
- [6] J.E. Zimmermann, P. Thiene and J.T. Harding, J. Appl. Phys., **41**, 1572 (1970)
- [7] J.E. Mercereau, Rev. Phys. Appl. **5**, 13 (1970) and N. Nisenoff, Rev. Phys. Appl., **5**, 21 (1970)
- [8] D. Shoerberg, "Superconductivity" p.30, Cambridge Univ. Press, 1962
- [9] J. Kanomori and A. Kotani, in "Core Level Spectroscopy in Condensed Systems", Proceedings of the Tenth Taniguchi International Symposium, Japan (Springer Verlag) Berlin, Heidelberg (1998).
- [10] C.K. Jorgensen and H. Berthou, Chem. Phys. Lett., **13**, 186 (1972)

- [11] T.A. Carlson, J.C. Carver and G.A. Vernon, *J. Chem. Phys.*, **62**, 932 (1975)
- [12] G.A. Vernon, G. Stucky and T.A. Carlson, *Inorg. Chem.*, **15**, 278 (1976)
- [13] M. Newville, *J. Synchrotron Rad.*, **8**, 322, (2001)
- [14] B. Ravel and M. Newville, *J. Synchrotron Rad.*, **12**, 537 (2005)
- [15] B. Ravel, *J. Synchrotron Rad.*, **8**, 314 (2001)
- [16] S.I. Zabinsky, J.J. Rehr, A. Ankudinov, R.C. Albers and M.J. Eller, *Phys. Rev. B*, **52**(4), 2995 (1995)

Chapter 3

Disorder Induced Negative Magnetization in LaSrCoRuO_6

3.1 Introduction

Ordering of B-site cations in the double perovskites is known to play an important role in deciding the magnetic, transport and structural properties of these systems. $\text{Sr}_2\text{FeMoO}_6$ and $\text{Sr}_2\text{FeReO}_6$ both of which display large low field magnetoresistance are two good examples [1, 2]. The itinerancy and ferrimagnetism in the above materials arise from a double exchange type of mechanism in which the ordering and electronic configurations play a critical role [3]. The characteristics of this type of ordering stems from the fact that it combines features of both ferromagnetic (FM) and antiferromagnetic (AF) systems. Moreover, if more than two spin sub-lattices are involved, a new phenomena like temperature induced magnetization reversal can emerge [4]. So far, apart from ferrimagnets [5], only few other families of oxides which include layered ruthenates, vanadates and manganites have exhibited temperature induced magnetization reversal [4, 6, 7, 8, 9, 10, 11, 12].

The above compounds, often characterized by a strong competition between antiferromagnetic and ferromagnetic coupling and a complex interplay of spin, charge, and orbital degrees of freedom, are extremely sensitive to small perturbations such as slight

structural alterations. Sr_2YRuO_6 is a typical example. Here the negative magnetization observed in low fields has been ascribed to two oppositely ordered ferromagnetic superexchange interactions viz, Ru-O-O-Ru and Ru-O-Y-O-Ru [10]. LaSrCoRuO_6 is another compound wherein degree of B-site (Co and Ru) order can lead to intriguing magnetic and transport properties [13, 14]. However, here unlike Y, Co is a magnetic ion and that has led to different interpretations of the nature of magnetic order in this compound. LaSrCoRuO_6 was reported to be a 3D variable range hopping semiconductor with magnetic ordering temperature of 157K [15]. Recent studies suggest that the compound is an antiferromagnet with $T_N = 87\text{K}$ [13] or a spin glass [14] and the transition at 157K could be due to SrRuO_3 impurity. Apart from SrRuO_3 impurity phase, the sharp rise in magnetization can also be due to ferromagnetic Ru-O-Ru interactions arising from antiphase grain boundaries [16]. The studies conducted on LaSrCoRuO_6 so far by varying the composition ratio of A site ions (La and Sr) highlight the importance of different magnetic interactions between $\text{Co}^{2+/3+}$ and $\text{Ru}^{4+/5+}$ in governing the magnetic ground state [14, 17]. This chapter reports the effect of thermally induced site-occupancy disorder in LaSrCoRuO_6 on its magnetic properties. The most notable feature that we see here is the observation of negative magnetization at low applied fields in the more disordered sample. The results have been explained on the basis of EXAFS data recorded at Co and Ru K-edge to be due to presence of additional ferromagnetic interactions resulting from B-site disorder in an otherwise antiferromagnetic lattice.

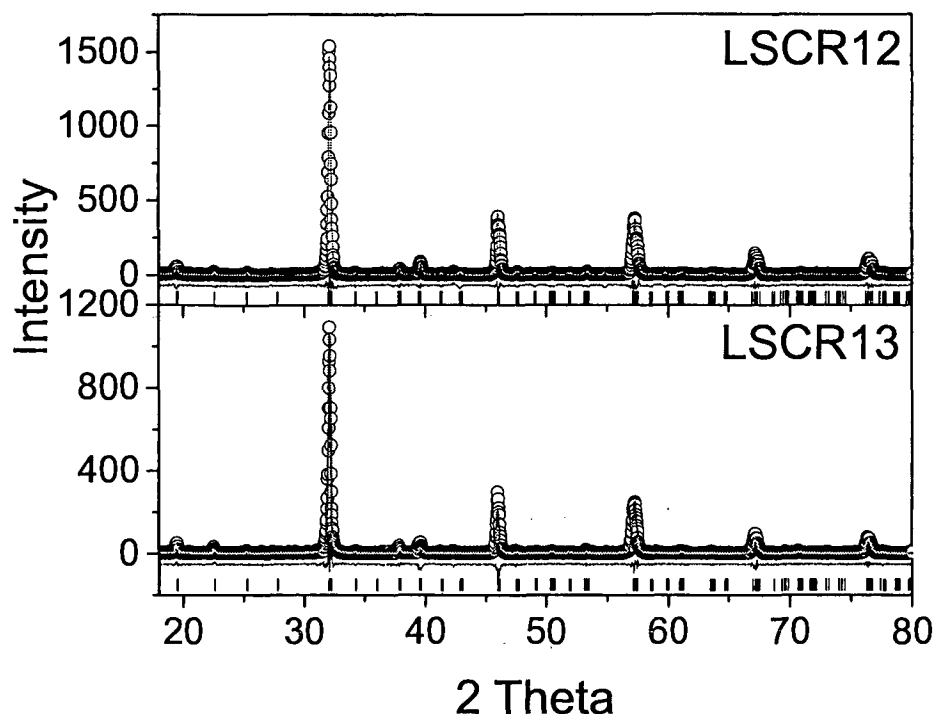


Figure 3.1: Rietveld refined XRD patterns for LSCR13 and LSCR12. The open circles show the observed counts and the continuous line passing through these counts is the calculated profile. The difference between the observed and calculated patterns is shown as a continuous line at the bottom of the two profiles. The calculated positions of the reflections are shown as vertical bars.

3.2 Structural Studies(X-ray and Neutron Powder Diffraction)

The Rietveld refined XRD patterns for two samples of LaSrCoRuO_6 viz, LSCR13 and LSCR12 prepared at 1300°C and 1200°C respectively are presented in Fig. 3.1.

The stoichiometric double perovskite, LaSrCoRuO_6 has a monoclinic structure with the B-site cations Co and Ru ordered in the NaCl pattern in the space group $P2_1/n$. ND patterns recorded at 300K (Fig. 4.5) show evidence for higher degree of B-site order in LSCR13 as compared to LSCR12. The presence of the sharper $(\frac{1}{2}, \frac{1}{2}, \frac{1}{2})$ super lattice reflection in the ND pattern in LSCR13 (see inset Fig 4.5) indicates a higher degree of

Table 3.1: Unit cell parameters, Co and Ru site occupancies obtained from Rietveld refinement and Curie-Weiss parameters calculated from magnetization measurements at 1000 Oe for the two samples of $\text{LaSrCo}_{1-x}\text{Ru}_{1+x}\text{O}_6$. Numbers in parentheses are uncertainty in the last digit.

Sample	LSCR13	LSCR12
a (Å)	5.5847(4)	5.5891(3)
b (Å)	5.5592(6)	5.5540(5)
c (Å)	7.8674(9)	7.8787(5)
β	90.05(2)	90.10(1)
Volume (Å ³)	244.25(4)	244.57(3)
Co ($\frac{1}{2}, 0, \frac{1}{2}$)	0.98(1)	0.87(1)
Ru ($\frac{1}{2}, 0, \frac{1}{2}$)	0.02(1)	0.13(1)
Ru ($\frac{1}{2}, 0, 0$)	0.98(1)	0.87(1)
Co ($\frac{1}{2}, 0, 0$)	0.02(1)	0.13(1)
μ_{eff} (μ_B/fu)	5.47(2)	5.43(1)
Θ_{CW} (K)	-49(2)	-2.5(4)

ordering in LSCR13.

Rietveld refinement of the XRD and ND patterns was carried out with $P2_1/n$ space group wherein the La/Sr occupy the 4e site with fractional coordinates (0.0033, 0.0218, 0.25), Co is at 2c (0.5, 0, 0.5), Ru is at 2d (0.5, 0, 0) and the oxygen atoms occupy three sites, viz, (0.2886, 0.280, 0.0355); (0.2324, 0.774, 0.0264) and (-0.0662, 0.4938, 0.255) [1]. The scale factor, background parameters, cell parameters, Co and Ru site occupancies along with instrumental broadening, totalling to 17 parameters were refined in that order to obtain a good fit. The crystallographic parameters obtained from refinement of ND patterns along with Curie-Weiss parameters calculated from magnetization measurements are summarized in Table 6.1. Refinement shows that there is only about 4% disorder in the case of LSCR13 whereas in case of LSCR12 about 20% of Co occupies the Ru site (2d site) and vice versa thereby resulting in a larger disorder in the occupation of the B-sites as compared to LSCR13. Therefore, we refer to LSCR13 as a ordered compound while LSCR12 is referred to as disordered compound.

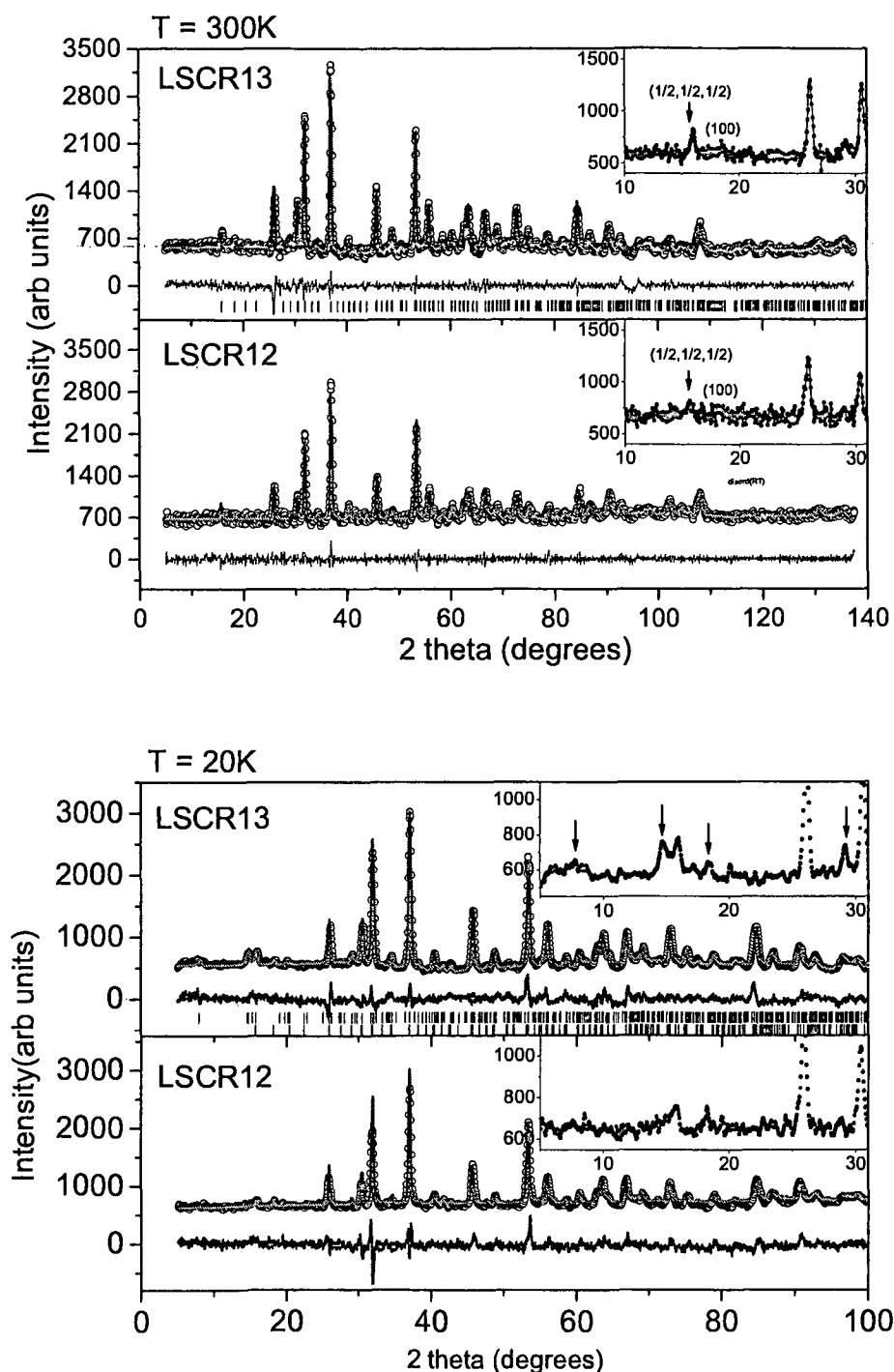


Figure 3.2: Observed (circles), calculated (line) and difference ND patterns recorded at 300K (upper panel) for LSCR13 and LSCR12. The inset presents data in limited range with the superlattice reflections seen clearly in LSCR13 indicating higher degree of order. The lower panel shows neutron data taken at 20K for the same samples. The inset presents data in limited range with the arrows indicating magnetic reflections present in LSCR13.

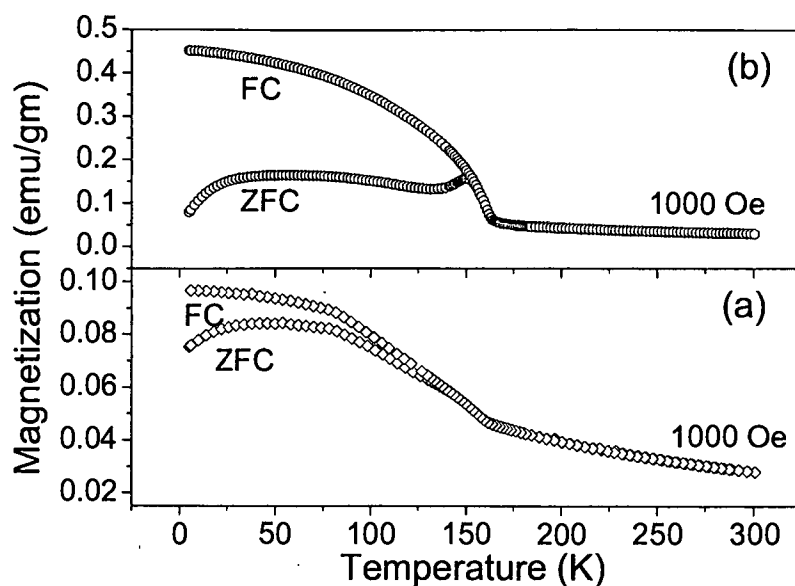


Figure 3.3: Magnetization as a function of temperature at applied fields of 1000 Oe in LSCR13 (a) and LSCR12 (b).

3.3 Magnetization Measurements

Magnetization measurements performed at 1000 Oe during the ZFC and FC cycles for the two LaSrCoRuO_6 samples are presented in Fig. 6.4.

In case of LSCR13, both ZFC and FC cycles rise sharply below 160K and branch off below 130K. While the ZFC curve culminates into a broad hump centered at about 55K, the FC curve approaches a constant value below 77K. These curves do not reveal the nature of magnetic order in the compound. It may be noted here that spin frozen ground state has been previously reported for this composition [14]. In yet another study, antiferromagnetic order has also been reported with $T_N = 87\text{K}$ [13]. In order to confirm the nature of magnetic order in the present sample, ND pattern was recorded at 20K and is presented in Fig. 4.5. Weak extra reflections due to antiferromagnetic ordering are seen at the positions described by propagation vector along the $k = \frac{1}{2} 0 \frac{1}{2}$

with respect to the crystallographic $P2_1/n$ cell. This magnetic arrangement is the same as that reported by Bos and Attfield [13].

In the case of LSCR12, there is a wide difference in magnetization behaviour recorded during ZFC and FC cycles. The ZFC magnetization with increasing temperature increases sharply culminating into a broad hump centered around 50K. It decreases slightly with further rise in temperature before increasing sharply resulting in a peak at 151K. The FC magnetization, on the other hand decreases continuously to 167K and settles into a low value giving an impression of ferro to para transition. The differences in behaviour of magnetization during ZFC and FC cycle indicate a complex magnetic ground state. ND pattern recorded at 20K as seen in Fig. 4.5 also does not show any evidence of long range magnetic order within our detectable limit. This could be implied to a magnetically frustrated ground state due to presence of competing ferro and antiferromagnetic interactions.

Plot of inverse of susceptibility ($1/\chi = H/M$) in Fig. 3.4. For LSCR13 $1/\chi$ varies linearly with temperature in the range $170K < T < 300K$ and Curie-Weiss fit to the data yields effective paramagnetic moment $\mu_{eff} = 5.47 \mu_B/f.u.$ in good agreement with the calculated spin only moment of Co^{2+} and Ru^{5+} ions and the Curie-Weiss temperature, $\Theta_{CW} = -49K$ that is also in good agreement with the value reported earlier [14]. The negative Θ_{CW} indicates the presence of strong antiferromagnetic interactions.

In the case of LSCR12, the susceptibility although seems to be fairly linear down to 170K, deviates below the Curie-Weiss behaviour at temperatures less than 220K. A linear fit in the temperature region 300K to 240K, to inverse susceptibility of LSCR12 with Curie-Weiss equation results in $\mu_{eff} = 5.43\mu_B/f.u.$ and $\Theta_{CW} = -2.5K$ (see Fig. 3.4).

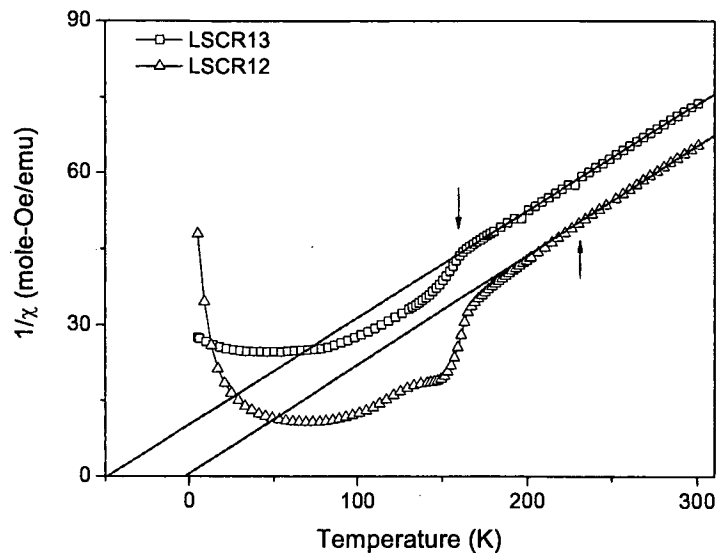


Figure 3.4: Inverse Magnetic susceptibility function of temperature calculated as $\chi = M/H$ at applied fields of 1000 Oe in LSCR13 and LSCR12.

The reduced value of Θ_{CW} and the deviation from Curie-Weiss behaviour from higher temperature in LSCR12 points to presence of short range ferromagnetic interactions in this compound. The presence of ferromagnetic interactions can be due to the presence of small amount of SrRuO_3 impurity which has an ordering temperature in the region of 140K - 160K. Although this agrees well with the sharp rise in magnetization in LSCR12 below 170K, the deviation of susceptibility from Curie-Weiss behaviour from about 220K hints at the presence of short range ferromagnetic interactions arising due to some other reason than due to SrRuO_3 impurity alone. Further the absence of magnetic Bragg reflections in the neutron diffraction pattern of LSCR12 due to antiferromagnetic order as in case of LSCR13 emphasizes the presence of short range ferromagnetic interactions within LaSrCoRuO_6 lattice. The presence of small amounts of SrRuO_3 impurity would not alter the magnetic ground state of parent LaSrCoRuO_6 .

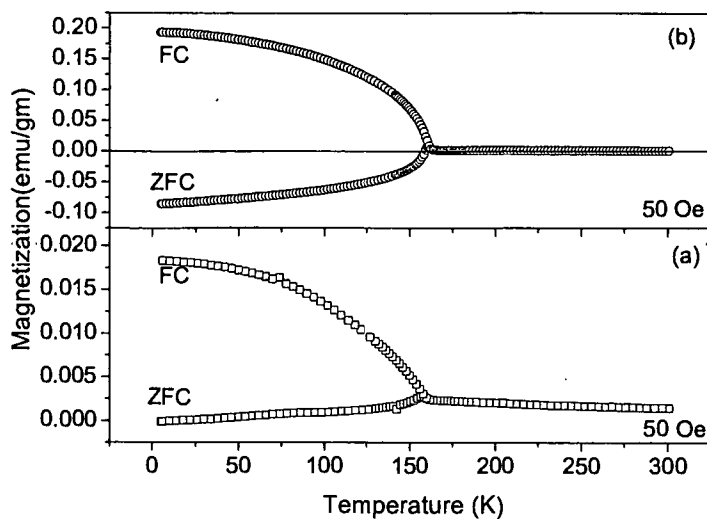


Figure 3.5: ZFC and FC magnetization curves at applied field of 50 Oe recorded for LSCR13 (a) and LSCR12 (b).

In order to understand magnetic properties better, the low field (50 Oe) magnetization data were measured during ZFC and FC cycles on the two samples of LaSrCoRuO_6 and are presented in Fig. 3.5. In case of LSCR12, magnetization measured during the ZFC cycle is negative at the lowest temperature. It decreases in magnitude with increasing temperature and crosses over to the positive side at 155 K, exhibits a peak at 160K signifying a transition from a magnetically ordered to paramagnetic state. During the FC cycle, magnetization behaviour is similar except its value is positive throughout. Such behaviour again cannot be understood to be due to presence of SrRuO_3 impurity alone. It may be emphasized here that care has been taken to make sure that the remanent field of SQUID magnetometer was less than ± 13 Oe during these low field measurements. In case of LSCR13, although the magnetization exhibits significant deviation between ZFC and FC cycles below 160K but is positive throughout.

Isothermal magnetic response of the two samples has been studied at various temper-

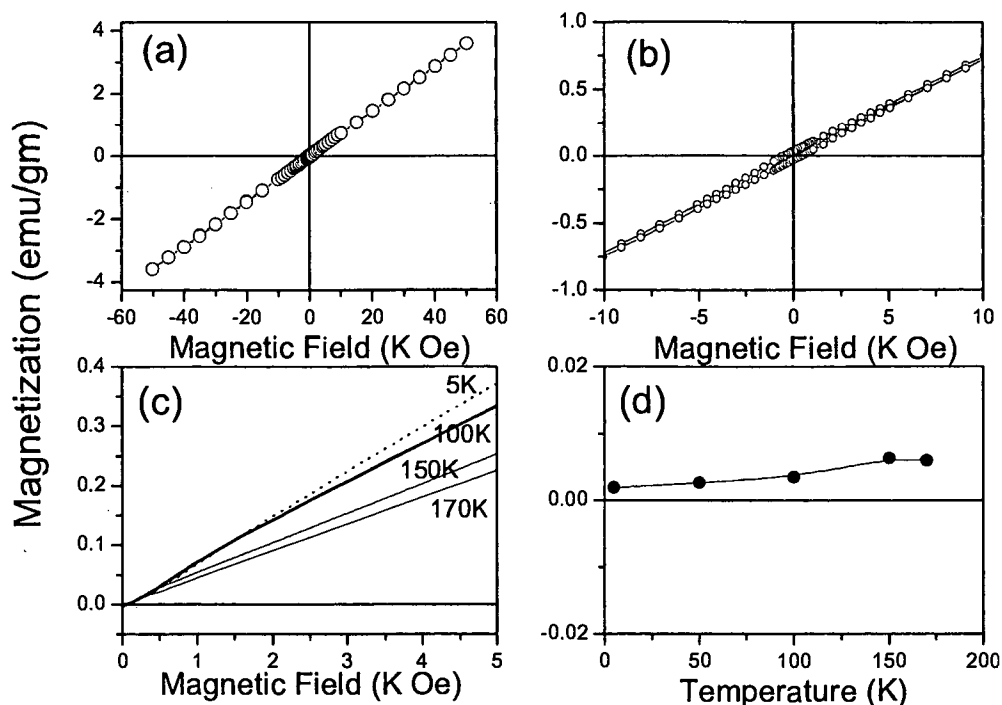


Figure 3.6: Isothermal magnetization curves for LSCR13 recorded in the field interval of $\pm 5\text{T}$ at 5K (a); its magnified view ($\pm 10\text{ KOe}$) (b); virgin magnetization curves at few representative temperatures (c) and variation of magnetization values extracted from virgin curves at a field value of $\sim 50\text{ Oe}$.

ature in the field range of $\pm 50\text{ KOe}$. Fig. 3.6(a) presents the isothermal magnetization curve for LSCR13 measured at 5K. The amplified loop ($\pm 10\text{ KOe}$) is presented in Fig. 3.6(b).

It can be seen that the magnetization exhibits strong field dependency and almost no hysteresis which is typical of an antiferromagnet. On the other hand for LSCR12 the isothermal magnetization studies performed at 5K (see Fig. 3.7(a)) exhibit a clear ferromagnetic hysteresis loop riding on an antiferromagnetic (linear) background. Such a hysteresis loop is typical for a compound with a ferromagnetic component along with antiferromagnetic interactions. The expanded loop in Fig. 3.7(b) shows that the ferromagnetic component is quite strong and about 4 to 5 times larger than that reported

in Ref. [13]. Calculation of saturation moment by extrapolating the linear regions of hysteresis loop yields a value of 0.64 emu/gm which is about 6% of the value of Ru in SrRuO₃. This cannot be ascribed to SrRuO₃ impurity alone as such a sizeable amount of SrRuO₃ would have been detected in diffraction studies. Therefore the observed magnetic behaviour can only be ascribed to presence of competing ferromagnetic and antiferromagnetic interactions resulting due to higher B-site disorder present in LSCR12. As the low field magnetization measured in ZFC cycle is negative, it is worthwhile to see the behaviour of virgin magnetization at different temperatures especially in the low field region. Fig. 3.7(c) exhibits the virgin magnetization curves for LSCR12 and Fig. 3.6(c) presents the same for LSCR13. While the magnetization remains positive even at very low fields for LSCR13, corresponding magnetization for LSCR12 is negative. Further the shape of virgin curve at 100K makes it amply clear that ferromagnetism is more dominant while the 5K curve is more linear corresponding to dominant antiferromagnetic interactions. This again excludes the possibility of ferromagnetism arising due to SrRuO₃ impurity alone. Further, in case of LSCR12, the value of magnetization at a low field (~ 50 Oe) extracted from virgin curves decreases below 150K and then shows a upturn towards positive values below 80K. This is more clearly depicted in Fig. 3.7(d). This clearly points to a presence of two magnetic sublattices which interact with each other leading to observed negative magnetization. No such dependence is observed in case of LSCR13 (see Fig. 3.6(d)).

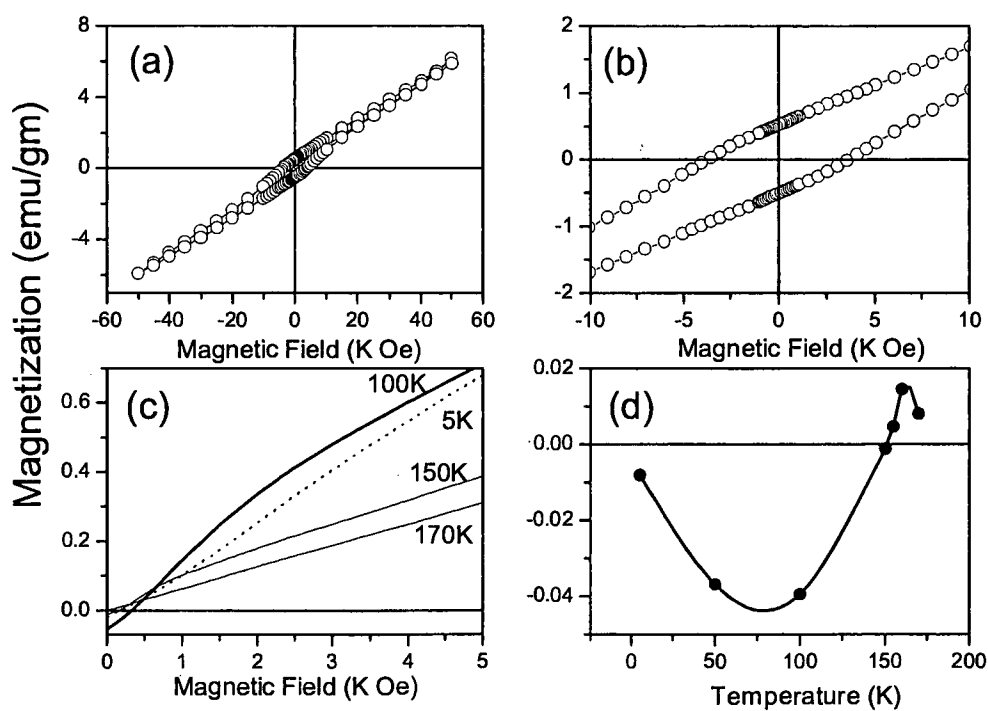


Figure 3.7: Isothermal magnetization curves for LSCR12 recorded in the field interval of ± 5 T at 5K (a); its magnified view (± 10 K Oe) (b); virgin magnetization curves at few representative temperatures (c) and variation of magnetization values extracted from virgin curves at a field value of ~ 50 Oe.

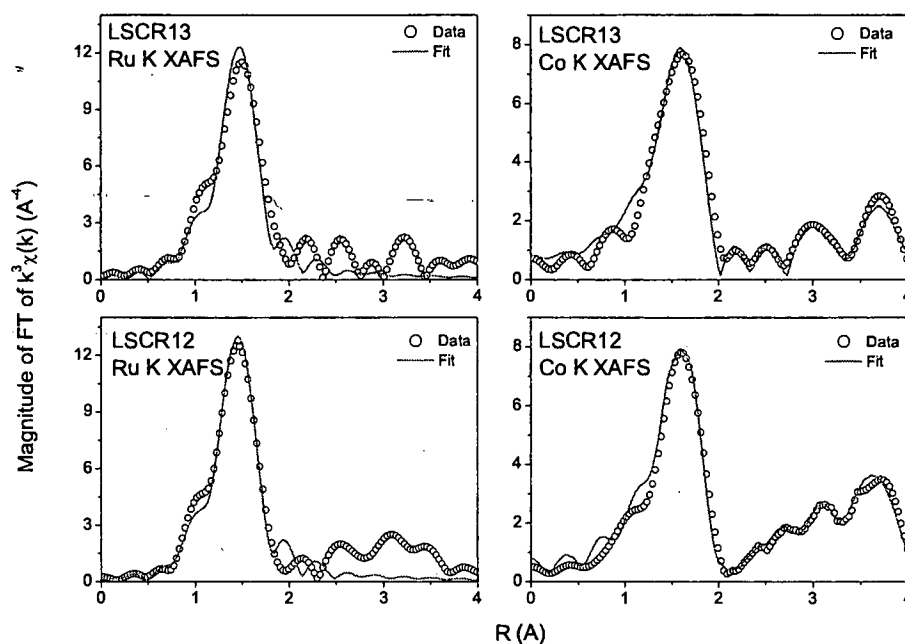


Figure 3.8: k^3 weighted magnitude of Fourier transform of EXAFS data recorded at Co and Ru K-edge in LSCR13 and LSCR12.

3.4 X-ray Absorption Fine Structure

A disorder in site occupancy of Co and Ru sites can strengthen ferromagnetic interactions. Such a disorder can result in Ru-O-Ru networks which will alter the Co and Ru octahedral networks, especially the Co-O-Ru bond angle. In order to investigate the changes in the local structures around Co and Ru in between the two samples, respective EXAFS data have been analyzed and the results are presented in Table 3.2 and Fig. 3.8.

It can be seen from the table that in case of LSCR12 the Co-O and Ru-O bond lengths are lower and the mean square radial displacements (σ^2) are higher as compared to those in LSCR13. Further, the values of Co-Ru single scattering bond length and Co-O-Ru multiple scattering bond length indicate that the Co-O-Ru bond angle increases in LSCR12 as compared to LSCR13. A straighter Co(Ru)-O-Ru(Co) bond angle implies a

Table 3.2: Structural parameters like bond length (RÅ), bond angle and mean square radial displacement ($\sigma^2\text{Å}^2$) obtained from Co and Ru K edge EXAFS analysis. Numbers in parentheses are uncertainty in the last digit.

Bond	LSCR13		LSCR12	
	R (Å)	σ^2 (Å ²)	R (Å)	σ^2 (Å ²)
Co-O	2.054(7)	0.008(1)	2.046(9)	0.009(1)
Ru-O	1.967(8)	0.003(1)	1.950(5)	0.004(1)
Co-Ru	3.97(6)	0.002(1)	3.97(1)	0.005(1)
Co-Ru-O-Co	4.00(7)	0.002(1)	4.00(1)	0.004(1)
\angle Co-O-Ru	161.7(1)°		166.4(1)°	

formation of quasi-itinerant π^* bands of Ru and/or ferromagnetic superexchange of high spin Co^{2+} -O-Ru⁵⁺ type. The higher value of σ^2 for Co-Ru bond distance is indicative of larger disorder in LSCR12. These local structural changes can be understood to be due to B-site occupancy disorder in LSCR12 resulting in formation of π^* bands due to Ru-O-Ru linkages. These itinerant-electron π^* bands interact ferromagnetically which explains the sudden increase in magnetization below 150K. The ferromagnetic Ru sublattice so formed is coupled by an antiferromagnetic exchange interaction to the Co-O-Ru antiferromagnetic sublattice. Below its ordering temperature ($\sim 150\text{K}$), the ferromagnetic Ru sublattice polarizes the paramagnetic Co moments in a direction opposite to the applied field leading to magnetic compensation and negative magnetization. Once the Co moments align antiferromagnetically below the antiferromagnetic ordering temperature of Co-O-Ru sublattice ($\sim 80\text{K}$) the magnetization increases towards a positive value as can be seen in Fig. 3.7(d).

3.5 Discussion

LaSrCoRuO₆ is AA'BB'O₆ type double perovskite crystallizing in a monoclinic structure. This structure allows for ordering of B-site cations in a NaCl fashion. This ordering is

favoured due to the charge difference ($\Delta q \geq 3$) between Co and Ru. In perfectly ordered LaSrCoRuO_6 , Co^{2+} and Ru^{5+} magnetic ions couple antiferromagnetically leading to an antiferromagnetic ground state as can be seen from neutron diffraction measurements. A disorder in Co and Ru site occupancy will result in Ru-O-Ru type linkages which are known to align ferromagnetically. The presence of ferromagnetic interactions is clearly visible in LSCR12 which has a larger B-site occupancy disorder in terms of increased values of magnetization as compared to those in LSCR13 and hysteresis in M vs H loop. Due to such a disorder in occupancy of Co and Ru sites, octahedral distortions set in, as the immediate neighbour of a Ru octahedra could be either a Ru octahedra or a Co octahedra. EXAFS results in LSCR12 bear a testimony to this fact. In LSCR12, the Co-O and Ru-O bond lengths are shorter, the mean square displacement is higher and Co-O-Ru bond is straighter. These changes are a result of Ru-O-Ru ferromagnetic linkages which due to their presence alter Ru-O-Co antiferromagnetic interactions. The negative magnetization seen in the low field ZFC magnetization is due to Ru-O-Ru ferromagnetic interactions which below $\sim 150\text{K}$ polarize the paramagnetic Co spins in a the direction opposite to applied field giving rise to magnetic compensation.

3.6 Conclusions

The disorder in occupation of Co and Ru sites in LaSrCoRuO_6 double perovskite results in Ru-O-Ru linkages which are ferromagnetic. Due to such linkages, the magnetization of disordered compound increases in magnitude as compared to that of ordered compound. At low applied fields the ferromagnetic spins polarize the paramagnetic Co spins in a direction opposite to the direction of magnetic field resulting in negative magnetization.

References

- [1] K. L. Kobayashi, T. Kimura, H. Sawada, K. Terakura and Y. Tokura, *Nature* (London), **395**, 677 (1998).
- [2] J. Gopalakrishnan, A. Chattopadhyay, S. B. Ogale, T. Venkatesan, R. L. Greene, A. J. Millis, K. Ramesha, B. Hannoyer and G. Marest, *Phys. Rev. B*, **62**, 9538 (2000).
- [3] D. D. Sarma, *Curr. Opin. Solid State Mater. Sci.*, **5**, 261 (2001).
- [4] A. A. Taskin and Y. Ando, *Phys. Rev. Lett.*, **98**, 207201 (2007).
- [5] K. P. Belov, *Phys. Usp.*, **39**, 623 (1996); **42**, 711 (1999); **43**, 407 (2000).
- [6] Y. Ren, T. T. M. Palstra, D. I. Khomskii, E. Pellegrin, A. A. Nugroho, A. A. Menovsky and G. Sawatzky, *Nature*, **396**, 441 (1998).
- [7] Y. Ren, T. T. M. Palstra, D. I. Khomskii, A. A. Nugroho, A. A. Menovsky and G. Sawatzky, *Phys. Rev. B*, **62**, 6577 (2000).
- [8] K. Yoshii, *J. Solid State Chem.*, **159**, 204 (2001).
- [9] K. Yoshii, A. Nakamura, A. Ishii and Y. Morii, *J. Solid State Chem.*, **162**, 84 (2001).

- [10] R. P. Singh and C. V. Tomy, *Phys. Rev. B*, **78**, 024432 (2008).
- [11] R. P. Singh and C. V. Tomy, *J. Phys.: Condens. Matter*, **20**, 235209 (2008).
- [12] G. Cao, Y. Xin, C. S. Alexander, and J. E. Crow, *Phys. Rev. B*, **63**, 184432 (2001).
- [13] J-W. G. Bos, J. P. Attfield, *Chem. Matter.*, **16**, 1822 (2004).
- [14] A. Mamchik, W. Dmowski, T. Egami, I-W. Chen, *Phys. Rev. B*, **70**, 104410 (2004).
- [15] S. H. Kim, P. D. Battle, *J. Sol. State Chem.*, **114**, 174 (1995).
- [16] S. Kim, R. I. Dass and J. B. Goodenough, *J. Sol. State Chem.*, **181**, 2989 (2008).
- [17] P. Tomeš, J. Hejtmánek and K. Knížek, *Sol. State Sci.*, **10**, 486 (2008).

Chapter 4

Structure, Transport and Magnetic Properties in



4.1 Introduction

LaSrCoRuO_6 is a double perovskite whose magnetic properties critically depend on cationic order, charge balance and complex magnetic interactions between two transition metal ions [1, 2, 3]. Its crystal structure is composed of corner-shared CoO_6 and RuO_6 octahedra arranged in a pseudocubic array in the rocksalt arrangement. It is a semiconductor with ideal valence states HS Co^{2+} ($3d^7$ high-spin configuration) and Ru^{5+} ($4d^3$) [4]. Magnetically these compounds are reported to be antiferromagnetic with two magnetic face centered cubic (fcc) sublattices consisting of Co and Ru. Both the sublattices order with type II antiferromagnetic structure which would mean that the spins in [111] planes in succession Co-Ru-Co-Ru alternate as $+/+/-/-$. This marginalizes the Co-O-Ru nearest neighbour interactions and the ordering is governed by a competition between linear Co-O-Ru-O-Co and 90° Co-O-O-Co antiferromagnetic exchange paths [1, 5]. The degree of ordering is known to affect the magnetic and transport properties due to changes in magnetic interactions and in cationic valence. Effects of anti-site disor-

der on the magnetic and transport properties due to La or Sr doping in LaSrCoRuO_6 have been investigated [1, 5, 6]. The change of composition (La or Sr doping) introduces mobile electrons in La richer samples or holes in Sr richer samples.

Another possible way of modifying magnetic and transport properties is by forming the solid solutions of antiferromagnetic LaCoO_3 and ferromagnetic SrRuO_3 . These perovskite solid solutions of the form $\text{Sr}_{1-x}\text{La}_x\text{Ru}_{1-x}\text{Co}_x\text{O}_3$ will have a strong interplay of cationic order, charge balance and complex magnetic interactions between the two B-site cations. In SrRuO_3 , the 4d electrons of the low spin Ru^{4+} ions occupy the narrow π^* band near Fermi level [7]. The lower 3d energy levels of Co^{3+} causes a charge transfer from 4d Ru^{4+} to 3d Co^{3+} [2]. However, Co can have various electronic states including high spin (HS) Co^{2+} , Co^{3+} and Co^{4+} , intermediate spin (IS) Co^{3+} and Co^{4+} and low spin (LS) Co^{3+} and Co^{4+} [8, 9, 10, 11, 12]. This complicates the situation giving rise to properties like localized magnetic moment of Co [13], negative magnetoresistance [14]. In case of $\text{Sr}_{1-x}\text{La}_x\text{Ru}_{1-x}\text{Co}_x\text{O}_3$, a complete charge transfer occurs at $x = 0.5$. At this composition, the CoO_6 and RuO_6 octahedra align themselves in a pseudocubic array in the rocksalt arrangement forming the arch-type "double perovskite" structure.

The charge transfer between Ru and Co in LaSrCoRuO_6 is very sensitive to local atomic structure such as cation order [1, 3, 6]. Any disturbance in this cation order leads to compensation of antiferromagnetic interactions by the ferromagnetic interactions most likely associated with Ru-O-Ru interactions. The LaCoO_3 substituted SrRuO_3 , has been known to exhibit large local magnetic moment arising due to Co spin polarizing the itinerant electrons of SrRuO_3 [2]. However, the delicate charge balance achieved in solid solutions by conversion of Co^{3+} to Co^{2+} and oxidation Ru^{4+} to Ru^{5+} due to

formation of double perovskite structure has not been addressed. More importantly the magnetic interactions at play as the system transforms from a ferromagnetic ground state to an antiferromagnetic one is far from being clearly understood. It is with this aim the present investigation is proposed. This chapter describes detailed investigations carried out on the structural, magnetic and transport properties of solid solutions of SrRuO_3 and LaCoO_3 which form double perovskite compounds of the type $\text{La}_{2x}\text{Sr}_{2-2x}\text{Co}_{2x}\text{Ru}_{2-2x}\text{O}_6$, where $0.25 \leq x \leq 0.75$.

4.2 Results

4.2.1 X-ray Diffraction Studies

The Rietveld refined XRD patterns for all the compounds studied here are presented in Fig. 4.1. The samples crystallize in the $P2_{1/n}$ monoclinic structure with a initial increase followed by a decrease beyond $x = 0.5$ of cell volume as LaCoO_3 is added to SrRuO_3 to form a solid solutions. It may be mentioned here that the compounds with values of $x < 0.25$ and $x > 0.75$ have $Pbnm$ and $R\bar{3}c$ structures respectively and hence were not studied as they cannot be classified as double perovskites. Rietveld refinement of the XRD patterns were carried out with the $P2_{1/n}$ space group wherein the La/Sr occupy the 4e site with the fractional coordinates (0.00125, 0.00774, 0.2463), Co is at 2c (0.5, 0, 0.5), Ru is at 2d (0.5, 0, 0) and the oxygen atoms occupy three sites, viz, (0.2491, 0.2566, 0.0295); (0.2207, -0.2233, 0.0295) and (-0.06418, 0.4995, 0.2507).

The scale factor, back ground parameters, cell parameters, Co and Ru site occupancies along with instrumental broadening, totalling 17 parameters were refined in that order to obtain a good fit. As can be seen from Table 4.1, the B-site disorder was found to be least for $x = 0.5$ which also happens to be the stoichiometric double perovskite LaSrCoRuO_6 .

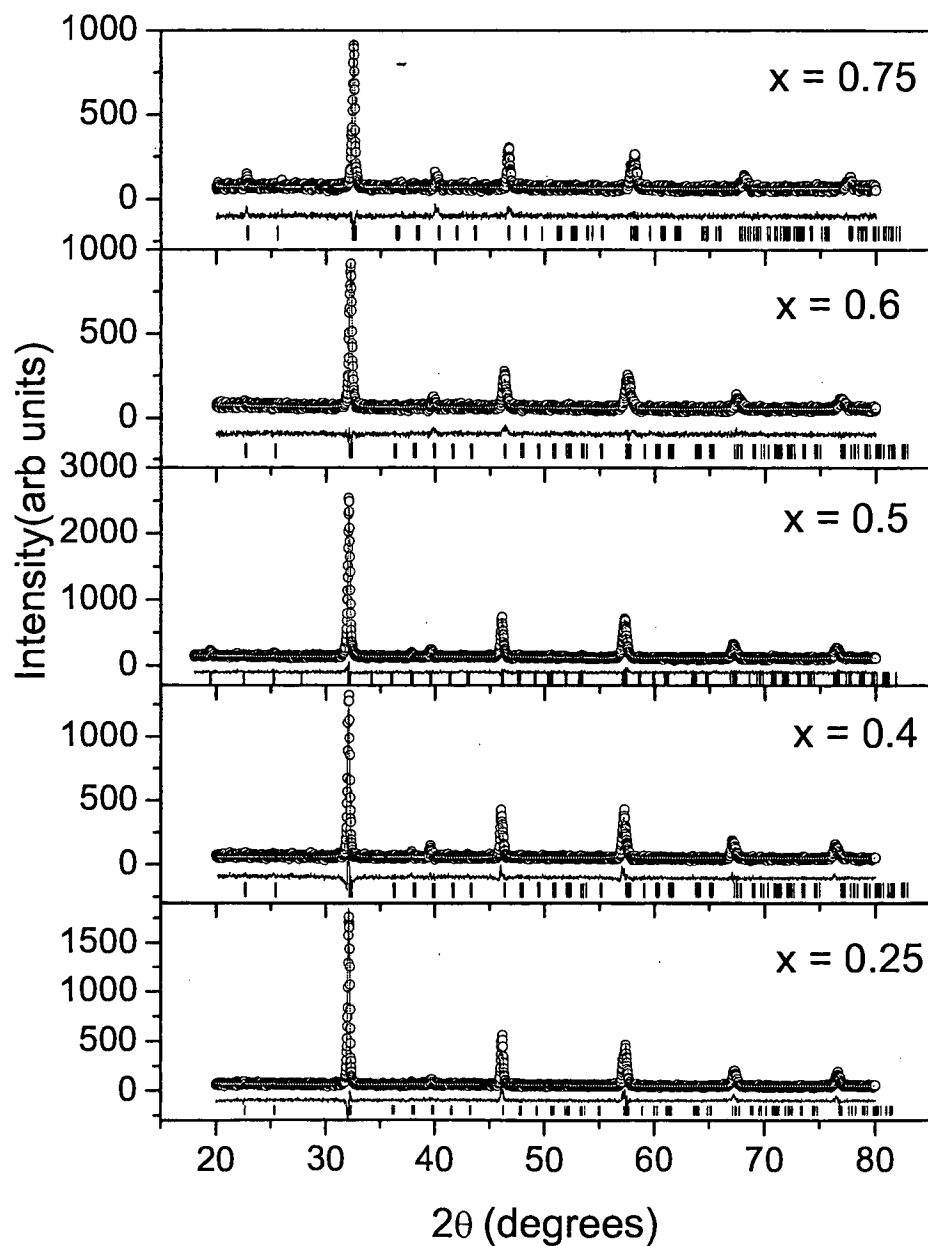


Figure 4.1: Rietveld refined XRD patterns of $\text{La}_{2x}\text{Sr}_{2-2x}\text{Co}_{2x}\text{Ru}_{2-2x}\text{O}_6$. The open circles show the observed counts and the continuous line passing through these counts is the calculated profile. The difference between the observed and calculated patterns is shown as a continuous line at the bottom of the two profiles. The calculated positions of the reflections are shown as vertical bars.

Table 4.1: Expected (E) and refined (R) occupancies of Co and Ru for different values of $\text{La}_{2x}\text{Sr}_{2-2x}\text{Co}_{2x}\text{Ru}_{2-2x}\text{O}_6$.

$x \rightarrow$		0.25		0.4		0.5		0.6		0.75	
sites	atoms	E	R	E	R	E	R	E	R	E	R
$(\frac{1}{2}, 0, \frac{1}{2})$	Co	0.25	0.19	0.4	0.26	0.5	0.49	0.5	0.36	0.5	0.45
	Ru	0.25	0.31	0.1	0.24	-	0.01	-	0.14	-	0.05
$(\frac{1}{2}, 0, 0)$	Ru	0.5	0.44	0.5	0.36	0.5	0.49	0.4	0.26	0.25	0.20
	Co	-	0.06	-	0.14	-	0.01	0.1	0.24	0.25	0.30

Table 4.2: Unit cell parameters obtained from Rietveld refinement and Curie-Weiss parameters calculated from magnetization measurements at 1000 Oe for $\text{La}_{2x}\text{Sr}_{2-2x}\text{Co}_{2x}\text{Ru}_{2-2x}\text{O}_6$. Numbers in parentheses are uncertainty in the last digit.

x	$a(\text{\AA})$	$b(\text{\AA})$	$c(\text{\AA})$	β°	$V(\text{\AA}^3)$	$\Theta_{CW}(K)$	$\mu_{eff}(\mu_B)$
0.25	5.5577(4)	5.5715(6)	7.8409(9)	90.05(2)	242.80(4)	62.8(2)	3.49(2)
0.40	5.5750(3)	5.5733(3)	7.8683(9)	90.25(2)	244.47(4)	49.5(2)	3.44(2)
0.50	5.5847(3)	5.5591(3)	7.8674(9)	90.05(2)	244.25(4)	-49.0(2)	3.87(2)
0.60	5.5626(3)	5.5287(3)	7.8245(9)	90.08(2)	240.63(4)	-20.8(2)	3.86(1)
0.75	5.4824(3)	5.5310(5)	7.7697(5)	89.93(3)	235.60(3)	-24.8(4)	3.82(1)

Interestingly the disorder or the deviation from expected occupancy is highest for $x = 0.4$ and 0.6 . This aspect needs more attention and perhaps magnetic and transport properties will shed light on this. The crystallographic parameters obtained from the above refinements along with the Curie-Weiss parameters calculated from magnetization measurements are all summarized in Table 4.2.

4.2.2 Magnetization Studies

Magnetization measurements performed in applied fields of 1000 Oe and 50 Oe during the ZFC and FC cycles for $x = 0.25, 0.4, 0.6$ and 0.75 samples are presented in Fig. 4.2. In the case of $x = 0.25, 0.4$ and 0.6 , there is a wide difference in magnetization recorded during the ZFC and FC cycles. The ZFC magnetization for these three samples, with increasing temperature increases sharply culminating into a broad hump centered around 50K. It decreases slightly with further rise in temperature before increasing sharply resulting in a peak at about 150K. The FC magnetization, on the other hand decreases continuously

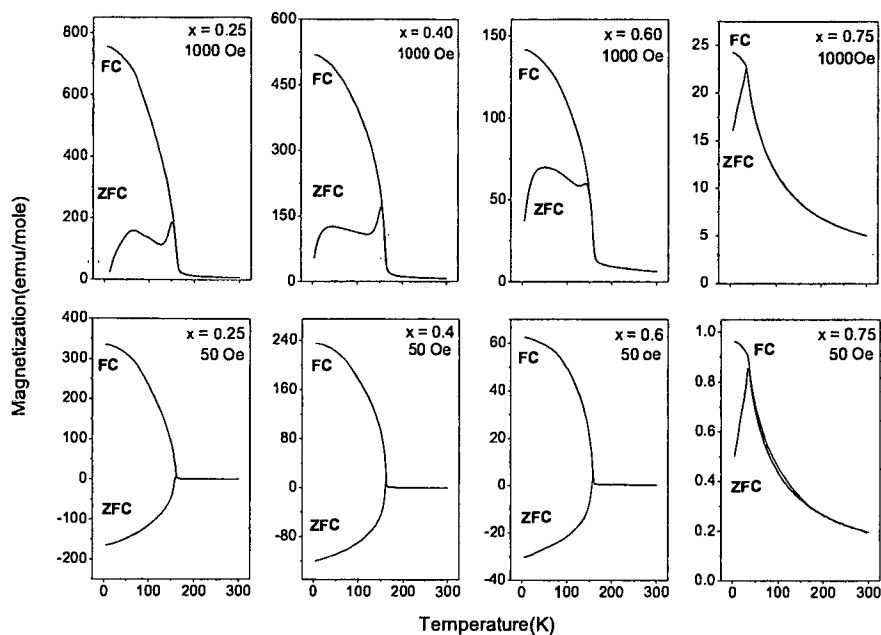


Figure 4.2: Magnetization as a function of temperature recorded in applied fields of 1000 Oe (upper panel) and 50 Oe (lower panel) in $\text{La}_{2x}\text{Sr}_{2-2x}\text{Co}_{2x}\text{Ru}_{2-2x}\text{O}_6$.

to about 167K and then settles down into a low value giving an impression of a ferro to para transition. The wide difference in the magnetization between the ZFC and FC cycle indicates a complex magnetic ground state. It may also be noted that the magnetization (emu/mole) value at 5K decreases with increasing La and Co content. Further with increasing x the irreversibility between the ZFC and FC curves is also seen to decrease until at $x = 0.75$. For this composition there is a very little difference between ZFC and FC magnetization curves and the sample seems to order antiferromagnetically at $T_N = 34$ K.

The low field magnetization measurements are also in agreement with the above. The interesting point however is the observation of negative values of magnetization for three compositions viz, $x = 0.25, 0.4$ and 0.6 during ZFC cycle. Such negative values

of magnetization were also seen in case of thermally disordered LaSrCoRuO_6 [3]. It may be noted here that all precautions were taken to ensure that negative values of magnetization are not due to remanent field of superconducting magnet of the SQUID magnetometer and this procedure has been described earlier [3]. Furthermore, as has been described-later, the initial magnetization curves recorded for these samples at 5K also exhibit negative magnetization for lower values of field (see insets of Fig. 4.4). In case of $x = 0.75$ however, the magnetization was all along positive even during the ZFC cycle. The negative magnetization could be ascribed to the presence of two magnetic sub-lattices which order in such a way as to cancel the magnetization of each other and in low fields, align the net magnetic moment in a direction opposite to the applied field. The two magnetic sublattices could be conjunctured to be ferromagnetic $\text{Ru}^{4+}\text{-O-Ru}^{4+}$ and antiferromagnetic $\text{Co}^{2+}\text{-O-Ru}^{5+}$ and/or $\text{Co}^{3+}\text{-O-Co}^{3+}$.

This fact will be more clear from the values of effective paramagnetic moment μ_{eff} and Curie-Weiss temperature Θ_{CW} obtained from the high temperature magnetization behaviour. Curie-Weiss analysis has been employed to examine the behaviour of high temperature magnetization. The plots of the inverse susceptibility ($1/\chi = H/M$) versus temperature are presented in Fig 4.3.

For $x = 0.75$, the inverse susceptibility appears to vary linearly with temperature in the range $40\text{K} < T < 300\text{K}$ but a Curie-Weiss fit to the data indicates that there is a deviation from the linear fit below 160K. This is a characteristic progressive suppression of the spin-spin interactions as temperature decreases due to spin-orbit coupling [15]. The antiferromagnetic order below 34K can then be attributed to ordering of Co spins via non-magnetic $\text{RuO}_{6/2}$ bridges [16]. Therefore the data in the range $180\text{K} < T <$

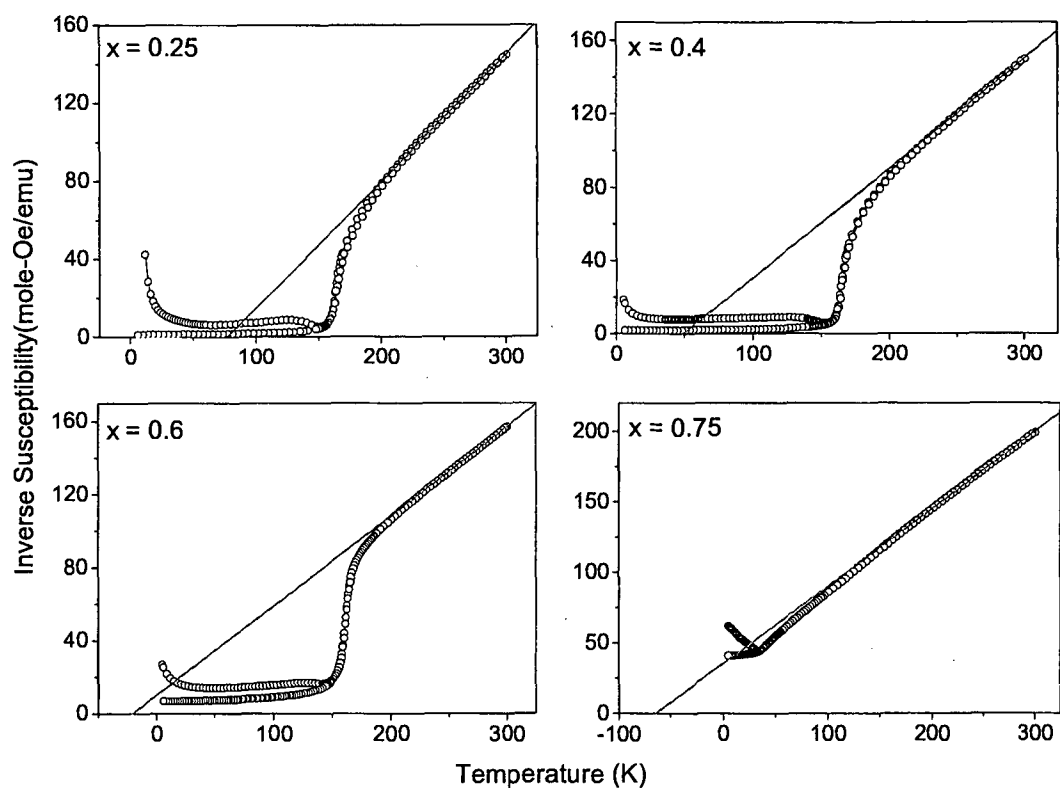


Figure 4.3: Plot of inverse magnetic susceptibility (H/M) as a function of temperature calculated using magnetization data recorded in applied field of 1000 Oe in $\text{La}_{2x}\text{Sr}_{2-2x}\text{Co}_{2x}\text{Ru}_{2-2x}\text{O}_6$.

300K was fitted to the Curie-Weiss law and the values of μ_{eff} and Θ_{CW} were obtained. Likewise for all the other compounds too, Curie-Weiss fitting was performed in the high temperature range (180K to 300K) and μ_{eff} and Θ_{CW} were calculated. These parameters are listed in Table 6.1. It can be seen that while the μ_{eff} varies only in a small range between 3.44 to 3.87 μ_B , Θ_{CW} shows a parabolic variation with x and changes its sign from negative for Co rich compounds to positive for Ru rich compositions. Negative Θ_{CW} indicates presence of stronger antiferromagnetic interactions while positive Θ_{CW} means stronger ferromagnetic interactions. In case of $x = 0.5$, the μ_{eff} value agrees very well with the calculated spin only moment value of Co^{2+} and Ru^{5+} indicating formation of a well ordered double perovskite. Another point to be noted is very large negative value of Θ_{CW} . This is an indicator of strong antiferromagnetic interactions and indeed this compound is reported to order antiferromagnetically at $T_N = 80\text{K}$ [1]. In other cases, the Ru rich compositions obviously have higher amount of $\text{Ru}^{4+}/\text{Ru}^{5+}$ leading to stronger ferromagnetic interactions and positive Θ_{CW} while the Co rich compounds have stronger antiferromagnetic interactions arising from higher amounts of $\text{Co}^{2+}/\text{Co}^{3+}$ ions. However, for all these compositions, μ_{eff} values reported in Table 6.1 can only be obtained by considering the presence of $\text{Ru}^{4+}/\text{Ru}^{5+}$ and $\text{Co}^{2+}/\text{Co}^{3+}$ redox couples. Even in case of $x = 0.75$ small deviation between ZFC and FC curves is seen below 160K (see Fig. 4.2). The presence of these magnetic ions results in formation of more than one magnetic sublattices giving rise to complex magnetic behaviour.

Isothermal Magnetization

A further confirmation of the presence of competing magnetic interactions is obtained from isothermal magnetic response recorded for all the samples at various temperatures

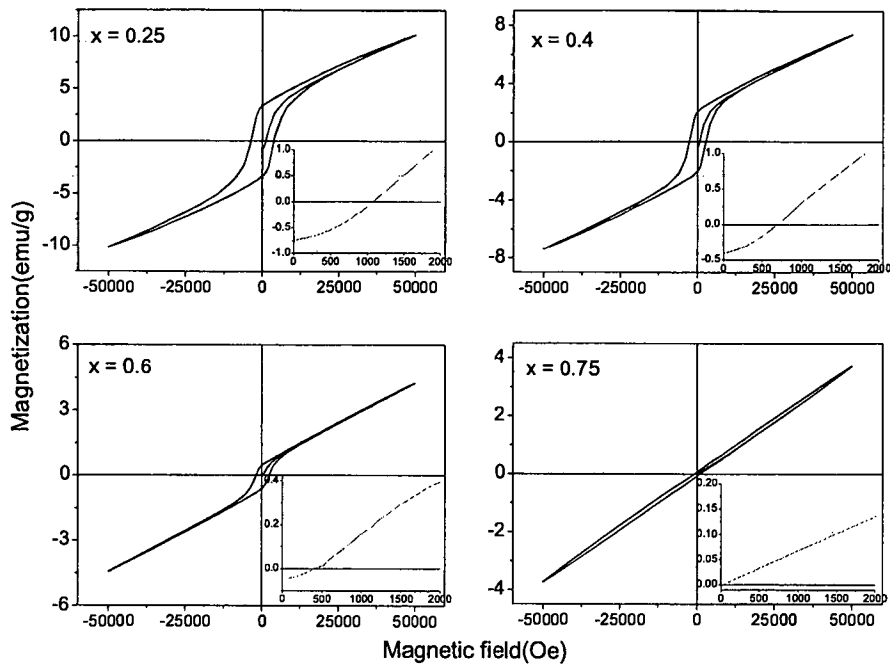


Figure 4.4: Isothermal magnetization curves recorded in the field interval of ± 5 T at 5K for $\text{La}_{2x}\text{Sr}_{2-2x}\text{Co}_{2x}\text{Ru}_{2-2x}\text{O}_6$.

in the field range of ± 50 KOe. Fig. 4.4 presents the isothermal magnetization curves for four samples ($x = 0.25, 0.4, 0.6$ and 0.75) at 5K.

It can be seen from this figure that for $x = 0.75$, the magnetization exhibits a strong field dependency and almost no hysteresis which is typical of an antiferromagnet. This is in agreement with antiferromagnetic ordering seen in M v/s T and ND measurements. On the other hand for all other compositions the isothermal magnetization exhibits a clear ferromagnetic hysteresis loop that rides on an antiferromagnetic (linear) background. Therefore the observed magnetic behavior can be ascribed to the presence of competing ferromagnetic and antiferromagnetic interactions. It is also noticed that with increase in Ru content, the area under the hysteresis loop increases implying the strengthening of ferromagnetic interactions. The initial magnetization curves shown as insets in Fig. 4.4

make it clear that the negative magnetization seen in the low field ZFC curves is indeed an intrinsic property of the materials studied here. Further it can also be seen that with the increase in x , magnetization turns positive at lower and lower values of applied field.

4.2.3 Neutron Diffraction

To establish the nature of magnetic order, ND patterns were recorded at low temperature (20K) and 300K for the two end members $x = 0.75$ and 0.25 . The Rietveld refined ND patterns at 300K for both these compounds are presented in Fig. 4.5. The parameters obtained from Rietveld refinement agree well with those obtained from XRD studies. The low temperature (20K) data shown in limited range in Fig. 4.5 indicates extra superlattice reflections due to antiferromagnetic ordering in $x = 0.75$. These reflections can be accounted for by an antiferromagnetic alignment of Co and Ru spins with a propagation vector along the $k = \frac{1}{2}, 0, \frac{1}{2}$ with respect to crystallographic axis. No long range magnetic order is visible in case of Ru rich composition ($x = 0.25$) indicating that the sharp rise in magnetization at about 160K is due to short range ferromagnetic correlations. The short range ferromagnetic correlations could be due to Ru-O-Ru linkages intervened by Co ions. These ferromagnetic correlations are present along with antiferromagnetic interactions as evidenced by the wide separation between ZFC and FC curves for this sample.

4.2.4 Resistivity Measurements

Presence of $\text{Co}^{2+/3+}$ and $\text{Ru}^{4+/5+}$ redox couples that give rise to complex magnetic behaviour will also affect the transport properties of the compounds. It may be mentioned here that while SrRuO_3 has metallic conductivity [17], LaCoO_3 exhibits semiconducting behaviour at temperatures below 300K [18]. A plot of ρ versus temperature for

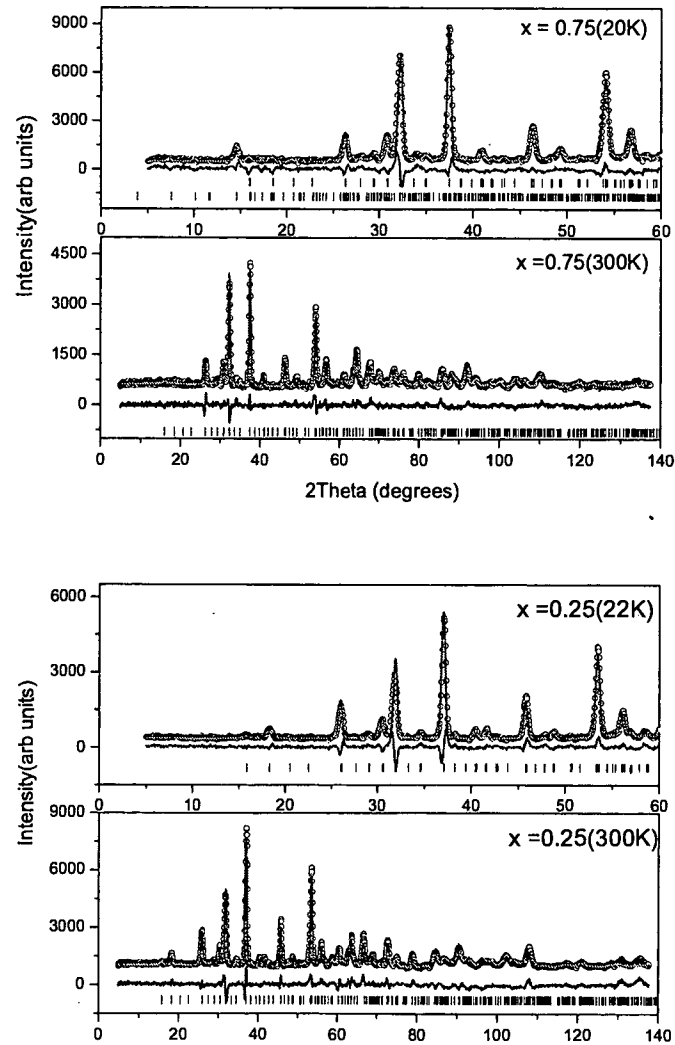


Figure 4.5: Observed (circles), calculated (line) ND patterns recorded at 300K and 20K in case of $\text{La}_{2-x}\text{Sr}_{2-2x}\text{Co}_{2x}\text{Ru}_{2-2x}\text{O}_6$ for $x = 0.25$ and $x = 0.75$. The data at 20K is shown in limited range for clarity. The continuous line at the bottom is the difference line between observed and calculated data.

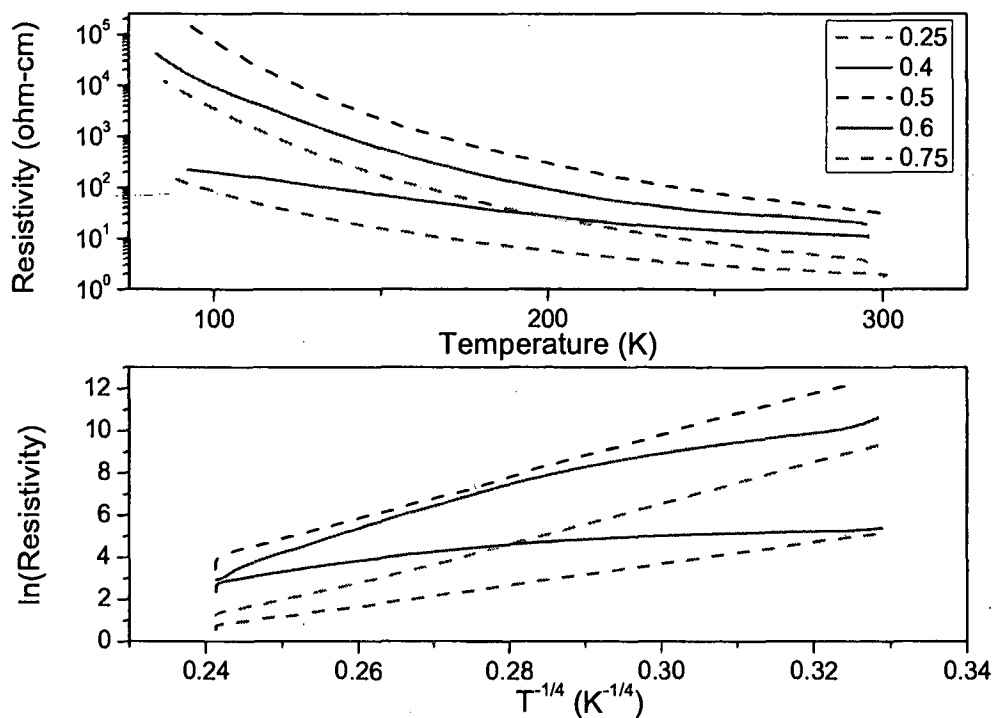


Figure 4.6: Resistivity of $\text{La}_{2x}\text{Sr}_{2-2x}\text{Co}_{2x}\text{Ru}_{2-2x}\text{O}_6$ as a function of temperature (upper panel). The lower panel shows a plot of $\log \rho$ versus $T^{-1/4}$ for all compositions.

$\text{La}_{2x}\text{Sr}_{2-2x}\text{Co}_{2x}\text{Ru}_{2-2x}\text{O}_6$ with $0.25 \leq x \leq 0.75$ is presented in Fig.4.6.

All the samples show semiconducting behaviour. It may be noted that the ordered composition ($x = 0.5$) has the highest magnitude of resistivity due to absence of any Ru-O-Ru type conducting paths. Since the resistivity of this ordered sample follows Mott's variable range hopping (VRH) behaviour, $\log \rho$ versus $T^{-1/4}$ has been plotted in the lower panel of fig. 4.6 for all compositions. It can be seen that along with $x = 0.5$, $x = 0.25$ and 0.75 samples show a linear behaviour indicating conduction to be in accordance with Mott's VRH law. Resistivity behaviour for $x = 0.4$ and 0.6 compounds however, is quite different. Here the ρ varies in a very narrow range and exhibits a hump at about 160K which coincides with the sharp rise in magnetization data of these samples. Rietveld analysis have also shown maximum B-site occupancy disorder for the same two

compositions and therefore could be linked to the presence of more number of Ru-O-Ru conducting paths.

4.2.5 X-ray Photoelectron Spectroscopic Studies

All the above properties hint at presence of $\text{Co}^{2+}/\text{Co}^{3+}$ and $\text{Ru}^{4+}/\text{Ru}^{5+}$ pairs in $\text{La}_{2x}\text{Sr}_{2-2x}\text{Co}_{2x}\text{Ru}_{2-2x}\text{O}_6$ compounds in different proportion. Core level XPS of Co and Ru can give an indication of valency of these ions and therefore a measure of such proportion. Fig 4.7 presents the background subtracted Co and Ru core level spectra for $x = 0.25, 0.5$ and 0.75 . Both Co $2p$ and Ru $3p$ spectra show two clear peaks due to spin orbit splitting and the associated satellite peaks (marked as *). In the case of Co, the main peaks are separated by a spin orbit splitting of about 15eV while in the case of Ru this splitting is about 22eV [19]. In the case of $x = 0.25$ and 0.75 , the main peaks are broadened as compared to $x = 0.5$ and show considerable spectral weight on the higher energy side especially in case of Co $2p$. Therefore the spectra have been fitted with two Gaussians perhaps corresponding to Co^{2+} and Co^{3+} species. Likewise the Ru $3p$ spectra also shows a presence of two types of Ru ions which are most likely to be Ru^{4+} and Ru^{5+} species. In case of $x = 0.5$, Co $2p$ and Ru $3p$ spectra can be well represented by a single gaussian which can be attributed to divalent Co and pentavalent Ru respectively. Further in case of $x = 0.25$ which has majority Ru content, the intensity of the peak corresponding to Ru^{4+} is higher than that of the peak corresponding to Ru^{5+} while the $x = 0.75$ sample shows higher amounts of Co^{3+} species as compared to Co^{2+} . This is as expected, the unexpected however is the corresponding contents of $\text{Co}^{2+}/\text{Co}^{3+}$ in $x = 0.25$ and $\text{Ru}^{4+}/\text{Ru}^{5+}$ in $x = 0.75$. Using the percentage concentration ratios of $\text{Co}^{2+}/\text{Co}^{3+}$ and $\text{Ru}^{4+}/\text{Ru}^{5+}$ obtained from area under the respective Gaussian's, an attempt was made

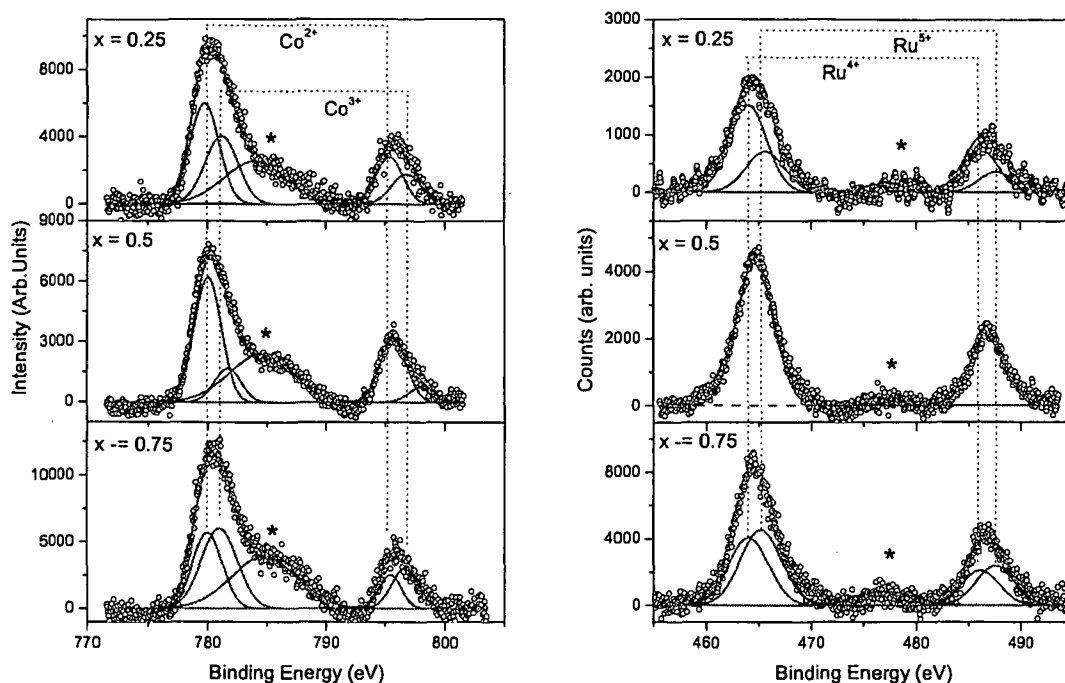


Figure 4.7: Co(2p) and Ru(3p) core level spectra along with fitted curves for $\text{La}_{2x}\text{Sr}_{2-2x}\text{Co}_{2x}\text{Ru}_{2-2x}\text{O}_6$ compounds.

to calculate the spin only magnetic moments for the two compositions. The calculations were made assuming $S = 3/2$ for Co^{2+} and Ru^{5+} , $S = 1$ for Co^{3+} and $S = 2$ for Ru^{4+} . The calculated values were found to be $3.5\mu_B$ in case of $x = 0.75$ and $3.25\mu_B$ in case of $x = 0.25$. Although slightly lower, they seem to agree with the trend reported in Table 6.1.

4.3 Discussion

In the case of ordered double perovskite, LaSrCoRuO_6 , the presence of highly acidic Ru^{5+} stabilizes the high spin Co^{2+} and thereby suppressing various electronic transitions that Co ion can have. However, when the order is disturbed, Co-O-Co and Ru-O-Ru linkages are formed and the trivalent state of Co and tetravalent state of Ru are favoured. Such

has been the case in $\text{La}_{2-x}\text{Sr}_x\text{CoRuO}_6$ [6].

In $\text{La}_{2x}\text{Sr}_{2-2x}\text{Co}_{2x}\text{Ru}_{2-2x}\text{O}_6$, present studies indicate that with the addition of LaCoO_3 to SrRuO_3 leads to stabilization of double perovskite phase is seen in a broad concentration region of $0.25 \leq x \leq 0.75$. These double perovskites, apart from Co^{2+} -O- Ru^{5+} interactions will also contain Co-O-Co and Ru-O-Ru linkages. This is amply clear from the magnetic and transport properties described above. As mentioned above, these linkages favour trivalent and tetravalent states for Co and Ru respectively. Further, under such conditions it is well known that HS and IS states of Co^{3+} are promoted [20]. Presence of HS/IS Co^{3+} ions will give rise to additional magnetic interactions. Further Ru^{4+} -O- Ru^{4+} is known to be ferromagnetic and metallic in conduction [21]. The observed competition between ferromagnetic and antiferromagnetic interactions can be therefore attributed to presence of Ru^{4+} and Co^{3+} ions. The presence of these ions along with occupancy disorder leads to formation of Ru rich and Co rich magnetic sublattices which order ferromagnetically and antiferromagnetically respectively. This is well supported by the decrease in magnetization values with increasing Co content and sharper rise of magnetization in case of Ru rich compositions. Only when there is a complete ordering of the B-site cations, Co^{2+} and Ru^{5+} ions are stabilized as nearest neighbours and long range antiferromagnetic order is established. The antiferromagnetic order seen in $x = 0.75$ can be attributed to antiferromagnetic cobalt ordering via non-magnetic $\text{RuO}_6/2$ bridges [16].

The presence of more than one magnetic sublattice also explains the negative magnetization observed in ZFC cycle of low field magnetization data. The ferromagnetic sublattice formed due to presence of tetravalent Ru ions orders at around 160K. This

polarizes the paramagnetic Co spins in a direction opposite to the applied field leading to magnetic compensation and negative values of magnetization. With a decrease in Ru content, the ferromagnetic sublattice becomes weaker and the field required to reverse the magnetization to positive values also decreases. This can be very clearly seen from the initial magnetization curves presented in Fig. 4.4.

4.4 Conclusion

In summary, the structural, transport and magnetic properties in $\text{La}_{2x}\text{Sr}_{2-2x}\text{Co}_{2x}\text{Ru}_{2-2x}\text{O}_6$ have been studied. Double perovskite structure with space group $\text{P}2_{1/n}$ is stabilized over a wide composition range from $x = 0.25$ to 0.75 . With the increase in Co content, ferromagnetic interactions are found to weaken and at $x = 0.75$, the compound orders antiferromagnetically at $T_N = 34\text{K}$. This interplay of ferromagnetic and antiferromagnetic interactions is attributed to presence of $\text{Ru}^{4+}/\text{Ru}^{5+}$ and $\text{Co}^{2+}/\text{Co}^{3+}$ redox couple in all the compounds. The only exception to this is the ordered compound $x = 0.5$ wherein Co and Ru exist in divalent and pentavalent states respectively representing an archtype double perovskite. The presence of different magnetic sublattices leads to magnetic compensation and negative magnetization. This can be explained by polarization of paramagnetic Co spins by the ferromagnetic Ru^{4+} sublattice in a direction opposite to applied field.

References

- [1] J-W. G. Bos, J. P. Attfield, *Chem. Matter.*, **16**, 1822 (2004).
- [2] A. Mamchik, W. Dmowski, T. Egami, I-W. Chen, *Phys. Rev. B*, **70**, 104410 (2004).
- [3] P. S. R. Murthy, K. R. Priolkar, P. A. Bhoje, A. Das, P. R. Sarode and A. K. Nigam, *J. Magn. Magn. Mater.*, **322**, (2010) 3704.
- [4] D. Kim, B. L. Zink, F. Hellman, S. McCall, G. Cao and J. E. Crow, *Phys. Rev. B*, **67**,100406 (2003).
- [5] Dlouhá M, Hejtmánek J, Jiráček Z, Knížek K, Tomeš P and Vratislav S J. *Magn. Mater.*, doi:10.1016/j.jmmm.2009.06.035 (2009).
- [6] P. Tomeš, J. Hejtmánek and K. Knížek, *Sol. State Sci.*, **10**, 486 (2008).
- [7] G. Cao, S. McCall, M. Sheppard, J. E. Crow, R. P. Guertin, *Phys. Rev. B*, **56**, 321 (1997).
- [8] J. B. Goodenough, *J. Phys. Chem. Solids*, **6**, 287 (1958).
- [9] R. H. Potze, G. A. Sawatzky and M. Abbate, *Phys. Rev. B*, **51**, 11501 (1995).
- [10] T. Saitoh, T. Mizokawa, A. Fujimori, M. Abbate, Y. Takeda and M. Takano, *Phys. Rev. B*, **55**, 4257 (1997).

- [11] R. Caciuffo, D. Rinaldi, G. Barucca, J. Mira, J. Rivas, M. A. S. Rodriguez, P. G. Radaelli, D. Frorani and J. B. Goodenough, *Phys. Rev. B*, **59**, 1068 (1999).
- [12] P. G. Radaelli and S. -W. Cheong, *Phys. Rev. B*, **66**, 094408 (2002).
- [13] L. Pi, A. Maignan, R. Retoux and B. Raveau, *J. Phys: Condens. Matter*, **14**, 7391 (2002).
- [14] S. Manoharan, R. K. Sahu, D. Elefant and C. M. Schneider, *Solid State Commun.*, **125**, 103 (2003).
- [15] C. -Q. Jin, J. -S. Zhou, J. B. Goodenough, Q. Q. Liu, J. G. Zhou, L. X. Yang, Y. Yu, R. C. Yu, T. Katsura, A. Shatskiy, E. Ito, *Proc. Natl. Acad. Sci.*, **105**, 7115 (2008).
- [16] S. Kim, R. I. Dass and J. B. Goodenough, *J. Solid State Chem.*, **181**, 2989 (2008).
- [17] P. B. Allen, H. Berger, O. Chauvet, L. Forro, T. Jarlborg, A. Junod, B. Revaz and G. Santi, *Phys. Rev. B* **53**, 4393 (1996); L. Klein, J. S. Dodge, C. H. Ahn, G. J. Snyder, T. H. Geballe, M. R. Beasley and A. Kapitulnik, *Phys. Rev. Lett.*, **77**, 2774 (1996).
- [18] P. M. Raccah and J. B. Goodenough, *Phys. Rev.*, **155**, 932 (1967); V. G. Bhide, D. S. Rajoria, G. R. Rao, and C. N. R. Rao, *Phys. Rev. B* **6**, 1021 (1972).
- [19] J. F. Moulder, W. F. Stickle, P. E. Sobol, K. D. Bomben, "*Handbook of X-ray Photoelectron Spectroscopy*" (Physical Electronics, 1995)
- [20] K. Knížek, Z. Jiráček, J. Hejtmánek, P. Novák, *J. Phys.: Condens. Matter*, **18**, 3285 (2006).
- [21] I. I. Mazin and D. J. Singh, *Phys. Rev. B* **56**, 2556 (1997).

Chapter 5

Effect of B-site Dopants on Magnetic and Transport Properties of LaSrCoRuO_6

5.1 Introduction

Perovskites containing 3d (B) and 4d or 5d (B') transition metal cations attract attention because of the strong competition between antiferromagnetic and ferromagnetic coupling and a complex interplay of spin charge and orbital degrees of freedom [1]. Some of these perovskites like $\text{Sr}_2\text{FeMoO}_6$ and $\text{Sr}_2\text{FeReO}_6$ display itinerant ferrimagnetism and large low field magnetoresistance [2, 3]. These properties can be effectively altered by substituting the B or B' site ions with other transition metal ions [4, 5].

Ruthenium based double perovskites are interesting and have been studied extensively for their unusual magnetic and transport properties. Ru(V) containing perovskites exhibit many interesting properties like itinerant electron magnetism and co-existence of antiferromagnetic order and superconductivity [6, 7, 8, 9, 10]. Similarly Ru(IV) based double perovskites containing a transition metal ion on the B' site present a wide variety of ground states that depend on Ru 4d and O 2p covalent mixing and the itinerancy of π^* electrons [11].

LaSrCoRuO_6 is another double perovskite that provides a unique opportunity to examine the interplay of cationic order, charge balance and complex magnetic interactions between two transition metal ions [12, 13]. Its crystal structure is composed of corner-shared CoO_6 and RuO_6 octahedra arranged in a pseudocubic array in the rocksalt arrangement. The degree of ordering is known to affect the magnetic and transport properties due to changes in magnetic interactions and in cationic valence. Effects of anti-site disorder on the magnetic and transport properties due to La or Sr doping in LaSrCoRuO_6 have been investigated [12, 14, 15]. LaSrCoRuO_6 compound is a semiconductor with ideal valence states HS Co^{2+} ($3d^7$ high-spin configuration) and Ru^{5+} ($4d^3$) [18]. The change of composition (La or Sr doping) introduces mobile electrons in La richer samples or holes in Sr richer samples. Magnetically these compounds are reported to be antiferromagnetic with two magnetic face centered cubic (fcc) sublattices consisting of Co and Ru. Both the sublattices order with type II antiferromagnetic structure which would mean that the spins in [111] planes in succession Co-Ru-Co-Ru alternate as $+/+/-/-$. This marginalizes the Co-O-Ru nearest neighbour interactions and the ordering is governed by a competition between linear Co-O-Ru-O-Co and 90° Co-O-O-Co antiferromagnetic exchange paths [12, 15].

Effect of substitutions at the B or B' sites in LaSrCoRuO_6 have not been studied so far. In particular, the effect of antisite disorder will be very important as it will alter the magnetic interactions present in LaSrCoRuO_6 and perhaps result in more complex magnetic ground state. Antisite disorder in ferromagnetic double perovskites like $\text{Sr}_2\text{FeMoO}_6$ is known to affect magnetic and transport properties of these compounds [16]. Herein we report, structural, transport and magnetic properties of $\text{LaSrCo}_{1-x}\text{Ru}_{1+x}$

for $-0.3 \leq x \leq 0.4$ and $\text{LaSrCo}_{1-y}\text{Cu}_y\text{RuO}_6$ $y \leq 0.2$ studied using X-ray diffraction (XRD), Neutron diffraction (ND), resistivity and magnetization as a function of temperature and magnetic field. The compounds studied herein have a fixed A-site variance though varying Goldschmidt tolerance factor t [17] and redox active $\text{Co}^{2+/3+}$ and $\text{Ru}^{4+/5+}$ couples resulting essentially due to antisite disorder. This study elucidates the complex role of coexisting localized electrons belonging to both Co and Ru d orbitals as well as some itinerant π^* electrons of Ru: t_{2g} parentage that arise due to presence of $\text{Ru}^{4+/5+}$ and $\text{Co}^{2+/3+}$ redox couples on the structural, magnetic and transport properties of substituted LaSrCoRuO_6 .

5.2 Results

5.2.1 $\text{LaSrCo}_{1-x}\text{Ru}_{1+x}\text{O}_6$

The stability of the ordered double perovskite phase with $P2_1/n$ symmetry is determined within the composition region $x = 0.1$ to 0.4 for Ru and $x = -0.1$ to -0.3 for Co from the Le Bail refinement of XRD patterns which are presented in Fig. 5.1. The lattice parameters obtained from refinement are presented in Table 5.1. LaSrCoRuO_6 which has Co^{2+} and Ru^{5+} ions occupying the B-site represents a perfectly ordered perovskite with NaCl type ordering of its B-sites cations. Substitution of Ru for Co and Co for Ru creates not only an antisite disorder in the Co-O-Ru matrix but also a change in the formal valence of the B-site ions.

While the effect of disorder can be clearly seen in Fig. 5.2 on the superlattice reflection $(\frac{1}{2}, \frac{1}{2}, \frac{1}{2})$ at $\sim 19.5^\circ$,

the linear variation of the cell volume with x as seen in Fig. 5.3(a) indicates a change in the formal valence of B-site cations. It may be noted here that Co^{3+} has a smaller

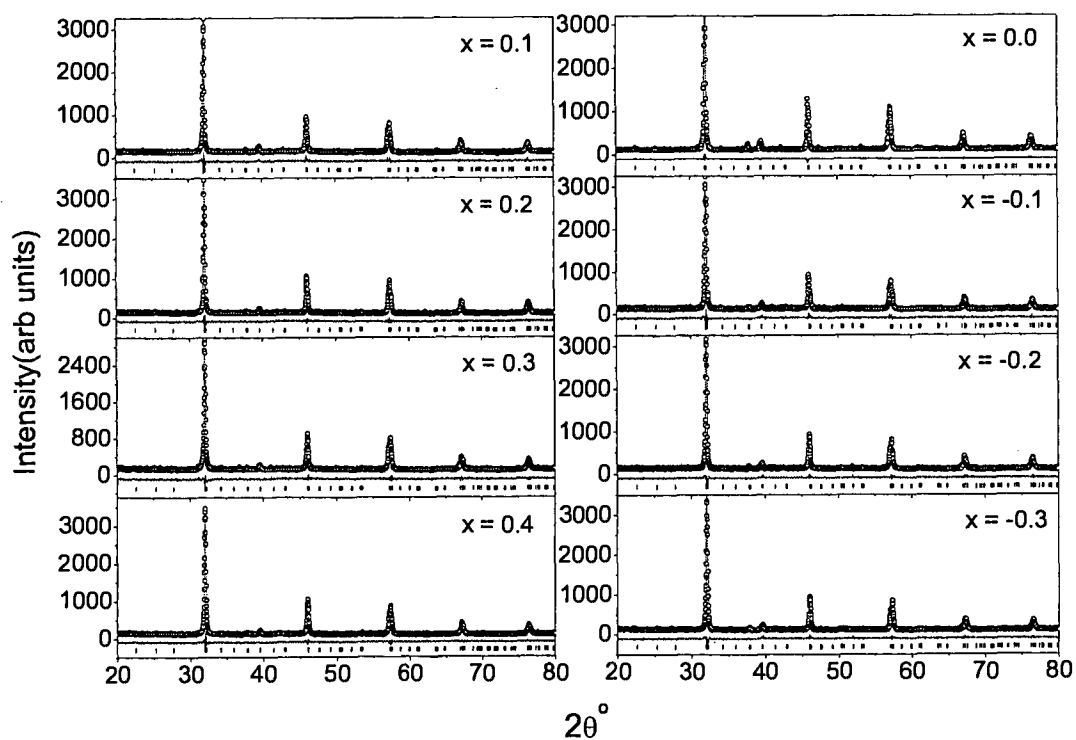


Figure 5.1: Le bail fitted XRD patterns for $\text{LaSrCo}_{1-x}\text{Ru}_{1+x}\text{O}_6$. The data points are indicated as circles and the solid line through them is the fit to the data. The difference pattern is shown at the bottom along with tick marks indicating Bragg reflections.

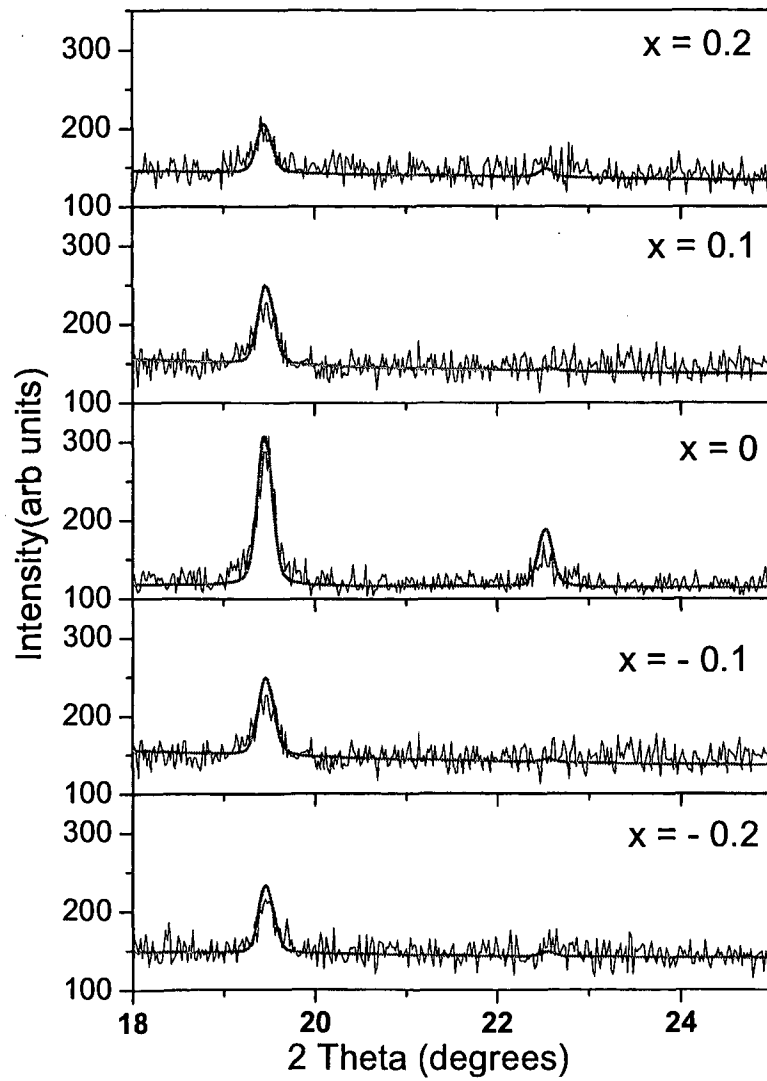


Figure 5.2: Variation of intensity of superlattice $(\frac{1}{2}, \frac{1}{2}, \frac{1}{2})$ reflection with increasing Ru ($x > 0$) and Co ($x < 0$) doping.

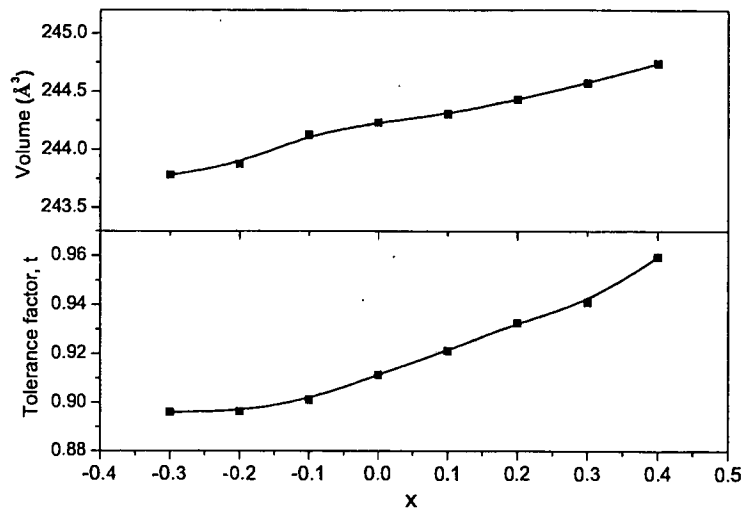


Figure 5.3: (a) Composition dependence of the unit cell volume in $\text{LaSrCo}_{1-x}\text{Ru}_{1+x}\text{O}_6$. (b) Variation of tolerance factor t with x in $\text{LaSrCo}_{1-x}\text{Ru}_{1+x}\text{O}_6$.

ionic radius than Co^{2+} while the ionic radius of Ru^{4+} is larger than Ru^{5+} and hence the cell volume decreases for Co doped compounds and increases with Ru doping. The linear variation of the unit cell volume also confirms the existence of single-phase solid solutions for all values of composition x reported here.

An interesting aspect of substitution of Co at the Ru site is the comparatively large change in the monoclinic cell angle, β . It decreases from 90.05° in the undoped sample to 89.9° for the Co doped sample ($x = -0.2$) whereas remains nearly constant for the Ru doped samples. This could be due to the large charge and size difference between Co and Ru and/or due to a deviation from pseudo-cubic symmetry arising because of clustering of similar B-site ions due to charge balance. With increasing Co substitution from $x = -0.1$ to -0.3 , the electrons are likely to be removed from the Co ions leading to a valency increase of Co from $2+$ to $3+$ as the Ru ions are in highly oxidized state. But this does not satisfy the charge balance and will require some of the Ru^{5+} to reduce

Table 5.1: Room temperature structural parameters obtained from Le Bail fitting and high temperature magnetic and transport properties for $\text{LaSrCo}_{1-x}\text{Ru}_{1+x}\text{O}_6$. Here a , b , c and β denote unit cell parameters, V is the unit cell volume, μ_{eff} (μ_B/fu) and Θ_{CW} represent effective magnetic moment and Curie Weiss temperature respectively and T_p is temperature of peak magnetization seen in ZFC curve. Numbers in parentheses are uncertainty in the last digit.

x	-0.3	-0.2	-0.1	0	0.1	0.2	0.3	0.4
a (Å)	5.5866(4)	5.5861(3)	5.5858(3)	5.5847(4)	5.5847(4)	5.5846(3)	5.5843(4)	5.584(3)
b (Å)	5.5551(6)	5.5553(5)	5.5555(5)	5.5592(6)	5.5541(5)	5.5533(6)	5.5524(4)	5.5515(5)
c (Å)	7.8599(5)	7.8612(5)	7.8634(5)	7.8673(4)	7.8646(4)	7.8641(5)	7.8629(5)	7.8636(4)
β	89.92(2)	89.98(1)	89.96(2)	90.05(2)	90.04(2)	90.04(1)	90.04(1)	90.05(1)
V (Å ³)	243.68(4)	243.87(3)	244.12(3)	244.25(4)	244.31 (3)	244.43(3)	244.57(4)	244.74(3)
μ_{eff}	5.52(2)	5.35(1)	–	5.47(2)	5.50(2)	5.42(2)	5.39(2)	5.58(3)
Θ_{CW} (K)	24(1)	37(1)	–	-49(1)	21(1)	25(1)	25(1)	0(1)
T_p (K)	42(1)	47(1)	–	70(1)	53(1)	52(1)	54(1)	49(1)

to Ru^{4+} . Consequently, the charge and the size difference between Ru and Co ion may lead to a deviation in β . This can be also be visualized in Fig. 5.3(b) where t is plotted as a function of composition x . While t increases from about 0.91 for $x = 0$ to 0.95 for $x = 0.4$ (Ru-rich compositions), it decreases to 0.89 for $x = -0.3$ (Co-rich compositions) indicating that the substitution of Ru for Co allows for a better matching of A-O and B(B')-O bond distances than the replacement of Ru by Co.

The structural changes occurring due to Ru and Co doping will have an effect on the magnetic properties. Fig.5.4 presents the temperature variation of magnetization measured between 5K and 300K in an applied field of 1000Oe and the magnetic susceptibility ($\chi = M/H$) calculated from thereon for four representative compounds. The difference between ZFC and FC magnetization curve reveals a complex magnetic structure. In the high temperature region ($200\text{K} \leq T \leq 300\text{K}$), χ was fitted to the Curie-Weiss equation

$$\chi = C/(T - \Theta_{CW})$$

where $C = N_A(\mu_{eff}\mu_B)^2/3k_B$ is the Curie constant and Θ_{CW} is the Curie-Weiss temperature. Effective moment per formula unit ($\mu_{eff} = g[S(S + 1)]^{1/2}$) calculated from

C and Θ_{CW} obtained for fitting for all the compounds along with undoped compound, LaSrCoRuO_6 are enlisted in Table 5.1. From the analysis of the high temperature magnetization in the doped systems, it can be inferred that Co ions are in high spin (HS) or intermediate spin (IS) state and that the magnetic interaction for all x are dominated by nearest neighbour interactions of the superexchange type between HS/IS $\text{Co}^{2+,3+}$ and low spin (LS) $\text{Ru}^{4+,5+}$ ions. A second observation is that the effective magnetic moment does not vary with x . The nearly constant value of μ_{eff} in the $x \in (-0.3 \text{ to } 0.4)$ region can only be explained on the basis of presence of HS and IS states for Co^{3+} and Ru^{4+} . In the case of undoped sample, the type of long range magnetic order is characterized by $\Theta_{CW} \sim -50\text{K}$ and a clear antiferromagnetic transition at $T_N \approx 80 \text{ K}$ [12]. In case of Ru and Co doped samples, Θ_{CW} is positive indicating presence of additional ferromagnetic interactions. In Ru doped samples, positive Θ_{CW} can be understood to be due to ferromagnetic $\text{Ru}^{4+}\text{-O-Ru}^{4+}$ interactions.

The presence of such interactions is supported by the sudden rise of magnetization at about 160K which is close to ferromagnetic ordering temperature of SrRuO_3 . The presence of any SrRuO_3 impurity phase however, can be ruled out as no additional reflections are seen in the diffraction pattern even at 40% Ru doping. The competition between the ferromagnetic and antiferromagnetic interactions can result in magnetic frustration below the peak temperature $T_p \sim 50\text{K}$ seen in ZFC magnetization curve. The nature of magnetic order will be confirmed later using neutron diffraction. Positive values of Θ_{CW} even in Co doped compounds is puzzling. It can only be understood to be due to presence of $\text{Co}^{2+/3+}$ and $\text{Ru}^{4+/5+}$ redox pairs for charge balance. The nearly constant values of μ_{eff} supports this conjuncture well. Sudden rise seen in magnetization at around 160K

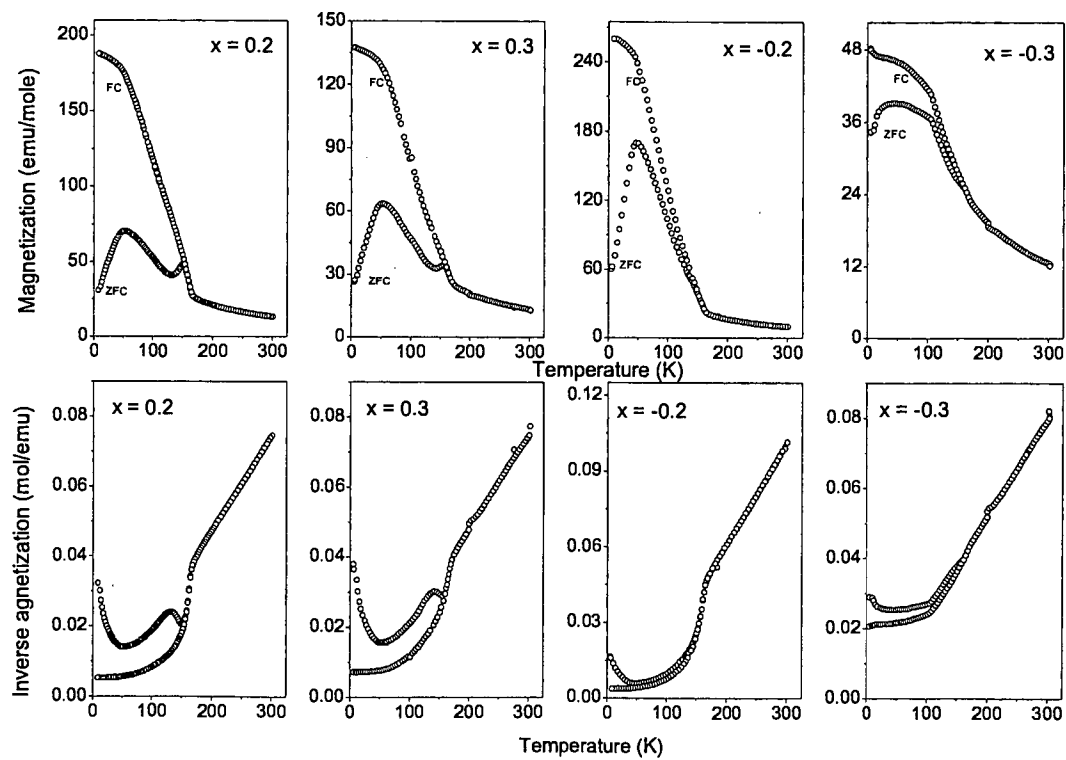


Figure 5.4: Magnetization curves for $\text{LaSrCo}_{1-x}\text{Ru}_{1+x}\text{O}_6$ during the ZFC and FC cycle recorded at 100 Oe.

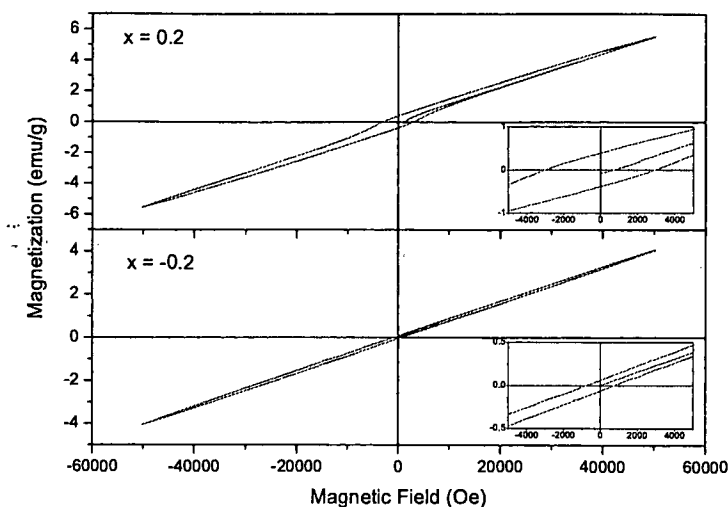


Figure 5.5: Isothermal magnetization recorded at 5K in the field range of ± 5 T for two different values of x belonging to $\text{LaSrCo}_{1-x}\text{Ru}_{1+x}\text{O}_6$. Insets show the expanded (± 4500 Oe) loops.

seen in 20% and 30% Co doped samples is also in agreement with the above view. The presence of Ru^{4+} leads to the ferromagnetic Ru-Ru interaction where the Ru 4d electrons form itinerant-electron π^* bands of t-orbital parentage. Presence of competition between ferromagnetic and antiferromagnetic interactions is also evident from magnetization curves of Co doped samples. Furthermore, the hysteresis loop recorded for 20% Co doped compound at 5K in magnetic field interval of ± 5 Tesla and presented in Fig. 5.5 exhibits a small irreversibility (see the expanded loop in the inset of Fig. 5.5) indicating existence of weak ferromagnetic interactions along with antiferromagnetic interaction. In the case of Ru doped compound however, presence of clear magnetic hysteresis riding on smoothly increasing background indicates a strong competition between ferro and antiferromagnetic interactions.

In order to understand this competition further, magnetization was recorded in a low field of 500Oe. Here the magnetization response in the Ru doped samples is completely

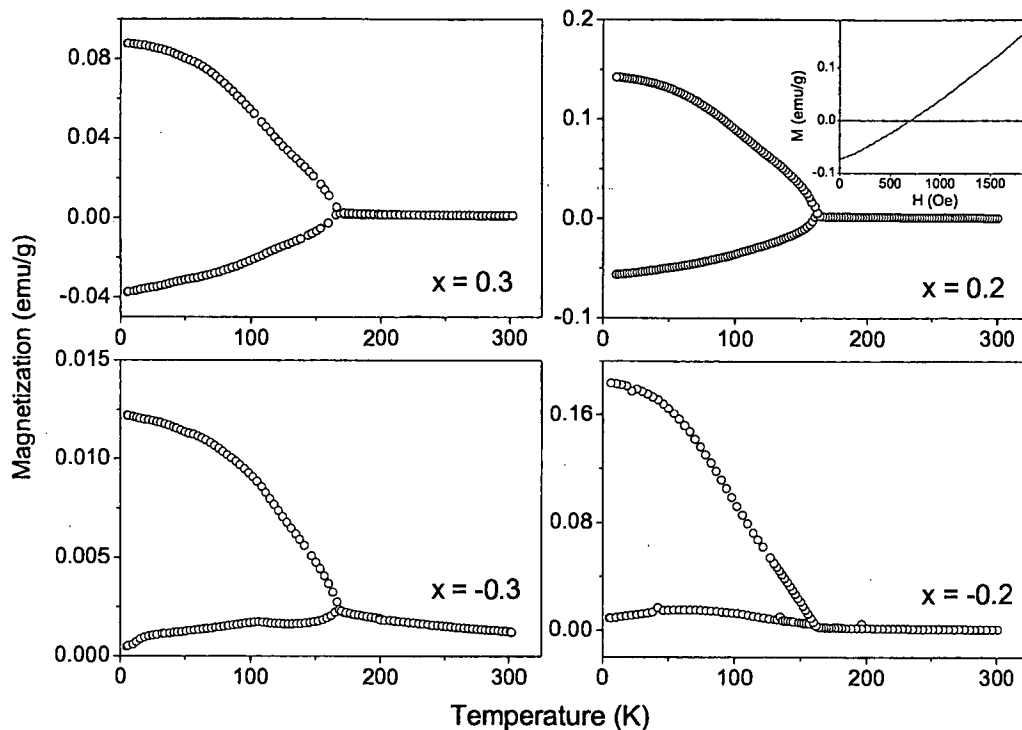


Figure 5.6: Low field (50 Oe) magnetization data as a function of temperature for $\text{LaSrCo}_{1-x}\text{Ru}_{1+x}\text{O}_6$. The inset in plot of $x = 0.2$ shows the initial magnetization curve as a function of applied field for the same sample.

different as compared to that measured at 1000 Oe as can be seen in the Fig 5.6.

During the ZFC cycle, the magnetization is negative at the lowest temperature and increases continuously with increase in temperature. At about 158K and crosses over to the positive side, exhibits a peak at 162K signifying a transition from a magnetically ordered to a paramagnetic state. The magnetization remains positive during the entire FC cycle exhibiting a relatively sharp rise at 162K, precisely the same temperature at which ZFC shows a cusp. In the case of Co doped samples, although there is a large difference between ZFC and FC magnetization curves, the magnetization is positive during both cycles. It may be emphasized here that care has been taken to make sure that the remanent field of SQUID magnetometer was less than ± 13 Oe during these low field

measurements. Furthermore, in the inset of M versus T plot for $x = 0.2$ shows the initial magnetization curve for the same sample measured as a function of field. It can be clearly seen that magnetization is negative in fields up to about 700 Oe.

Neutron diffraction was employed to determine the magnetic structure of two compounds, $x = 0.2$ and -0.2 . The data taken at 300K and 20K is presented in Fig. 5.7. The data at 20K is shown in very limited range in order to highlight the magnetic reflections. Very weak reflections due to AFM ordering were observed (marked in Fig. 5.7) in the positions given by the propagation vector along the pseudocubic 111 direction with respect to the crystallographic $P2_1/n$ cell [12, 19]. The observation of the lines with $k = (1/2, 0, 1/2)$ defines that AFM arrangement in each sublattice is of type II, consisting of ferromagnetic [111] planes. The values of magnetic moments at 20K obtained from neutron diffraction are $\mu(\text{Co}) \sim \mu(\text{Ru}) = 1.0\mu_B$ for $x = 0.2$ and $\mu(\text{Co}) \sim \mu(\text{Ru}) = 0.6\mu_B$ for $x = -0.2$.

This implies that the spins in (111) planes alternate as $+/+/-/-$ for Co/Ru/Co/Ru. Such a AFM arrangement also indicates that the magnetic ordering is governed by the 180° Co-O-Ru-O-Co AFM exchange paths [20, 21]. Earlier studies report the presence of competing 90° Co-O-O-Co AFM exchange paths that can be a cause of magnetic frustration leading to the low values of long-range-ordered moments as detected by neutron scattering [15].

The temperature dependence of the resistivity for $\text{LaSrCo}_{1-x}\text{Ru}_{1+x}\text{O}_6$ with $x = -0.2$, 0 and 0.2 are plotted in the Fig 5.8.

The samples exhibit semiconducting behavior in the entire measured range of temperature. The addition of Ru and Co dopants is found to decrease the resistivity significantly

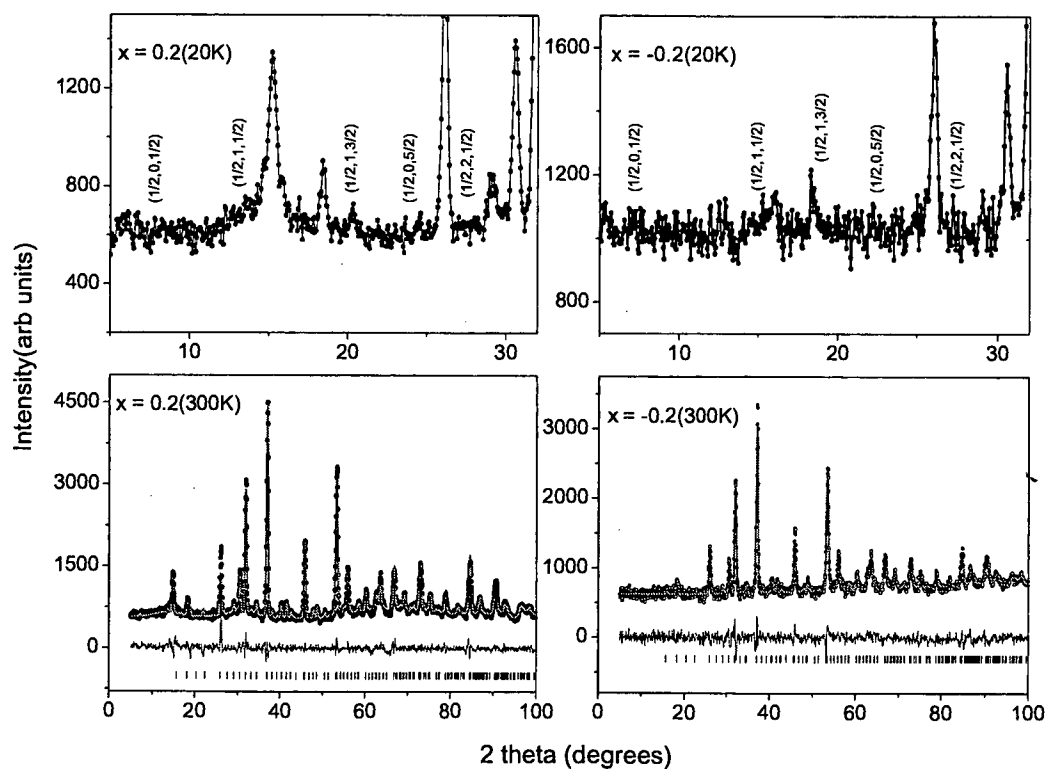


Figure 5.7: Neutron diffraction patterns recorded at 300K and 20K for $x = 0.2$ and -0.2 of the series $\text{LaSrCo}_{1-x}\text{Ru}_{1+x}\text{O}_6$. The 300K data is presented in the 2θ range of 5° to 100° as circles along with Rietveld refined curve (solid line through the data) and the difference curve at the bottom. The 20K data is shown in limited range to highlight the weak magnetic reflections (marked with corresponding (h,k,l) values).

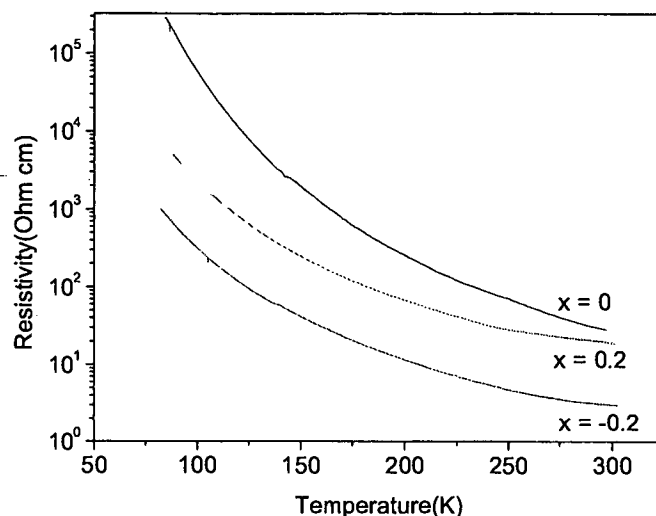


Figure 5.8: Resistivity as a function of temperature for $\text{LaSrCo}_{1-x}\text{Ru}_{1+x}\text{O}_6$ compounds where $x = -0.2, 0$ and 0.2

by about two orders of magnitude. In the case of Ru doped samples, the decrease in resistivity is due to the formation of metallic $\text{Ru}^{4+} - \text{O} - \text{Ru}^{4+}$ chains in these samples which essentially result due to excess Ru concentration. On the other hand in the case of Co doped samples, structural and magnetization studies indicated the presence of $\text{Co}^{2+/3+}$ and $\text{Ru}^{4+/5+}$ redox pairs. The presence of Ru^{4+} results in itinerant electrons due to population of π^* antibonding orbitals. This explains the decrease in resistivity in case of Co doped samples.

5.2.2 $\text{LaSrCo}_{1-y}\text{Cu}_y\text{RuO}_6$

In Fig. 5.9 XRD patterns of 10% and 20% Cu doped LaSrCoRuO_6 compounds is presented. Both these compounds are single phase and the structural parameters obtained from Le Bail fitting are presented in Table 5.2 along with that of undoped sample, LaSrCoRuO_6 for ready comparison. The unit cell volume in Cu doped samples is slightly lower. This could be because of slightly smaller ionic radii of Cu^{2+} (0.73\AA) than that of

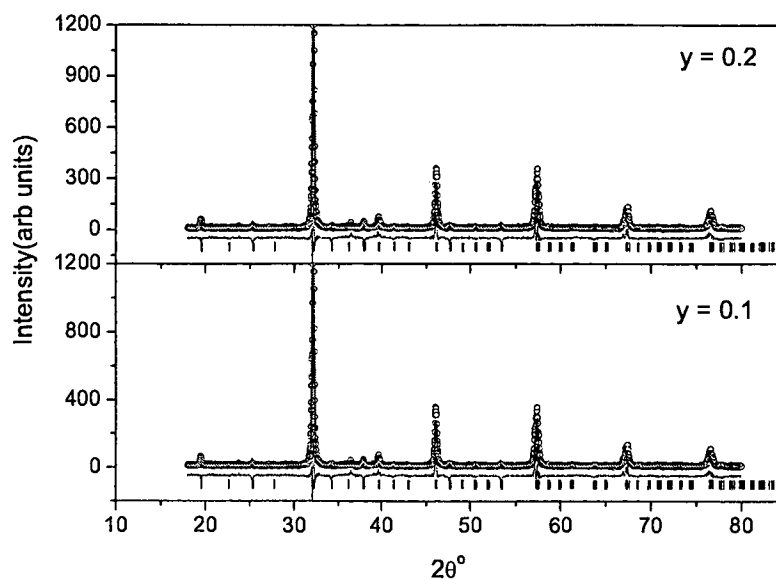


Figure 5.9: XRD patterns of $\text{LaSrCo}_{1-y}\text{Cu}_y\text{RuO}_6$ for $y = 0.1$ and 0.2 along with best fitted line and difference line shown at the bottom. The ticks indicate the positions of allowed Bragg reflections.

Co^{2+} (0.745\AA) in HS configuration. Substitution of Cu for Co is expected not to alter charge balance and therefore Ru will be in $5+$ state as in undoped compound. However, the substitution is expected to alter magnetic and transport properties. Substitution of Cu in $\text{Sr}_2\text{HoRuO}_6$ type double perovskites is reported to exhibit a coexistence of antiferromagnetism and superconductivity [10].

Magnetization for the two Cu doped samples, recorded during ZFC and FC cycles in an applied field of 1000 Oe is presented in Fig. 5.10.

In both cases, both ZFC and FC magnetization curves increases with decreasing temperature culminating into a broad peak centered at 42K and 47K respectively for $y = 0.1$ and 0.2 samples. Inverse magnetization plotted for both the samples in lower panel of Fig. 5.10 shows linear variation down to 100K . The calculated susceptibility ($\chi = M/H$) was fitted to Curie-Weiss equation. The values of μ_{eff} and Θ_{CW} extracted from

Table 5.2: Room temperature structural parameters obtained from Le Bail fitting and high temperature magnetic and transport properties for $\text{LaSrCo}_{1-x}\text{Ru}_{1+x}\text{O}_6$. Here a , b , c and β denote unit cell parameters, μ_{eff} and Θ_{CW} represent effective magnetic moment and Curie Weiss temperature respectively and T_p is temperature of peak magnetization seen in ZFC curve. Numbers in parentheses are uncertainty in the last digit.

x	0	0.1	0.2
a (Å)	5.5847(4)	5.5621(2)	5.5627(2)
b (Å)	5.5592(6)	5.5518(2)	5.5544(2)
c (Å)	7.8673(4)	7.8684(2)	7.8714(2)
β	90.05(2)	90.23(1)	90.28(1)
Volume (Å ³)	244.25(4)	242.98(4)	243.20(3)
μ_{eff} (μ_B /fu)	5.47(2)	5.18(1)	5.01(1)
Θ_{CW} (K)	-49(1)	-32.1(3)	-7.3(4)
T_p (K)	70(1)	47(1)	42(1)

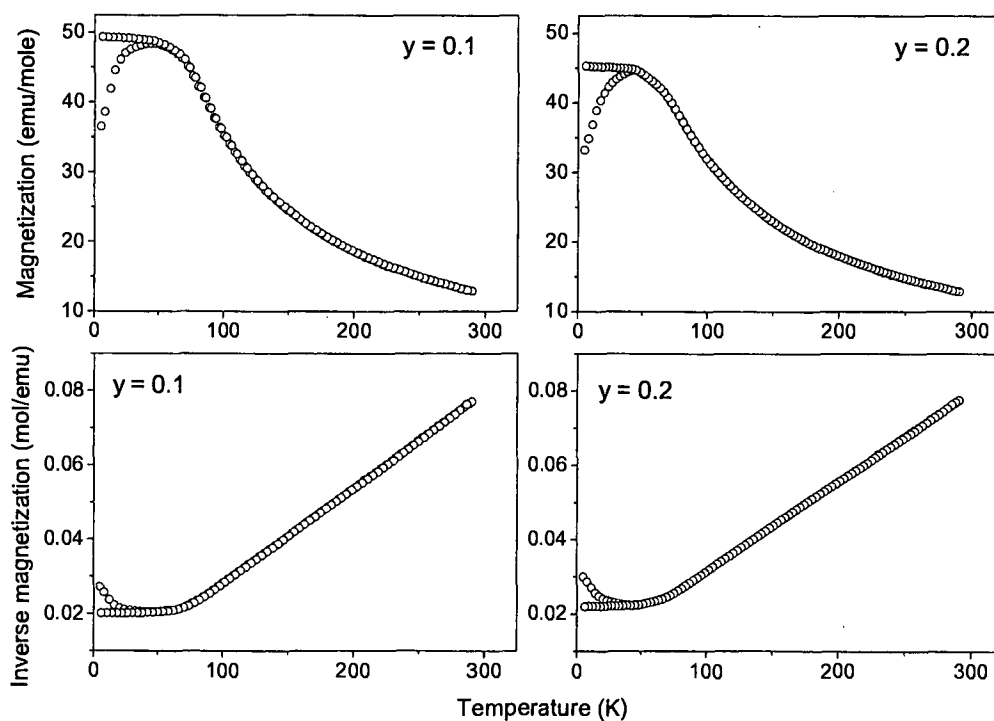


Figure 5.10: ZFC and FC magnetization curves for $\text{LaSrCo}_{1-y}\text{Cu}_y\text{RuO}_6$ recorded at $H = 1000\text{Oe}$.

fitting are listed in Table 5.2. The values of Θ_{CW} obtained are both negative although much smaller than that of the undoped sample. Negative values indicate dominance of antiferromagnetic interactions in these compounds. Theoretically calculated spin only moments using Ru^{5+} ($S = 3/2$), Co^{2+} ($S = 3/2$) and Cu^{2+} ($S = 1/2$) for both the doped samples are in good agreement with the experimentally obtained values. This behavior is unlike that seen in case of Ru and Cu doped compounds. The large splitting observed between ZFC and FC magnetization curves is absent. Dominant interaction is antiferromagnetic. Even with presence of a impurity ion (Cu^{2+}) there appears to be no clustering or change in valence of Ru or Co.

In order to see the effect of Cu doping on the transport properties of LaSrCoRuO_6 , electrical resistivity in the temperature range $10\text{K} < T < 300\text{K}$ has been measured and presented in Fig. 5.11. It appears that with Cu substitution, there is very little change in resistivity as compared to the undoped sample. This can be attributed to Cu^{2+} replacing Co^{2+} ions inhibiting the conversion of Ru^{5+} to Ru^{4+} or formation of Ru-O-Ru chains.

5.3 Discussion

Substitution at B-site in ordered LaSrCoRuO_6 double perovskite allows an opportunity to probe the changes in structural, magnetic and transport properties due to creation of $\text{Co}^{2+/3+}$ and $\text{Ru}^{4+/5+}$ redox couples in an environment with fixed A-site variance and linearly varying Goldschmidt tolerance factor. In the entire doping region, for both the series, the double perovskite structure is preserved.

The magnetic and transport properties of $\text{LaSrCo}_{1-x}\text{Ru}_{1+x}\text{O}_6$ on the other hand show significant changes due to the creation of Ru^{4+} and Co^{3+} species in both Co doped and

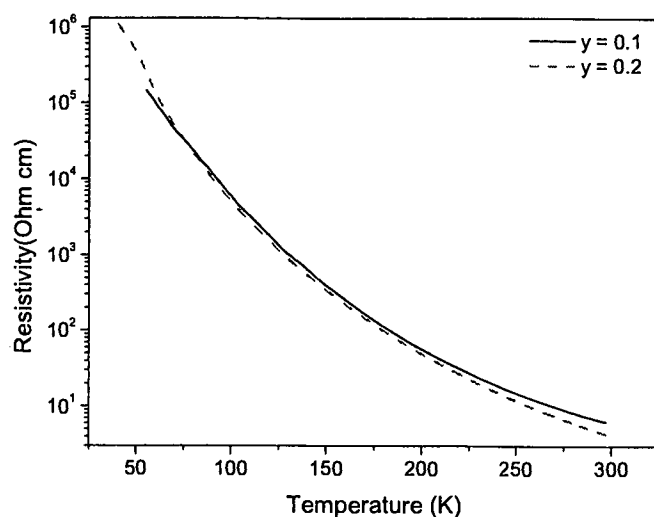


Figure 5.11: Temperature variation of electrical resistivity for $\text{LaSrCo}_{1-y}\text{Cu}_y\text{RuO}_6$ where $y = 0.1$ and 0.2 .

Ru doped compounds. The antisite disorder resulting due to excess Ru or Co leads to creation of Ru^{4+} and Co^{3+} species in addition to Ru^{5+} and Co^{2+} ions in order to maintain charge balance. In the case of undoped compound, LaSrCoRuO_6 , there are two competing magnetic interactions, the linear Co-O-Ru-O-Co and the 90° Co-O-O-Co . In the Ru and Co doped compounds these interactions get diluted at the expense of new interactions of the type $\text{Ru}^{4+/5+}\text{-O-Ru}^{4+/5+}$ and those involving HS/IS Co^{3+} . The sharp rise in magnetization seen at about 160K in all Co and Ru doped compounds can be attributed to ferromagnetic interactions arising due to Ru-O-Ru nearest neighbor interactions. As in case of SrRuO_3 , such an interactions leads to filling up of π^* band and lowering of resistivity as compared to undoped LaSrCoRuO_6 . The negative magnetization displayed by Ru rich compounds in low applied fields can then be understood to be due to polarization of paramagnetic Co spins by Ru-O-Ru ferromagnetic interactions below the Ru sublattice ordering temperature (160K). The Co spins are polarized in a

direction opposite to applied magnetic field giving rise to magnetic compensation and negative magnetization. In the case of Co doped compounds, no negative magnetization is observed although there is the steep rise of magnetization below 160K. Instead, only a large variation between ZFC and FC magnetization curves is seen. This could be understood to be due to clustering of similar types of ions in the sample. This is also indicated by decrease in the strength of ferromagnetic interactions with increasing Co content.

The competition between magnetic interactions observed in case of Co and Ru substituted compounds is reduced or eliminated with Cu substituting Co in LaSrCoRuO_6 . The magnetic properties clearly indicated presence of antiferromagnetic interactions from negative Θ_{CW} and the magnetization behavior in the entire temperature range. Since Cu^{2+} substitutes Co^{2+} , the charge on Ru remains unaltered. Since the ionic sizes of the two ions are also similar, there are no major structural changes. This results in nearly similar magnitude of resistivity as in the case of undoped LaSrCoRuO_6 .

It is known that partially filled 3d levels of Co in SrRuO_3 are well below the conduction band of Ru^{4+} . Therefore it is favorable to transfer a electron from Ru to Co, even though such electrons may become localized. The resulting Co^{2+} state will move its level closer to but still below Ru 4d levels. Thus the presence of highly acidic Ru^{5+} is more stabilizing for high spin Co^{2+} leading to an ordered lattice. Doping of Co and Ru will result in formation of Co-O-Co and Ru-O-Ru networks respectively. From XANES studies reported in [13], it is clear that Co-Co pairs will favor the trivalent state, and likewise Ru-Ru pairs would favor the tetravalent states. Therefore the observed magnetic behavior reflects the general competition between the itinerant ferromagnetism and the

antiferromagnetic superexchange coupling between Co-Co pairs, further modified by the interactions between Ru and Co. Since Cu substitution does not favor formation of Ru-O-Ru or Co-O-Co networks but instead disturbs the existing magnetic interactions especially the 90° Co-O-O-Co interaction, antiferromagnetism appears to be strengthened.

5.4 Conclusion

The study of magnetic and transport properties of ceramic samples $\text{LaSrCo}_{1-x}\text{Ru}_{1+x}$ and $\text{LaSrCo}_{1-y}\text{Cu}_y\text{RuO}_6$ leads to the following conclusions:

1. The ordered double perovskite phase exists for $-0.3 \leq x \leq 0.4$.
2. The thermally activated electrical resistivity is associated with nearest neighbor hopping between Co and Ru ions via linking oxygen atoms. The decrease in resistivity with Ru and Co doping is due to formation of Ru^{4+} and more holes in the Ru d band.
3. The Co and Ru doped compounds also show an increase in magnetization due to the formation of ferromagnetic Ru-O-Ru interactions.
4. In case of Cu doped compounds, the antiferromagnetism strengthens due to the suppression of the competing 90° Co-O-O-Co antiferromagnetic interactions.

References

- [1] D. D. Sarma, *Curr. Opin. Solid State Mater. Sci*, **5**, 261 (2001).
- [2] K. L. Kobayashi, T. Kimura, H. Sawada, K. Terakura, Y. Tokura, *Nature*, **395**, 677 (1998).
- [3] J. Gopalakrishnan, A. Chattopadhyay, S. B. Ogale, T. Venkatesan, R. L. Greene, A. J. Millis, K. Ramesha, B. Hannoyer and G. Marest, *Phys. Rev. B*, **62**, 9538 (2000).
- [4] F. Sriti, A. Maignan, C. Martin and B. Raveau, *Chem. Mater.*, **13**, 1746 (2001).
- [5] X. M. Feng, G. H. Rao, G. Y. Liu, H. F. Yang, W. F. Liu, Z. W. Ouyang, L. T. Yang, Z. X. Liu, R. C. Yu, C. Q. Jin and J. K. Liang, *J. Phys. Condens. Matter*, **14**, 12503 (2002).
- [6] P. D. Battle and W. J. Macklin, *J. Solid State Chem.*, **52**, 138 (1984).
- [7] N. Kamegashira, T. Mori, A. Imamura, and Y. Hinatsu, *J. Alloys Compd.*, **302**, L6 (2002).
- [8] Y. Doi, Y. Hinatsu, K. Oikawa, Y. Shimojo and Y. Morii, *J. Mater. Chem.*, **10**, 797 (2000)

- [9] M. K. Wu, D. Y. Chen, F. Z. Chien, S. R. Sheen, D. C. Ling, C. Y. Tai, G. Y. Tseng, D. H. Chen and F. C. Zhang, *Z. Phys. B: Condens. Matter*, **102**, 37 (1997).
- [10] N. G. Parkinson, P. D. Hatton, J. A. K. Howard, C. Ritter, F. Z. Chien and M. K. Wu, *J. Mater. Chem.*, **13**, 1468 (2003).
- [11] R. I. Dass, J. Q. Yan and J. B. Goodenough, *Phys. Rev. B*, **69**, 094416 (2004).
- [12] J-W. G. Bos and J. P. Attfield, *Chem. Matter.*, **16**, 1822 (2004).
- [13] A. Mamchik, W. Dmowski, T. Egami and I-W Chen, *Phys. Rev. B*, **70**, 104410 (2004).
- [14] P. Tomeš, J. Hejtmánek and K. Knížek, *Solid State Sci.*, **10**, 486 (2008).
- [15] M. Dlouhá, J. Hejtmánek, Z. Jiráček, K. Knížek, P. Tomeš and S. Vratislav S J. *Magn. Magn. Mater.*, doi:10.1016/j.jmmm.2009.06.035 (2009).
- [16] D. Serrate, J. M. de Teresa and M. R. Ibarra, *J. Phys. Condens. Matter.*, **19**, 023201 (2007).
- [17] V. M. Goldschmidt, *Skrifter Nordske Videnskaps-Akad. Oslo I, Mat-Naturvidensk Kl.*, **8**, 2 (1926).
- [18] S. H. Kim and P. D. Battle, *J. Sol. State. Chem.*, **114**, 174 (1995).
- [19] J-W. G. Boss and J. P. Attfield, *J. Mater. Chem.*, **15**, 715 (2005).
- [20] J-W. G. Bos, and J. P. Attfield, *Phys. Rev. B*, **70**, 174434 (2004).
- [21] E. Rodriguez, M. L. Lopez, J. Campo, M. L. Veiga and C. Pico, *J. Mater. Chem.*, **12**, 2798 (2002).

Chapter 6

Role of A-site Cations in Magnetic and Transport Properties of LaSrCoRuO_6

6.1 Introduction

SrRuO_3 is a metallic ferromagnetic perovskite with a Curie temperature $T_C \approx 160$ K [1] while CaRuO_3 , though metallic does not have any long range magnetic order in its RuO_3 arrays [2]. Although the substitution of more acidic Ca^{2+} ion for Sr^{2+} narrows the π^* band, but this band narrowing leads to a progressive transition to a nonmagnetic state ($J = 0$) as a result of spin-orbit coupling $\lambda \mathbf{L} \cdot \mathbf{S}$. Substitution of trivalent transition metal ions like Cr^{3+} , Mn^{3+} , Fe^{3+} attracts the holes, it introduces into π^* band to give an antiferromagnetic M^{3+} - Ru^{5+} interaction that stabilizes ferrimagnetic clusters as has been shown by Maignan et al [3]. Double perovskites of the type $\text{La}_2\text{RuM}^{2+}\text{O}_6$, wherein the $4d$ electron configuration is localized on an octahedral Ru^{4+} ion, the spin-orbit coupling makes ground state have a principal quantum number $J = 0$ [4]. Bos et al [5] have shown that the Co^{2+} spins of $\text{La}_2\text{CoRuO}_6$ order antiferromagnetically below $T_N = 25$ K. Ordered double perovskites, $(\text{LaA})\text{CoRuO}_6$ which contain Co^{2+} and Ru^{5+} ions in alternate octahedral sites are variable range hopping semiconductors and order antiferromagneti-

cally with two opposed Co and two opposed Ru spin sublattices with $T_N = 96$ K for A = Ca and 85 K for A = Sr [6, 7]. In our studies reported herein in previous chapters, we found that even a small disorder in Co and Ru occupancies gives rise to a competition between ferromagnetic and antiferromagnetic interactions. The ferromagnetic interactions are a result of Ru-O-Ru coupling that arise due to disorder in Co-O-Ru-O-Co arrays. The low field (50 Oe) magnetization measurements on ordered LaSrCoRuO_6 shows a wide separation between zero field cooled and field cooled data indicating the presence of weak ferromagnetic interactions in the antiferromagnetically ordered sample. These ferromagnetic interactions could be due to tiny, undetectable amounts of SrRuO_3 impurity or due to presence of Ru-O-Ru interactions at the antiphase boundaries or due to the presence of Sr at the A site of the perovskite sub-cell. SrRuO_3 impurity can be ruled out because even a tiny amount would have shown ferromagnetic like hysteresis below its ordering temperature. The hysteresis loop recorded at 5K in the applied fields of ± 5 T and presented in Figure 6.1 shows absolutely no hysteresis. In order to distinguish between the remaining two possibilities, a comparative study between magnetic and transport properties of the two double perovskites LaSrCoRuO_6 and LaCaCoRuO_6 is presented here. Both the samples have the similar structural and magnetic ground states. Antiphase boundaries in both the samples have the possibility of Ru-O-Ru interactions being present. The difference however will be in the occupancy of the A sites - in one case they will be occupied by La and Sr while in the other La and Ca will be present.

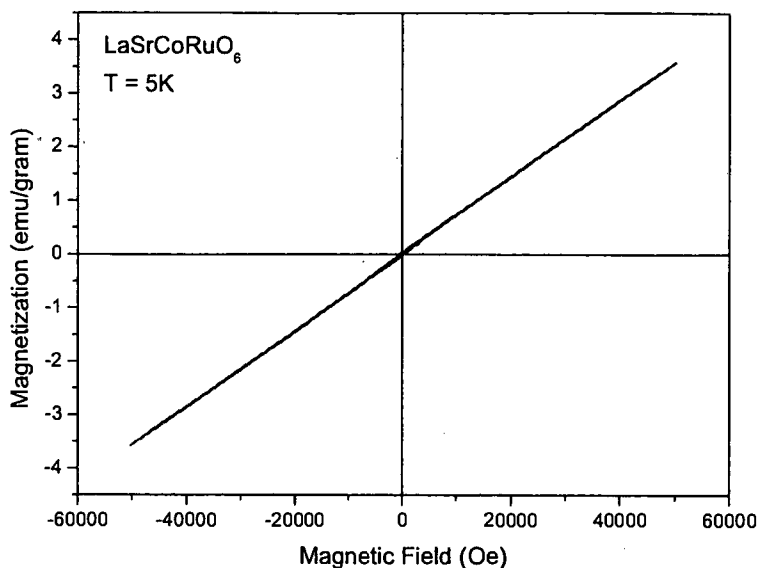


Figure 6.1: Isothermal Magnetization recorded at 5K in applied fields of ± 5 T for LaSrCoRuO₆

6.2 Structural Studies

The Rietveld refined XRD patterns for the two samples LaSrCoRuO₆ and LaCaCoRuO₆ are presented in Fig. 6.2. Both the samples were prepared in an identical way and the final annealing temperature was 1300°C. Rietveld analysis of the XRD data showed that both the compounds crystalize with the monoclinic P2₁/n superstructure. Expectedly, the cell volume of the LaSrCoRuO₆ was found to be larger than that of LaCaCoRuO₆. The P2₁/n superstructure allows for rocksalt ordered arrangement of Co and Ru over the perovskite B-sites, whereas La and Sr/Ca are randomly distributed over the A-sites. In Rietveld refinement, the scale factor, background parameters, cell parameters, Co and Ru site occupancies along with instrumental broadening, totaling to 17 parameters were refined in that order to obtain a good fit. The crystallographic parameters obtained from the refinement of the XRD patterns along with Curie-Weiss parameters calculated from

the magnetization measurements are summarized in Table 6.1. Both the samples can be termed as ordered as a negligible degree of Co/Ru disorder (about 2% in case of LaSr and about 1% in case of LaCa) is seen. A perfectly ordered structure would mean that Co and Ru should be in divalent and pentavalent states respectively. Bond valence sum calculations, values of which are given in Table 6.1 confirm the presence of only Co^{2+} and Ru^{5+} states in both the double perovskites. Another point worth noting is the Co-O-Ru bond angle. The three Co-O-Ru bond angles have been obtained from Rietveld refinement of room temperature XRD data. These values are presented in Table 6.1. While our values are in good agreement with those reported in Refs. [6] and [7], those in case of LaSrCoRuO_6 are distinctly larger as compared to the ones in LaCaCoRuO_6 . The larger Co-O-Ru bond angle will imply straighter bond. A straighter bond will lead to population of the π^* band of Ru and therefore higher conductivity.

6.3 Transport Measurements

The temperature dependence of the resistivity for LaSrCoRuO_6 and LaCaCoRuO_6 is as shown in the Fig. 6.3. Both the compounds are found to be variable range hopping semiconductors. The temperature dependence of resistivity was fitted in the entire range using a VRH equation

$$\rho(T) = \rho_0 \sqrt{T/T_0} \exp^{(T_0/T)^{1/d+1}} \quad (6.1)$$

where d is the dimensionality of the variable-range hopping process ($d = 3$).

Resistivity of LaSrCoRuO_6 exhibits a peculiar behaviour. Below 160K, the resistivity of the sample is lower than that expected from the resistivity calculated using thermally activated type temperature dependence. This can be regarded as to be due to some

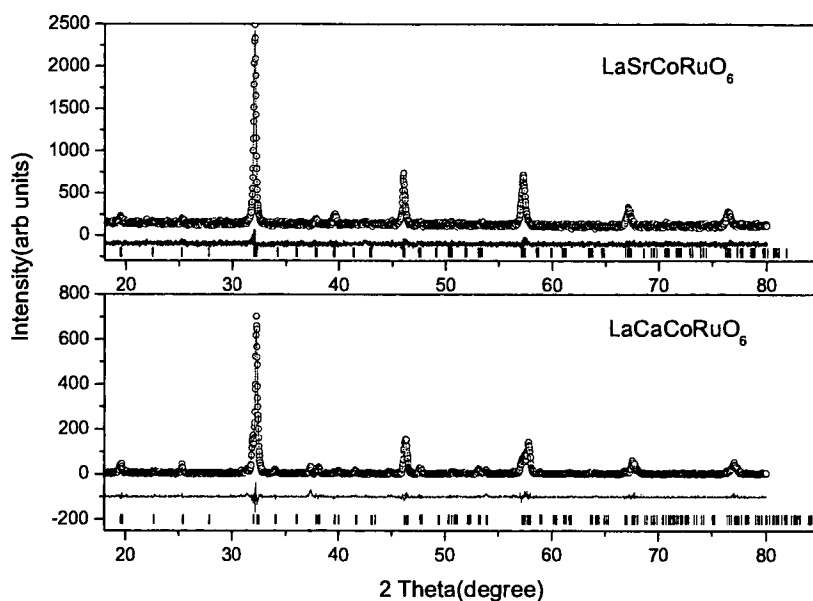


Figure 6.2: Rietveld refined XRD patterns for LaSrCoRuO_6 (upper panel) and LaCaCoRuO_6 (lower panel). The open circles show the observed counts and the continuous line passing through these counts is the calculated profile. The difference between the observed and calculated patterns is shown as a continuous line at the bottom of the two profiles. The calculated positions of the reflections are shown as vertical bars.

Table 6.1: Unit cell parameters, Co and Ru site occupancies obtained from Rietveld refinement, Bond Valence Sums, Bond angles between Co and Ru octahedra and Curie-Weiss parameters calculated from magnetization measurements at 1000 Oe for the two samples of LaSrCoRuO₆ and LaCaCoRuO₆. Numbers in parentheses are uncertainty in the last digit.

Sample	LaSrCoRuO ₆	LaCaCoRuO ₆
a (Å)	5.5847(4)	5.5068(4)
b (Å)	5.5592(6)	5.5878(4)
c (Å)	7.8674(9)	7.8138(6)
β	90.05(2)	90.06(1)
Volume (Å ³)	244.25(4)	240.46(4)
Co ($\frac{1}{2}, 0, \frac{1}{2}$)	0.98(1)	0.99(1)
Ru ($\frac{1}{2}, 0, \frac{1}{2}$)	0.02(1)	0.01(1)
Ru ($\frac{1}{2}, 0, 0$)	0.98(1)	0.99(1)
Co ($\frac{1}{2}, 0, 0$)	0.02(1)	0.01(1)
BVS (Co)	2.54(2)	2.38(2)
BVS (Ru)	4.96(3)	4.74(5)
Co-O1-Ru	159.4(3)	154.1(2)
Co-O2-Ru	164.3(3)	154.4(3)
Co-O3-Ru	161.6(2)	154.9(2)
μ_{eff} (μ_B/fu)	5.47(2)	5.27(2)
Θ_{CW} (K)	-49(2)	-150(4)

kind of spin ordering. No such anomaly is visible in case of LaCaCoRuO₆. It can also be noticed that the resistivity of the Sr containing double perovskite is lower than that with Ca at the A-site. This lower resistivity can be related to the structure. The lower Co-O-Ru bond angle which leads to population of the π^* band in LaSrCoRuO₆ provides quasi-itinerant charges which decrease the resistivity in case of this sample.

6.4 Magnetization Measurements

Magnetization measurements performed at 1000Oe during the ZFC and FC cycles for LaSrCoRuO₆ and LaCaCoRuO₆ samples are presented in Fig. 6.4. In the case of LaSrCoRuO₆, both the ZFC and FC cycles rise sharply below 160K and branch off below 130K. While the ZFC curve culminates into a broad hump centered at about 55K, the

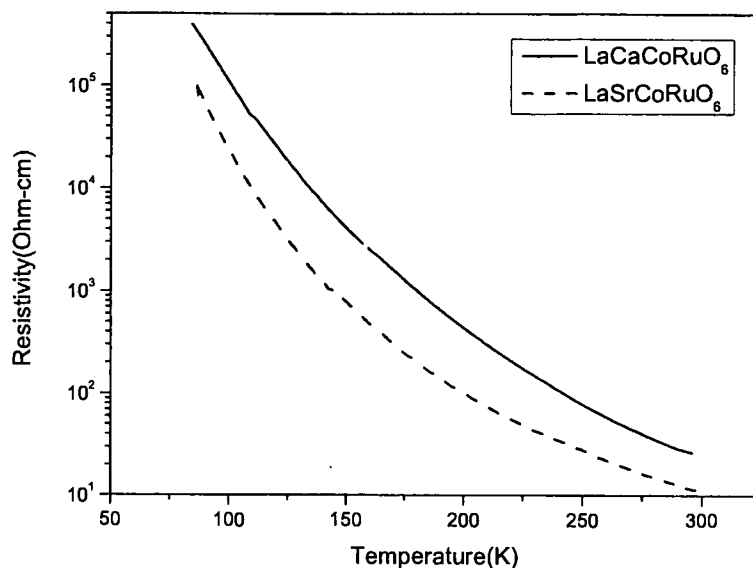


Figure 6.3: Temperature dependence of resistivity of LaSrCoRuO₆ and LaCaCoRuO₆

FC curve approaches a constant value below 77K. It has been reported earlier that this sample orders antiferromagnetically below $T_N = 87\text{K}$ [7].

In the case of LaCaCoRuO₆ as well, a similar type of antiferromagnetic ordering is reported below $T_N = 96\text{K}$. Our data also shows a deviation from paramagnetic behaviour around 80K. This difference in ordering temperature could be due to volatilization of Ru at high temperature during sample preparation. However, the sharp rise at about 150K seen in case of Sr containing sample is absent in LaCaCoRuO₆. This has been attributed to the non ferromagnetic nature of CaRuO₃. These double perovskites can have tiny undetectable amounts of SrRuO₃ and CaRuO₃ depending upon A-site cations. Since SrRuO₃ orders ferromagnetically, a sharp rise in magnetization of LaSrCoRuO₆ is visible. However, from previous chapters and even in Fig. 6.1 above it can be seen that no hysteresis is seen in isothermal magnetization ruling out presence of even tiny amounts of SrRuO₃ impurity. Therefore the difference in magnetization behaviour has

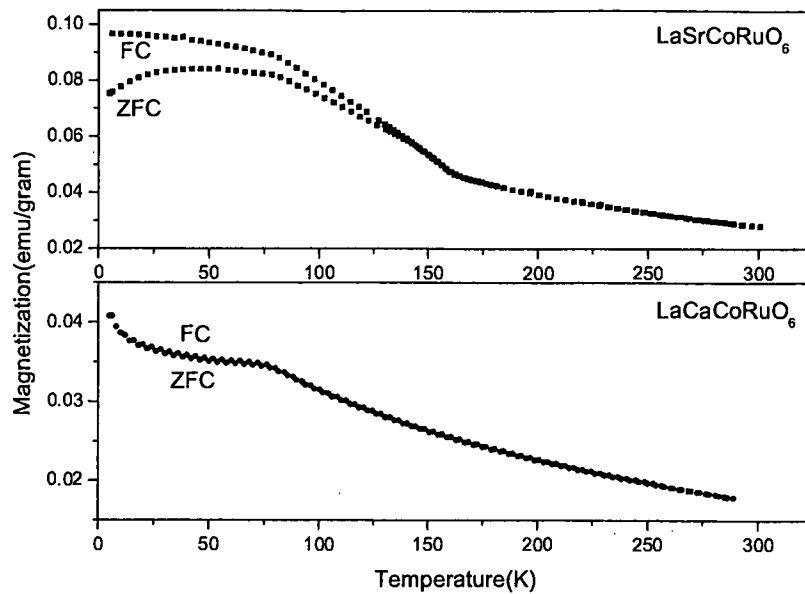


Figure 6.4: Magnetization as a function of temperature at applied fields of 1000 Oe for LaSrCoRuO_6 and LaCaCoRuO_6 .

to be intrinsic and could be related to presence of larger Sr as compared to Ca.

In order to discount the possibility of presence of Ru^{4+} in the compounds inverse of susceptibility ($1/\chi = H/M$) as a function of temperature is plotted in the Fig. 6.5. It can be seen that while the susceptibility of LaSrCoRuO_6 deviates from Curie-Weiss behaviour below 150K, that of LaCaCoRuO_6 is linear down to 80K. Fitting of Curie-Weiss equation to the data yields effective paramagnetic moment $\mu_{eff} = 5.47 \mu_B/\text{f.u.}$ and $5.24 \mu_B/\text{f.u.}$ for Sr and Ca containing samples respectively. These values are in fairly good agreement with the calculated spin only moment of Co^{2+} and Ru^{5+} ions. The Curie-Weiss temperature values for both these compounds are also reported in Table 6.1. Θ_{CW} are large and negative and in agreement with the values reported in literature [6, 8]. The negative values of Θ_{CW} indicate the presence of strong antiferromagnetic interactions in both the compounds.

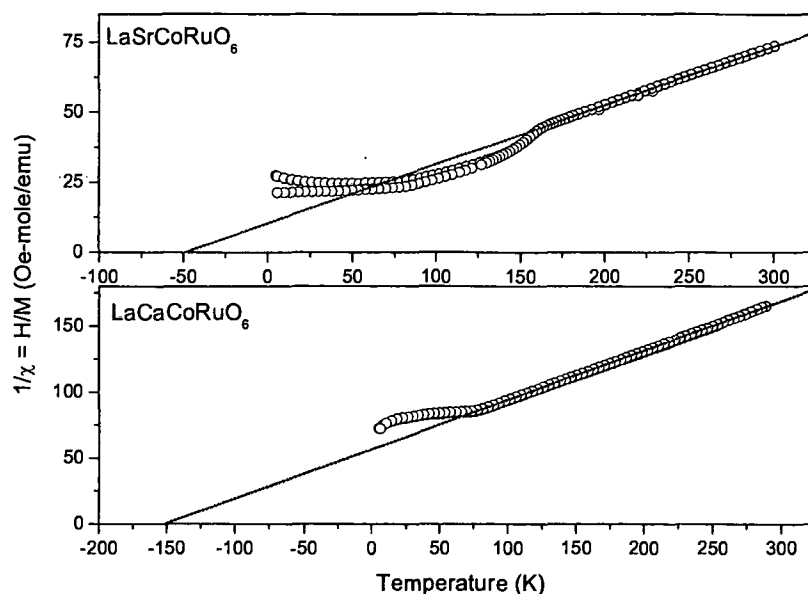


Figure 6.5: Plot of Inverse Magnetic susceptibility ($1/\chi = H/M$) as a function temperature for LaSrCoRuO_6 and LaCaCoRuO_6 . The solid line is a fit to Curie-Weiss equation.

Magnetization measurements in a low field of 50 Oe were measured during ZFC and FC cycles on both the samples, LaSrCoRuO_6 and LaCaCoRuO_6 and are presented in Fig. 6.6. In the case of LaCaCoRuO_6 , both FC and ZFC curves trace each other in the entire temperature region and exactly replicate the behaviour seen at 1000 Oe. Whereas for LaSrCoRuO_6 , the magnetization exhibits a large deviation between the ZFC and FC cycles below 160K and is very different from that seen at 1000 Oe. During the FC cycle the magnetization decreases with increase in temperature, exhibiting a sharp transition at about 160K resembling a transition from a magnetically ordered to a paramagnetic state. ZFC magnetization is low and shows a small increase with increasing temperature upto about 160K. Since ferromagnetic SrRuO_3 impurity has been ruled out, the behaviour in LaSrCoRuO_6 could be related to weak ferromagnetic interactions arising from anti-symmetric exchange interactions like the Dzyloshinskii-Moriya (DM) interaction [9, 10]

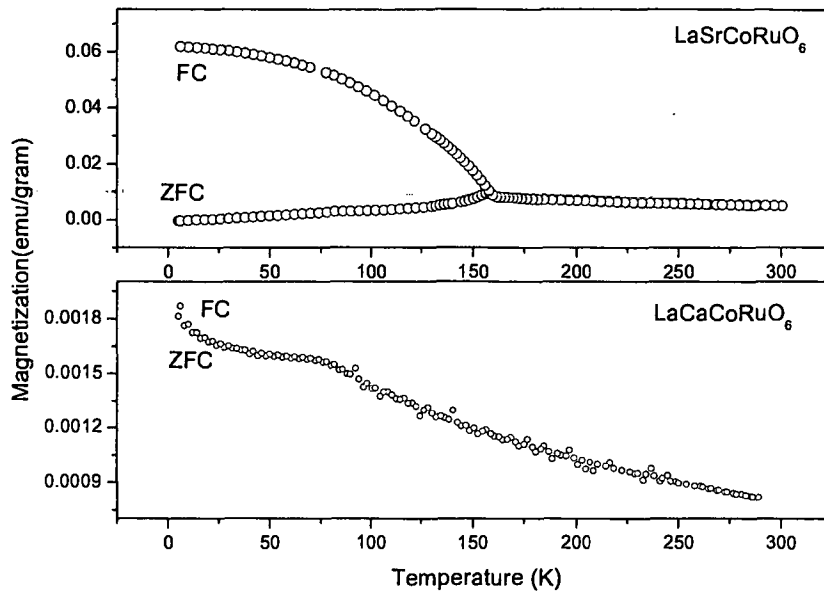


Figure 6.6: Magnetization as a function of temperature at applied fields of 50 Oe in LaSrCoRuO_6 .

due to the monoclinic crystal structure of LaSrCoRuO_6 . Double perovskites with Ru^{5+} ions like Sr_2YRuO_6 are known to have competing ferromagnetic and antiferromagnetic interactions [11]. The low symmetry structures of these double perovskites are susceptible to structural distortions and these can give rise to some antisymmetric exchange interactions. Since the symmetric exchange coupling between the Co and Ru sublattices is frustrated, the weaker antisymmetric (DM) interactions determine the perpendicular arrangement of the Co and Ru sublattice moments. These interactions strengthen the Co-O-O-Co or Ru-O-O-Ru antiferromagnetic exchange paths leading to a slight canting of the Co and Ru moments. Since the Co-O-Ru bond angles in LaCaCoRuO_6 are smaller, the antiferromagnetic alignment is strengthened which is reflected in slightly higher T_N and much larger negative values of Θ_{CW} .

6.5 Discussion

In SrRuO_3 , the $4d$ electrons of the Ru^{4+} ions occupy a narrow π^* band that is two-thirds filled but the spontaneous magnetization extrapolated to 0K is $M_s(0) = 1.4\mu_B/\text{Ru}$ [13], which is reduced from the spin-only value of $2.0\mu_B/\text{Ru}$. Broadening the π^* band by substituting the more basic Ba^{2+} ion for Sr^{2+} ion in the cubic perovskite, lowers both T_C and $M_s(0)$ as anticipated for itinerant-electron ferromagnetism [14]. Substitution of the more acidic Ca^{2+} ion for Sr^{2+} narrows the π^* band, but this band narrowing does not lead to an increase in the $M_s(0)$ [15]. Instead leads to a progressive transition to a nonmagnetic state ($J = 0$) as a result of spin-orbit coupling.

The narrow π^* band at the threshold of a transition from itinerant to localized electronic behaviour in the $\text{A}^{2+}\text{RuO}_3$ perovskites is due to $\text{Ru}^{4+}-\text{O}^{2-}-\text{Ru}^{4+}$ interactions. Introduction of the trivalent La^{3+} at the A site in $\text{A}_{2-x}\text{La}_x\text{Ru}_{2-x}\text{Co}_x\text{O}_6$ narrows the π^* band further and converts some of the Ru ions to pentavalent state. At $x = 1$, an archtype double perovskite of the type LaACoRuO_6 results with Co^{2+} and Ru^{5+} states. This charge transfer is facilitated because the partially filled 3d levels of Co^{3+} are well below the conduction band of Ru^{4+} . Therefore it is energetically favorable to transfer electrons from the Ru^{4+} conduction band (π^* band) to the electronic states of Co, even though such electrons will be more localized. This explains the transition from metallic ARuO_3 to semiconducting double perovskites. Further the presence of Co^{2+} in high spin state and Ru^{5+} ions ensure stable spins down to lowest temperature.

In both the double perovskites, LaSrCoRuO_6 and LaCaCoRuO_6 , the presence of substantial magnetic moments at both Co and Ru leads to dominant Co-O-Ru-O-Co linear σ superexchange interaction via the vacant e_g orbitals on Ru leading to an antiferro-

magnetic Co and Ru sublattices. In addition the existence of competing 90° Co-O-O-Co and Ru-O-O-Ru antiferromagnetic exchange paths results in magnetic frustration. Low values of long range magnetic moments detected by neutron diffraction are a result of this frustration [16]. Presence of Sr has a effect on the width of the π^* band of Ru in the double perovskite. As can be seen from the Rietveld refinement of XRD patterns, Co-O-Ru bond angle is higher in Sr containing double perovskite than that in LaCaCoRuO_6 . A straighter bond angle will aid in formation of a quasiitinerant π^* bands. This results in lower resistivity. Further such formation will result in weak ferromagnetic interactions due to antisymmetric exchange coupling which are a cause of large difference between ZFC and FC magnetization curves in LaSrCoRuO_6 .

6.6 Conclusion

In summary, both the double perovskites, LaSrCoRuO_6 and LaCaCoRuO_6 form archtype double perovskites crystallizing in an monoclinic structure. This structure allows for ordering of the B-site cations in a NaCl fashion. This type of ordering is favoured due to the charge difference of $\delta \geq 3$ between Co and Ru. Although both are perfectly ordered systems with Co^{2+} and Ru^{5+} magnetic ions coupling antiferromagnetically, LaSrCoRuO_6 sample exhibits ferromagnetic like rise in magnetization below 160K. This can be attributed to competition between linear Co-O-Ru-O-Co and the perpendicular Ru-O-O-Ru or Co-O-O-Co type antiferromagnetic correlations. This competition is enabled due to straightening of Co-O-Ru bonds in Sr containing sample. These interactions compete with each other leading to a slight canting of antiferromagnetically aligned spins leading to the observed ferromagnetic signal.

References

- [1] A. Callaghan, C. W. Moeller, R. Ward, *Inorg. Chem* **5**, 1572 (1966).
- [2] T. C. Gibb, R. Greatrex, N. N. Greenwood and P. Kaspi, *J. Chem. Soc. Dalton Trans.*, **12**, 1253 (1973).
- [3] A. Maignan, B. Raveau, V. Hardy, N. Barrier, R. Retoux, *Phys. Rev. B*, **74**, 024410 (2006).
- [4] S. Kim, R. I. Dass, and J. B. Goodenough, *J. Solid State Chem.*, **181**, 2989 (2008).
- [5] J. W. G. Bos, J. P. Attfield, T. S. Chan, R. S. Liu, L. Y. Yang, *Phys. Rev. B*, **762**, 014101 (2005).
- [6] J. W. G. Bos and J. P. Attfield, *Phys. Rev. B*, **69**, 094434 (2004)
- [7] J. W. G. Bos and J. P. Attfield, *Chem. Mater.*, **16**, 1822 (2004)
- [8] A. Mamchik, W. Dmowski, T. Egami, I -W. Chen, *Phys. Rev. B*, **70**, 104410 (2004)
- [9] I. Dzyaloshinskii, *J. Phys. Chem. Solids*, **4**, 241 (1957).
- [10] T. Moriya *Phys. Rev.*, **120**, 91 (1960).
- [11] G. Cao, Y. Xin, C. S. Alexander and J. E. Crow, *Phys. Rev. B.*, **63** 184432 (2001)
- [12] R. P. Singh and C. V. Tomy, *Phys. Rev. B*, **78**, 024432 (2008)

- [13] G. Cao, S. McCall, M. Sheppard, J. E. Crow, R. P. Guertin, *Phys. Rev. B*, **56**, 321 (1997).
- [14] C. -Q Jin, J. -S. Zhou, J. B. Goodenough, Q. -Q. Liu, J. G. Zhao, I. X. Yang, Y. Yu, R. C. Yu, T. Katsura, A. Shatskiy, E. Ito, *Proc. Natl. Acad. Sci.*, **105**, 7115 (2008).
- [15] R. B. Griffiths, *Phys. Rev. Lett.*, **23**, 17 (1969).
- [16] M. Dlouha, J. Hejmanek, Z. Jirak, K. Knizek, P. Tomes and S. Vratislav, *J. Magn. Mater.*, doi:10.1016/j.jmmm.2009.06.035.

Chapter 7

Summary and Conclusions

Double perovskites have attracted attention due to unusual magnetic properties and half metallic nature of the charge carrier transport. The itinerancy and ferrimagnetism in these systems are found to arise from a double exchange type of mechanism in which the ordering and electronic configuration play a critical role, the characteristics of this type of ordering stem from the fact that it combines features of both ferromagnetic and antiferromagnetic systems. LaSrCoRuO_6 is an archtype double perovskite which offers a unique opportunity to examine the interplay of the cationic order, charge balance, transport and magnetic interactions between Co and Ru species. The main aim of the present work is the study the effect of thermal and substitutional disorder on the structural, magnetic and transport properties of LaSrCoRuO_6 .

LaSrCoRuO_6 is an ideal double perovskite with Co and Ru octahedra arranging themselves in NaCl fashion. The valence of Co and Ru are +2 and +5 respectively. The degree of ordering of B-site cations in double perovskites is known to play an important role in deciding the magnetic, transport and structural properties of these systems. Any disturbance of this order will result in the formation of additional magnetic species like Ru^{4+} and Co^{3+} which add to the magnetic interactions already present and interesting

magnetic ground states. The main highlight of this work is the observation of “magnetic compensation” and “negative magnetization” due to creation of thermal or substitutional disorder in LaSrCoRuO_6 . This reversal of magnetization has been explained on the basis of magnetic interactions that result due to the disorder in the occupancy of B-site of LaSrCoRuO_6 double perovskite.

7.1 Implications of this work

The archetype double perovskite LaSrCoRuO_6 is a $\text{AA}'\text{BB}'\text{O}_6$ type double perovskite crystallizing in a monoclinic structure. This structure allows for ordering of B-site cations in a NaCl fashion with the ordering being favored due to a charge difference ($\delta q \geq 3$) between Co and Ru. In the perfectly ordered LaSrCoRuO_6 (LSCR13), the Co^{2+} and Ru^{5+} magnetic ions are found to couple antiferromagnetically leading to an antiferromagnetic ground state that can be seen from neutron diffraction measurements. In order to induce disorder in the occupancy of B-site different annealing procedure was employed. This disorder in Co and Ru site occupancy results in Ru-O-Ru type linkages which are known to align ferromagnetically. The presence of ferromagnetic interactions are clearly seen in the disordered compound of LaSrCoRuO_6 (LSCR12) which has a larger B-site occupancy disorder in terms of an increased value of magnetization as compared to that in the ordered compound LSCR13 and hysteresis in M vs H loop. Due to such a disorder in occupancy of Co and Ru sites, octahedral distortions set in, as the immediate neighbor of a Ru octahedra could either be a Ru octahedra or a Co octahedra. The EXAFS results in the disordered compound LSCR12 bear a clear testimony to this fact, with the Co-O and Ru-O bond lengths being shorter, the mean square displacement being higher

and the Co-O-Ru bond being straighter. These changes are a result of of Ru-O-Ru ferromagnetic linkages which due to their presence alter the Ru-O-Co antiferromagnetic interactions. The negative magnetization seen in the low field ZFC magnetization is due to Ru-O-Ru ferromagnetic interactions which below $\approx 150\text{K}$ are found to polarize the Co spins in a direction opposite to the applied field giving rise to magnetic compensation and negative magnetization.

The substitution at the B-site in the archetype ordered LaSrCoRuO_6 double perovskite allows an opportunity to probe the changes in the structural, magnetic and transport properties due to the creation of $\text{Co}^{2+/3+}$ and $\text{Ru}^{5+/4+}$ redox couples in an environment with a fixed A-site variance and linearly varying the Goldschmidt tolerance factor. Here two types of substitution at B-site has been probed. In the first case Co and Ru antisite disorder has been created by selectively increasing the composition of one of them with respect to other resulting in $\text{LaSrCo}_{1-x}\text{Ru}_{1+x}\text{O}_6$. In the second case Cu^{2+} has been substituted for Co^{2+} . It is expected that partial substitution of Co by Cu will inhibit some of the magnetic interactions giving a better understanding of magnetic interactions at play in LaSrCoRuO_6 . In the entire doping range, for both the series namely, $\text{LaSrCo}_{1-x}\text{Ru}_{1+x}\text{O}_6$ and $\text{LaSrCo}_{1-y}\text{Cu}_y\text{RuO}_6$, the double perovskite structure is preserved. As is known from chapter 3, in the case of the undoped LaSrCoRuO_6 , there are two competing magnetic interactions, the linear Co-O-Ru-O-Co and the 90° Co-O-O-Co. The magnetic and transport properties of the doped $\text{LaSrCo}_{1-x}\text{Ru}_{1+x}\text{O}_6$ show significant changes due to the creation of Ru^{4+} and Co^{3+} species in both the Co and Ru doped compounds. The linear Co-O-Ru-O-Co and the 90° Co-O-O-Co interactions are diluted in the Ru and Co doped compounds at the expense of new interactions of the

type $\text{Ru}^{4+/5+}\text{-O-Ru}^{5+/4+}$ and those involving the HS/IS Co^{3+} . The sharp rise in magnetization seen at about 160K in all the Co and Ru doped compounds can be attributed to ferromagnetic interactions arising due to Ru-O-Ru nearest neighbour interactions leading to the filling up of the π^* bands and lowering of the resistivity as compared to the undoped LaSrCoRuO_6 . The temperature induced magnetization reversal displayed by the Ru rich compounds in low applied fields has been explained to be due to the polarization of the paramagnetic Co spins by Ru-O-Ru ferromagnetic interactions below the Ru sub-lattice ordering temperature of 160K. The Co spins are polarized in a direction opposite to the applied magnetic field giving rise to magnetic compensation and negative magnetization. However, in the case of the Co rich compounds, no negative magnetization is seen although there exists a steep rise in magnetization below 160K, instead only a large variation between the ZFC and FC magnetization curves is seen, which is also indicated by a decrease in the strength of ferromagnetic interactions with increasing Co content. Doping of Co and Ru results in the formation of Co-O-Co and Ru-O-Ru networks respectively. It is known that the Co-Co pairs favour the trivalent state and likewise, the Ru-Ru pairs favour the tetravalent states. Hence, the observed magnetic behavior reflects the general competition between the itinerant ferromagnetism and the antiferromagnetic superexchange coupling between Co-Co pairs, that are further modified by the interactions between Ru and Co.

The strong competition between magnetic interactions that lead to a decrease in the ordered moment of Co and Ru is reduced or eliminated with the substitution of Cu for Co in LaSrCoRuO_6 . The magnetic properties clearly indicate the presence of antiferromagnetic interactions from the negative Θ_{CW} and the magnetization behavior in

the entire temperature range. With Cu^{2+} substituting Co^{2+} , the charge on Ru remains unaltered, and the ionic sizes of the two ions being similar, no major structural changes are observed, resulting in nearly similar magnitude of resistivity as in the case of the undoped LaSrCoRuO_6 . The Cu substitution does not favour the formation of Ru-O-Ru or Co-O-Co networks, it instead disturbs the existing magnetic interactions especially the 90° Co-O-O-Co interaction with the result that antiferromagnetism appears to be strengthened.

Another possible way of modifying magnetic and transport properties is by forming the solid solutions of antiferromagnetic LaCoO_3 and ferromagnetic SrRuO_3 . These perovskite solid solutions of the form $\text{Sr}_{1-x}\text{La}_x\text{Ru}_{1-x}\text{Co}_x\text{O}_3$ will have a strong interplay of cationic order, charge balance and complex magnetic interactions between the two B-site cations. The charge transfer between Ru and Co in LaSrCoRuO_6 is very sensitive to local atomic structure such as cation order. Any disturbance in this cation order leads to compensation of antiferromagnetic interactions by the ferromagnetic interactions most likely associated with Ru-O-Ru interactions. Investigations on the structural, magnetic and transport properties of solid solutions of SrRuO_3 and LaCoO_3 which form double perovskite compounds of the type $\text{La}_{2x}\text{Sr}_{2-2x}\text{Co}_{2x}\text{Ru}_{2-2x}\text{O}_6$, where $0.25 \leq x \leq 0.75$ have been carried out. With the increase in Co content, ferromagnetic interactions are found to weaken and at $x = 0.75$ the compound orders antiferromagnetically at $T_N = 34\text{K}$. This interplay of ferromagnetic and antiferromagnetic interactions is attributed to presence of $\text{Ru}^{4+}/\text{Ru}^{5+}$ and $\text{Co}^{2+}/\text{Co}^{3+}$ redox couple in all the compounds. The only exception to this is the ordered compound $x = 0.5$ wherein Co and Ru exist in divalent and pentavalent states respectively representing an archtype double perovskite. The presence of different

magnetic sublattices leads to magnetic compensation and negative magnetization. This can be explained by polarization of paramagnetic Co spins by the ferromagnetic Ru⁴⁺ sublattice in a direction opposite to applied field.

In our studies on double perovskite with A = Sr, it is found that even a small disorder in Co and Ru occupancies gives rise to a competition between ferromagnetic and antiferromagnetic interactions. The ferromagnetic interactions are a result of Ru-O-Ru coupling that arise due to disorder in Co-O-Ru-O-Co arrays. It may be noted that although SrRuO₃ is a ferromagnetic metal, its counterpart CaRuO₃ does not show any long range magnetic order. Therefore in order to understand the role of Sr in magnetic and transport properties of double perovskite, LaSrCoRuO₆ a comparative study between its magnetic and transport properties and those of LaCaCoRuO₆ was made. Both the samples have the similar structural and magnetic ground states. Presence of Sr has a effect on the width of the π^* band of Ru in the double perovskite. In the Sr containing sample, the Co-O-Ru bond angle is higher than that in LaCaCoRuO₆. A straighter bond angle will aid in formation of a quasiitinerant π^* bands. Such a formation will result in weak ferromagnetic interactions. The double perovskites consists of two coupled type II antiferromagnetic sub lattices. The coupling that results due to Dzyaloshinskii-Moriya (D-M) interaction works to reduce the effective antiferromagnetic moment. Presence of weak ferromagnetic interactions in LaSrCoRuO₆ drives the system to a point of magnetic frustration. Any change therefore in the coupling between Co and Ru in this compound gives rise to magnetic compensation and negative magnetization.

7.2 Future Work

In this concluding segment, we mention a few fields that can be pursued in relation to double perovskites in the coming years. Double perovskite oxides are becoming more and more important in various technological applications and hence the need to improve our detailed understanding of the structural, magnetic and transport properties of such materials and how the atomic structure is related to macroscopic physical properties. The commercial potential of these materials is determined and the effort has opened up new classes for application in spintronic devices such as magnetic tunnel junctions or low field magnetoresistive sensors. The structural, magnetic and electronic properties of perovskite-related materials having the general formula $AA'BB'O_6$ (where A and A' are lanthanides or alkaline-earths, B is transition metal ion and containing Ru^{5+} at the B' site) have been extensively investigated by a number of research groups. The compounds that belong to this family have a wide variety of interesting magnetic properties. In light of the results presented in this thesis, it is worth looking at magnetic properties of double perovskites formed with other transition metal compounds instead of Co^{2+} . For instance compounds with Mn, Fe which normally occur in +3 state may have interesting magnetic and transport properties. These could be compared with double perovskites containing Ni which would be in +2 state.

The subject of magnetization reversal in oxides and intermetallic compounds has received considerable attention. The magnetization reversal is usually achieved by applying a large magnetic field in a direction opposite to the aligned moments or by changing the temperature in moderate fields. The temperature induced magnetization reversal, which is quite rare, has been found to occur in systems having two or more different types of

magnetic ions, that are positioned at different crystallographic sites. A few ferrimagnetic compounds are known to show temperature induced magnetization reversal effect when two antiferromagnetically coupled magnetic sublattices exhibit different temperature dependence of the magnetization. There are few other oxides and intermetallic compounds which are known to show temperature induced magnetization reversal such as LnVO_3 ($\text{Ln} = \text{Y, La, Sm, Nd etc.}$), $(\text{Sm, Gd})\text{Al}_2$, LnCrO_3 ($\text{Ln} = \text{Gd, La}_{0.5}\text{Pr}_{0.5}$) etc, however the origin of magnetization reversal in these compounds is found to be entirely different compared to that of the ferrimagnetic compounds.

In the compound such as LaVO_3 , one of the reasons for the observed magnetization reversal is the competing effects of the D-M interaction and the single ion anisotropy of the V moments, as in the case of YVO_3 in the temperature range of 75K-110K. The magnetic ordering of the Yb moments in $\text{Sr}_2\text{YbRuO}_6$ is considered to be purely antiferromagnetic without any canted moments. The observation for negative magnetization in $\text{Sr}_2\text{YbRuO}_6$ when compared with that of LaVO_3 compound, it is to be noted that in the case of LaVO_3 , the D-M vector rotates against the magnetic field at the structural transition resulting from the first order magnetostrictive distortion, however since the structure of $\text{Sr}_2\text{YbRuO}_6$ remains the same at 10K as deduced from neutron diffraction measurements, the possibility of any structural transition and hence the rotation of the D-M vector against the field is found to be ruled out. Future investigations on whether such a rotation can be initiated by the magnetic ordering of the Yb moments need to be looked into.

Publications

- Journals:

1. Murthy P. S. R., Priolkar K. R., Bhobe P. A., Das A., Sarode P. R. and Nigam A. K. (2010): Structure, Transport and Magnetic properties in $\text{La}_{2x}\text{Sr}_{2-2x}\text{Co}_{2x}\text{Ru}_{2-2x}\text{O}_6$, J. Magn. Magn. Mater. (communicated)
2. Murthy P. S. R., Priolkar K. R., Bhobe P. A., Das A., Sarode P. R. and Nigam A. K. (2010): Effect of B-site Dopants on Magnetic and Transport Properties of LaSrCoRuO_6 , European Physical Journal B (accepted).
3. Murthy P. S. R., Priolkar K. R., Bhobe P. A., Das A., Sarode P. R. and Nigam A. K. (2010): Disorder Induced Negative Magnetization in LaSrCoRuO_6 , J. Magn. Magn. Mater. **322** 3704-3709.

- Conference Proceedings:

1. Murthy P. S. R., Priolkar K. R., Sarode P. R., Bhobe P. A. and Nigam A. K. (2009) Effect of dopants on Magnetic and Transport properties of LaSrCoRuO_6 , Proceedings of DAE Solid State Physics Symposium, BARC, Vol. 54C 1001-1002.
2. Murthy P. S. R., Bhobe P. A., Priolkar K. R., Sarode P. R. and Nigam A. K. (2008) Structure, Transport and Magnetic properties in $\text{La}_x\text{Sr}_{1-x}\text{Co}_x\text{Ru}_{1-x}\text{O}_3$, Proceedings of DAE Solid State Physics Symposium, BARC, Vol. 53C 1107-1108.

3. Murthy P. S. R., Bhoje P. A., Priolkar K. R., Sarode P. R. and Nigam A. K. (2007): Anomalous Ferrimagnetism in Double Perovskite $\text{LaSrCo}_{1-x}\text{Ru}_{1+x}\text{O}_6$ Proceedings of Solid State Physics Symposium at Mysore India Vol. 52C 1055-1056.

- Conference Presentations:

1. Murthy P. S. R., Priolkar K. R., Das A. and Sarode P. R. (2009) Neutron Diffraction Studies on $\text{La}_{1-x}\text{Sr}_x\text{Co}_{1-x}\text{Ru}_x\text{O}_3$, Presentation at Conference on Neutron Scattering and Mesoscopic Systems, Goa, India. (Peer review - abstract only).
2. Murthy P. S. R., Priolkar K. R., Das A. and Sarode P. R. (2008): Neutron Diffraction Studies on Cobalt and Ruthenium based Double Perovskites, Presentation at International Conference on Neutron Scattering, BARC Mumbai (Peer review - abstract only).